Theory for superconductivity and magnetism in layered titanium and chromium based materials

2023, March

Han-Xiang Xu

Research Institute for Interdisciplinary Science
Graduate School of Natural Science and Technology
(Doctor's Course)

OKAYAMA UNIVERSITY

Abstract

Condensed matter physics is one of the most active research fields in physics today. It was named in 1960s with solid state physics as predecessor. Investigations of condensed matter physics focus on the physical properties of matter in condensed phases including well-known solid and liquid phases, and novel superconducting phase, Bose–Einstein condensate phase, spin derived magnetic phases, *etc.*

Superconductors and superconductivity are one of the most remarkable discoveries of research in condensed matter physics in the 20th century. This exotic phenomenon is that with temperature decreasing the resistivity will disappear at a certain critical temperature, which was first detected in a low temperature experiment in mercury. In the course of time, an ever-growing number of superconductors, not only classical metals but also alloys, metallic oxides, non-metallic compounds, organics, and so forth, are found or synthesized. Moreover, with the researchers' efforts, the critical temperature, the transition temperature of the superconducting phase, was increased again and again. Until now, a few of superconductors with very high critical temperature near room temperature are reported in some extraordinary conditions like extremely high pressure. In the meantime, theoretical studies to explain the origin and nature of superconductivity are also continuously developing. One of the great successes is Bardeen–Cooper–Schrieffer (BCS) theory that interprets superconductivity in the superconductors discovered first that are named conventional superconductors now. Nevertheless, not all superconductors can be explained by BCS theory and those that cannot are called unconventional superconductors. Especially recent thirty years superconductivity is found in some compounds, in which metallic elements combine with the elements of poor metals or even non-metals, such as some cuprates with CuO_2 planes that are insulators at room temperature. For these kind of unconventional superconductors with strong correlation, spin fluctuation theory is successful in explaining an essential part, the origin of superconductivity in these systems. Until now, spin fluctuation theory is still developed in several kinds of performances, for example random phase approximation, fluctuation exchange, *etc.*

Thus, due to a mass of superconductors discovered today, it is necessary to develop spin fluctuation theory and to answer a question that are their superconducting mechanism interpreted by spin fluctuation theory, for the great, interesting question of universal rules or theory of superconductors and superconductivity.

Magnetism is another important topic of condensed matter physics, and it is connected to superconductivity due to spin fluctuations near magnetic instabilities. Magnetism was already found in ancient time and was thoroughly investigated in classical physics. After science lectured the gate of microscopic world, the understanding of magnetism began. It is clear that on microworld we can easily find that different performances of magnetism derived from different spin configuration. In this work, we study a phase transition with magnetic characteristics, and we want to find the connection between magnetism and superconductivity.

In our studies, we research superconductivity and magnetism in compounds of transition metals. Physical properties of transition metals are decided by d electrons. Especially for period 4, there are a lot of important elements, for example titanium (Ti), chromium (Cr), iron (Fe), nickel (Ni), copper (Cu) and so on. Thus, studying $3d$ electron systems is useful for understanding, preparing, and even designing materials with superconductivity or magnetism. In this work we only concentrate on two kinds of materials, titanium oxypnictides and chromium tellurides.

In our first study, titanium oxypnictides are investigated. Depending on density functional theory (DFT) we investigate the titanium oxypnictides $BaTi_2Pn_2O$ (Pn = pnictogen). Their crystal structure shows the feature of a square lattice that is similar to cuprates and iron-based superconductors. Thus, we are seeking for some common ground for superconductivity. One interesting area is $Ba_{1-x}A_xTi_2Sb_2O$ with varying alkali-doping. For reproducing the doping variation of the crystal structures, we use interpolated lattice parameters from experiment and the virtual crystal approximation for varying the doping level. Using density functional theory we determine density of states and band structure with the orbital character, but it is not enough to explain the variation of critical temperature with doping. Thus, by using projective Wannier functions we extract a tight-binding model for $Ba_{1-x}A_xTi_2Sb_2O$ and apply the random phase approximation for the Hubbard model to calculate susceptibilities and pairing vertex for revealing the superconducting order parameters of the gap function. Even with heavy doping, there is no high critical temperature in titanium oxypnictides comparing with cuprates or iron-based superconductors, we think it is due to the differences of bond of Ti.

In second study, we investigate a type of chromium tellurides, where superconductivity was reported in $CrSiTe_3$ recently. However due to the lack of information of crystal structure at high pressure, it is difficult to get a whole picture of $CrSiTe_3$

and reveal superconductivity. We also study $CrGeTe_3$ where there is an interesting insulator-metal transition and evolution of magnetic properties with pressure. Similarly, from the beginning, we use DFT to investigate $CrGeTe_3$ with varying pressures. By applying DFT+U, exchange couplings of Cr are determined, which yields Curie-Weiss temperatures in agreement with experiment. Meanwhile from DFT+U, average charge gap exhibits the insulator-metal transition happened around 5GPa. Beyond DFT, dynamical mean-field theory (DMFT) is a better choice for strongly correlated systems, and by using DMFT we can get additional information. Within DMFT, insulator-metal transition is confirmed. We obtain spectral functions which are can be compared with angle-resolved photoemission spectroscopy results. Finally, the magnetic ground state of $CrGeTe_3$ is discussed. We expected that after introducing strong correlation by DMFT it is hopeful to give a more precise explanation for the phase diagrams of $CrGeTe_3$ and even $CrSiTe_3$.

Contents

Chapter 1

Introduction

Superconductors and superconductivity is one of the most important discoveries in the 20th century. With two remarkable properties, zero resistivity and Meissner effect, superconductors play a significant role in many fields, for example energy storage [1], high magnetic field creator [2], power cable/wires [3], *etc.* Moreover an increasing number of novel superconductors are found or synthesized. However not all of the newer superconductors can be explained by the standard theory of superconductivity built in the last century. In this thesis the aim of our study is to give a theoretical explanation for some new superconductors that are found recently.

1.1 Superconductor and superconductivity

Superconductivity was first discovered in mercury at 4.2 K as reported by H. Kamerlingh Onnes in 1911 [4]. When temperature is lower that 4.2 K which is achieved by liquefying helium the resistance of mercury decreases to zero, in other words, resistance vanishes. This behavior was named superconductivity, and materials that show it were called superconductors. After the discovery of mercury, by the improvement of low temperature technology, superconductivity was discovered in more and more elements and complex materials.

Then in 1957 the first complete theory that can explain the superconducting microscopic mechanism was developed by Bardeen, Cooper and Schrieffer [5]. This is the famous Bardeen-Cooper-Schrieffer (BCS) theory. In this theory they gave a very important concept that there is an attractive interaction between electrons resulting from virtual exchange of phonons. This electron-electron pair is the so-called Cooper pair. Until now, the Cooper pair is the most critical feature of any superconductor. Thus, BCS theory is one of the most successful theories of superconductivity, in

which the specific heat and critical temperature T_c of superconductors are explained and predicted directly.

Over the years, an increasing number of superconductors are reported. However, researchers noticed that there are some superconductors that do not follow the mechanism proposed by BCS theory. These novel superconductors are called unconventional superconductors. Meanwhile, the BCS type superconductors are conventional superconductors.

Nowadays, there are two intriguing large families of unconventional superconductors attracting a lot of researchers. One is cuprate superconductors and another one is iron-based superconductors. Superconductivity of cuprates was first discovered in 1986 in a Ba-La-Cu-O system [6]. Recently, high T_c yttrium barium copper oxide (YBCO) is a very popular material in both science and engineering fields. In contrast to cuprates, iron-based superconductors were only discovered in 2006 [7]. In the phase diagram of many doped iron-based superconductors, the feature of superconducting domes occurring as function of various control parameters attracts a lot of attention.

In the past ten years, some newer superconductors belonging to $3d$ electron systems with physical properties that are similar to iron-based superconductor are discovered. It is important that their similarities of physical properties are mainly effected by these $3d$ electrons but differences are due to different number of electrons. Our study focuses on titanium-based superconductors and ternary chromium tellurides which both belong to $3d$ electron systems.

1.2 Titanium-based superconductors

1.2.1 Background

Titanium-based superconductors are new kinds of superconductors that were discovered and investigated in the past ten years. There are layered structures for several titanium-based superconductors and titanium itself is a member of $3d$ electron system materials, which would be the common grounds with cuprates or iron-based superconductors that is easy to stimulate researchers curiosity to study the physical properties of these materials including superconductivity.

The first layered titanium oxypnictides $Na_2Ti_2As_2O$ and $Na_2Ti_2As_2O$ were synthesized about thirty years ago [8], and their behavior in terms of spin-density wave (SDW) or charge-density wave (CDW) was investigated [9, 10].

Ten years ago, there is a new discovery of superconductivity of titanium oxypnictide materials that in a family of titanium oxypnictide $BaTi_2Pn_2O$ (Pn = pnictogen)

superconducting states exist at low temperature [14, 15] when a charge and/or spin

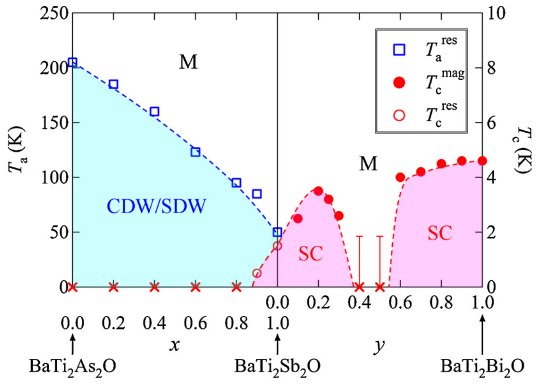

Figure 1.1: Electronicphase diagram of $BaTi_2(As_{1-x}Sb_x)_2O$ and $BaTi_2(Sb_{1-y}Bi_y)_2O$ from [11].

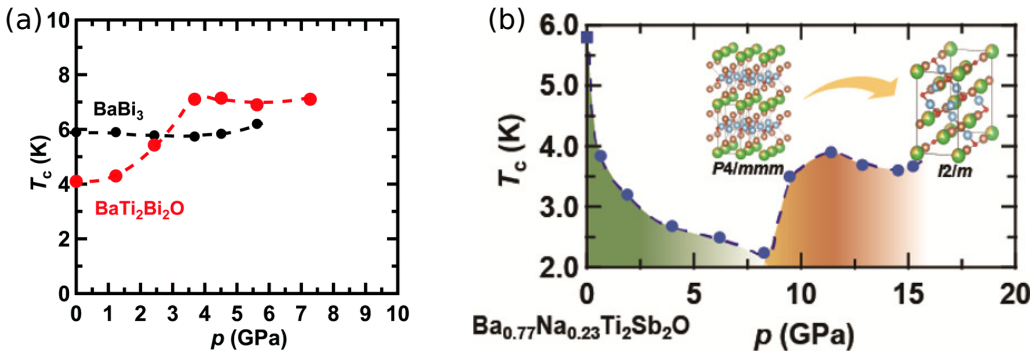

Figure 1.2: Superconducting T_c tuned by (a) only pressure [12], (b) pressure together with doping [13].

density wave is suppressed [11, 16]. An extensive discussion of the phase transition was observed in resistivity and magnetic susceptibility [9, 14, 17, 18] with thermoelectric power and Hall coefficient [19], in which there is one question whether it should be characterized as a CDW transition or a SDW transition. Experimental studies by NMR [20] and muon spin relaxation (μSR) [21, 22] were also discussed for this question.

Furthermore, it is found that the superconductivity of titanium oxypnictide $BaTi_2Pn_2O$ (Pn = pnictogen) is tunable by a lot of different parameters includ-

ing hole doping, isovalent doping and pressure [11, 18, 21, 23–25], of which details are given in the following.

First of all, with isovalent doping of As, Sb, and Bi, the doping-temperature phase diagram of $BaTi_2Pn_2O$ (Pn = As, Sb, Bi) shows an interesting two superconducting domes in Fig. 1.1.

Moreover, pressure is another suitable parameter to control superconductivity by itself or together with doping which is shown in Fig. 1.2, where in pattern (b) superconductivity changing with a structure collapse is a special case for controlling T_c.

However, we are most interested in the superconducting T_c of $Ba_{1-x}A_xTi_2Sb_2O$ tuned by alkali-doping (A=Na, K, Rb, and Cs) shown in Fig. 1.3, where we can

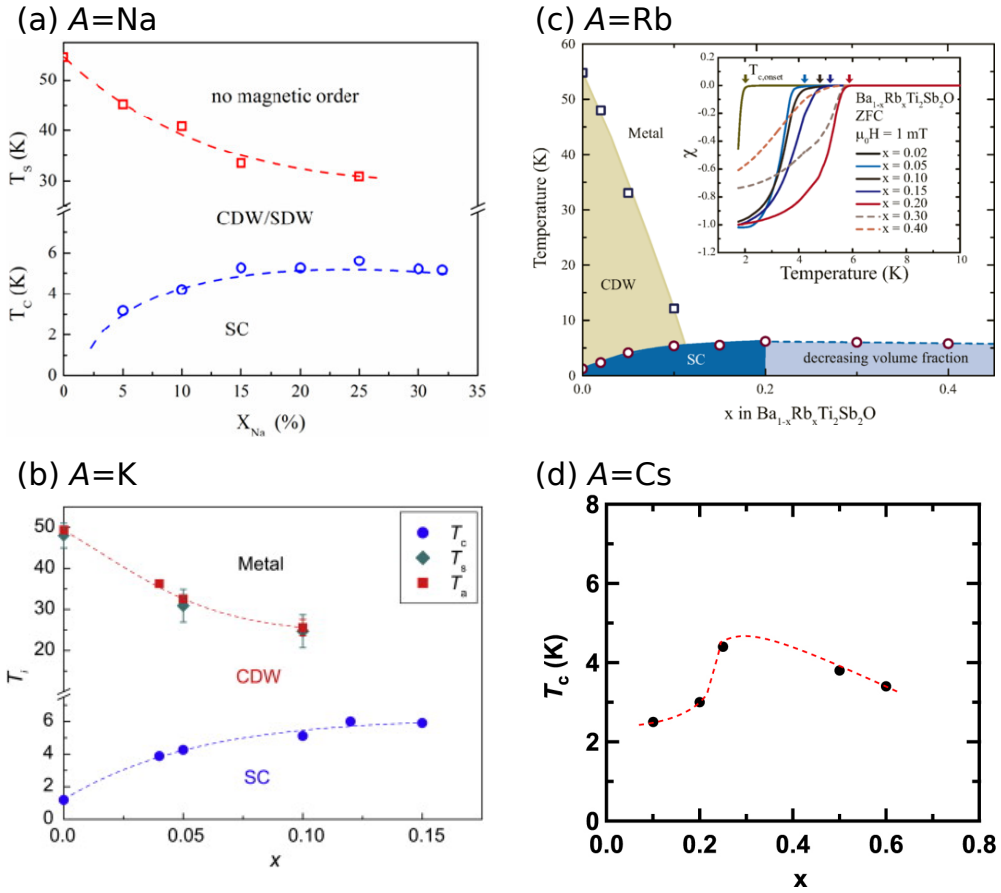

Figure 1.3: Phase diagram of alkali-doping vs. temperature of $Ba_{1-x}A_xTi_2Sb_2O$ for (a) A=Na [18], (b) A=K [23], (c) A=Rb [24], and (d) A=Cs [25].

easily find that T_c is enhanced by increasing alkali-doping and then is saturated in a certain doping level. This leads to half a superconducting dome in which higher doping structure cannot be made due to phase saturation.

Because of these intriguing physical properties of titanium oxypnictides $BaTi_2Pn_2O$, some researchers try to explain these behaviors theoretically. The rigid-band model is a theoretical tool that was usually used to study the hole doping of $BaTi_2Pn_2O$ [26, 27]. It is a fast and low-cost method for electron/hole doping. However, it is a rough approximation that does not always help people to understand these materials correctly. In our study, we plan to use a different approximation to approach the

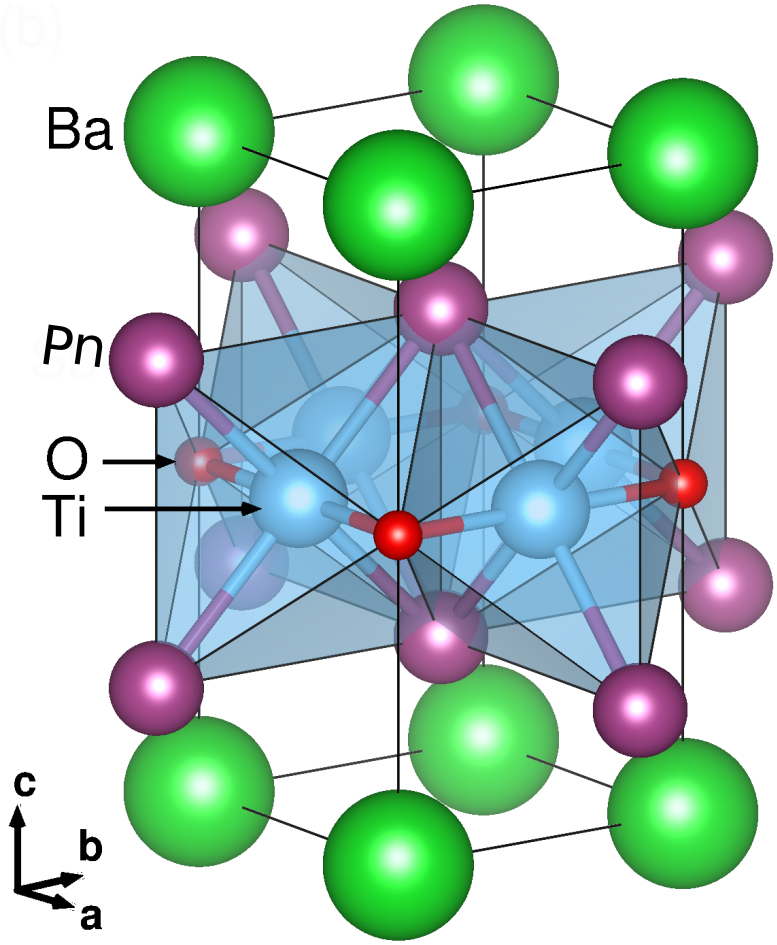

Figure 1.4: Crystal structure of $BaTi_2Pn_2O$ (Pn = pnictogen) with shaded TiO_2Pn_4 octahedra.

real alkali-doping of $BaTi_2Pn_2O$ and to explain their physical properties, especially superconductivity.

On the other hand, to decide if titanium oxypnictides are conventional or unconventional superconductor is another topic of these materials. There are different understandings from different studies, which sometimes are totally contradictory with each other. From the study of low-temperature heat capacity of $Ba_{1-x}Na_xTi_2Sb_2O$ [28], they think these materials are BCS-like conventional superconductors, but in the study where universal Uemura classification is used [29], $Ba_{1-x}Na_xTi_2Sb_2O$ are classified as unconventional superconductors. Therefore, to answer this question is also one of the aims of our studies.

Obviously, it is rewarding to study these materials for their expected unusual physical properties.

1.2.2 Structure

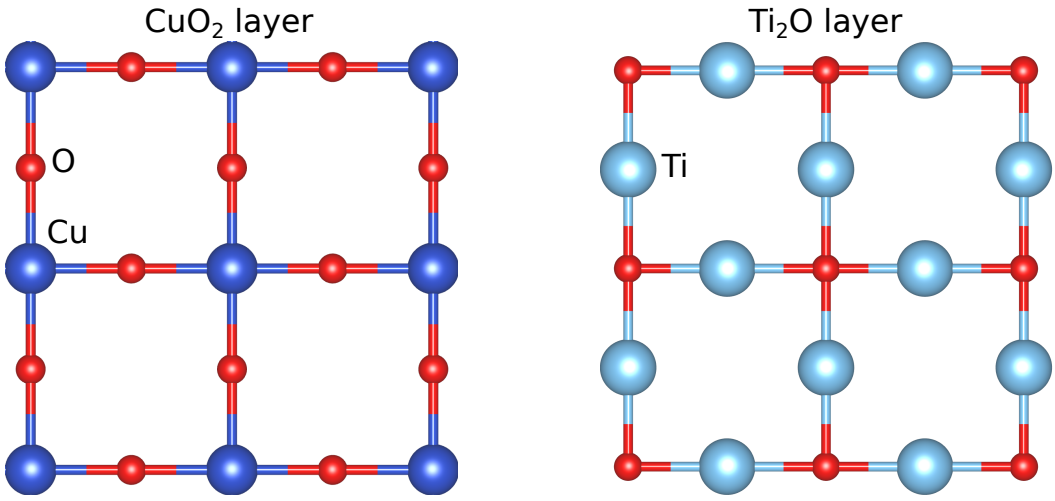

Figure 1.5: Comparison of CuO_2 layer of cuprates and Ti_2O layer of titanium-based superconductors.

The crystal structure of titanium oxypnictides $BaTi_2Pn_2O$ (Pn = pnictogen) is shown in Fig. 1.4, which is determined to be tetragonal with space group $P4/mmm$ (No. 123). Under doping or pressure, this structure is quite stable. Only heavy doping or high pressure or both of them simultaneously leads to a change of the space group.

Some researchers prefer to compare the Ti-O layer with Cu-O layer like shown in Fig.1.5. However, they are absolutely different structures, because around titanium atoms, there is an octahedral coordination made by pnictogen and oxygen atoms, which is crucially important and will be discussed in detail in the result chapter.

1.3 Ternary chromium tellurides

1.3.1 Background

There is a long time people believe that long range ferromagnetic order hardly survives in the two-dimensional (2D) systems. However, as time passed, there is a discovery that ferromagnetism could be remained in the van der Waals materials with bonded layers or even exfoliated monolayers [30]. The fact, which had been predicted theoretically [31], broke the understanding of no surviving ferromagnetism in the 2D materials, because of the enhanced thermal fluctuations revealed by the Mermin-Wagner theorem [32] that led to much more intense scrutiny of the materials $CrSiTe_3$ and $CrGeTe_3$, together with a few other layered ferromagnets like CrI_3 [33, 34] and Fe_3GeTe_2 [35].

Layered van der Waals ferromagnets that can be exfoliated are fueling a bonanza of fundamental exploration and nanoscale device demonstration. $CrSiTe_3$ and $CrGeTe_3$ are prime examples of this class of materials. Their magnetism is variable by applying pressure, and $CrSiTe_3$ even becomes superconducting [36]. These interesting behaviors attracted us to focus on these materials and we noticed that there are only a few studies that try to develop the understanding of these materials theoretically. Thus we are addressing solve this question by our investigation.

1.3.2 Structure

The crystal structure of chromium tellurides $CrSiTe_3$ or $CrGeTe_3$ is shown in Fig. 1.6, with space group $R\bar{3}$ (No. 148). It belongs to trigonal crystal system that have to be treated carefully for using different coordinate system.

Around chromium atoms there are 6 tellurium atoms, which built a special structure that some researchers think it is an octahedron. However, we do not consider this structure as an octahedron but figure out that it is a distorted triangular prism, which will lead to a different split of orbitals by crystal field theory.

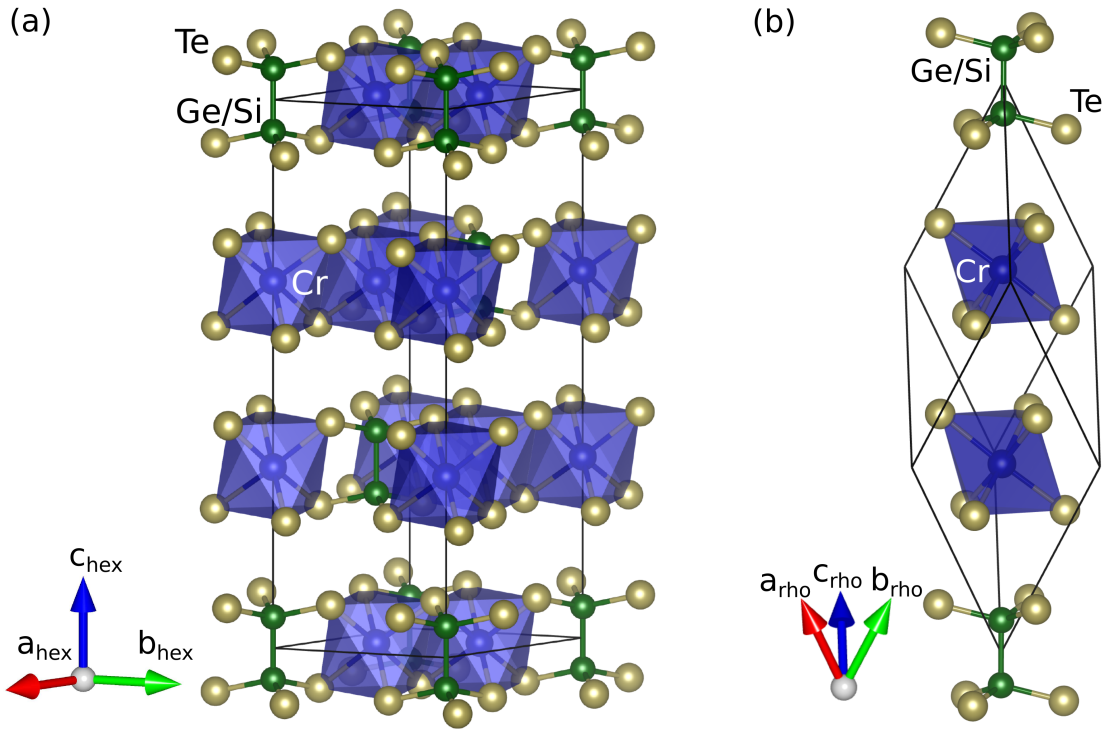

Figure 1.6: Crystal structure of $CrSiTe_3$ or $CrGeTe_3$ with distorted triangular prism made by central Cr atom and surrounding 6 Te atoms. (a) Conventional unit cell with axes of hexagonal coordinate system, (b) Primitive unit cell with axes of rhombohedral coordinate system,.

Chapter 2

Density functional theory

Density functional theory (DFT) is the theory for solving correlated many-body systems, of which the fundamental tenet is an assumption that any property of many interacting particles system can be given by the functional of the ground state density. The advantage of DFT that makes it becoming one of the primary tool for electronic structure calculation is that comparing with earlier theories DFT approaches a method to treat independent particles. The extraordinary successes of approximation are local density approximation (LDA) and generalized gradient approximation (GGA) [37].

The origin of DFT is started from the paper by P. Hohenberg and W. Kohn in 1964, in which they proposed an significant characteristic in quantum many-body system that is the density can be a "basic variable", namely all properties of the system can be considered as a unique functionals of the ground state density [38]. Then, after one year, their construct is extended to finite temperature by Mermin [39]. Meanwhile in 1965 W. Kohn and L. J. Sham delivered their famous paper in which they gave the formulation of DFT that becomes the basis being used in today's studies [40].

2.1 Hohenberg–Kohn theorem

The starting point of interacting many-body system is the basic Hamiltonian for the system of electrons and nuclei written as

$$\begin{aligned}\hat{H} &= -\frac{\hbar^2}{2m_e}\sum_i \nabla_i^2 - \sum_{i,I}\frac{Z_I e^2}{|\mathbf{r}_i - \mathbf{R}_I|} + \frac{1}{2}\sum_{i\neq j}\frac{e^2}{|\mathbf{r}_i - \mathbf{r}_j|} \\ &\quad - \sum_I \frac{\hbar^2}{2M_I}\nabla_I^2 + \frac{1}{2}\sum_{I\neq J}\frac{Z_I Z_J e^2}{|\mathbf{R}_I - \mathbf{R}_J|},\end{aligned} \tag{2.1}$$

where electrons are denoted by lower case subscripts, i and j, and nuclei are denoted by upper case subscripts, I and J, with charge Z_I and mass M_I.

Then the most important progress by Hohenberg and Kohn in Ref. [38] is that they formulate DFT as an exact theory of many-body systems. The Hamiltonian is

$$\hat{H} = -\frac{\hbar^2}{2m_e}\sum_i \nabla_i^2 + \sum_i V_{\text{ext}}(\mathbf{r}_i) + \frac{1}{2}\sum_{i\neq j}\frac{e^2}{|\mathbf{r}_i - \mathbf{r}_j|}, \tag{2.2}$$

where V_{ext} is an external potential of the system of interacting particles. There are two basic theorems of DFT first proved by Hohenberg and Kohn, which will be discussed as follow:

Theorem I: For any system of interacting particles in an external potential $V_{\text{ext}}(\mathbf{r})$, the potential $V_{\text{ext}}(\mathbf{r})$ is determined uniquely, except for a constant, by the ground state particle density $n_0(\mathbf{r})$.

Corollary I: When the Hamiltonian is fully determined, except for a constant shift of the energy, then the many-body wavefunction for all states, ground and excited, are determined. Therefore all properties of the system are completely determined by giving only the ground state density $n_0(\mathbf{r})$.

Proof. It is assumed that there are two different external potentials $V_{\text{ext}}^{(1)}(\mathbf{r})$ and $V_{\text{ext}}^{(2)}(\mathbf{r})$ which are different more than a constant but lead to the same ground state density $n(\mathbf{r})$. Then the two different external potentials give different Hamiltonians, $\hat{H}^{(1)}$ and $\hat{H}^{(2)}$ with different ground state wavefunction, $\Psi^{(1)}$ and $\Psi^{(2)}$ that are hypothesized to have the same ground state density $n_0(\mathbf{r})$.

Because $\Psi^{(2)}$ is not the ground state of $\hat{H}^{(1)}$, assuming that the ground state is non-degenerate there is

$$E^{(1)} = \left\langle \Psi^{(1)} \middle| \hat{H}^{(1)} \middle| \Psi^{(1)} \right\rangle < \left\langle \Psi^{(2)} \middle| \hat{H}^{(1)} \middle| \Psi^{(2)} \right\rangle. \tag{2.3}$$

Rewriting the $\Psi^{(2)}$ term

$$\begin{aligned}\left\langle\Psi^{(2)}\middle|\hat{H}^{(1)}\middle|\Psi^{(2)}\right\rangle &= \left\langle\Psi^{(2)}\middle|\hat{H}^{(2)}\middle|\Psi^{(2)}\right\rangle + \left\langle\Psi^{(2)}\middle|\hat{H}^{(1)}-\hat{H}^{(2)}\middle|\Psi^{(2)}\right\rangle \\ &= E^{(2)} + \int \mathrm{d}^3r \left[V_{\mathrm{ext}}^{(1)}(\mathbf{r}) - V_{\mathrm{ext}}^{(2)}(\mathbf{r})\right] n_0(\mathbf{r}), \end{aligned} \tag{2.4}$$

thus,

$$E^{(1)} < E^{(2)} + \int \mathrm{d}^3r \left[V_{\mathrm{ext}}^{(1)}(\mathbf{r}) - V_{\mathrm{ext}}^{(2)}(\mathbf{r})\right] n_0(\mathbf{r}). \tag{2.5}$$

On the other hand, if the notation (1) and (2) are exchanged in Eq. 2.3 still inequality holds. Similarly we have

$$E^{(2)} < E^{(1)} + \int \mathrm{d}^3r \left[V_{\mathrm{ext}}^{(2)}(\mathbf{r}) - V_{\mathrm{ext}}^{(1)}(\mathbf{r})\right] n_0(\mathbf{r}). \tag{2.6}$$

Summing up Eq. 2.5 and Eq. 2.6, there is $E^{(1)} + E^{(2)} < E^{(2)} + E^{(1)}$. Then it is clear that it is impossible two different external potentials $V_{\mathrm{ext}}^{(1)}(\mathbf{r})$ and $V_{\mathrm{ext}}^{(2)}(\mathbf{r})$ being given by a same non-degenerate ground state density $n(\mathbf{r})$. By *reductio ad absurdum*, it is proofed that the potential $V_{\mathrm{ext}}(\mathbf{r})$ is determined uniquely by the ground state particle density $n_0(\mathbf{r})$.

Theorem II: For the energy $E[n]$ in the terms of density $n(\mathbf{r})$, a universal energy functional can be defined, which is valid for any external potential $V_{\mathrm{ext}}(\mathbf{r})$. For any particular external potential $V_{\mathrm{ext}}(\mathbf{r})$, the exact ground state energy of the system is the global minimum value of this functional and the density $n(\mathbf{r})$ that minimizes the value of the energy functional is the exact ground state density $n_0(\mathbf{r})$ of the system.

Corollary II: The functional $E[n]$ alone is sufficient to determine the exact ground state energy and density.

Proof. To prove second theorem the meaning of a functional of the density has to be defined carefully and the space of density has to be restricted. In first theorem it is proven that all properties can be determined and constructed as functionals of unique ground state densities $n(\mathbf{r})$, which is called "V-representable" ground state densities of the electron Hamiltonian with external potential V_{ext}. Eq. 2.7 is the total energy functional:

$$\begin{aligned} E_{\mathrm{HK}}[n] &= T[n] + E_{\mathrm{int}}[n] + \int \mathrm{d}^3r V_{\mathrm{ext}}(\mathbf{r}) n(\mathbf{r}) + E_{II} \\ &\equiv F_{\mathrm{HK}}[n] + \int \mathrm{d}^3r V_{\mathrm{ext}}(\mathbf{r}) n(\mathbf{r}) + E_{II} \end{aligned} \tag{2.7}$$

where labels "HK" denote the Hohenberg−Kohn theorem, and E_{II} is the interaction energy of the nuclei. F_{HK} including all internal energies, *i.e.* kinetic energy and potential, of the interacting electron system as

$$F_{\mathrm{HK}}[n] = T[n] + E_{\mathrm{int}}[n], \tag{2.8}$$

which must be universal by construction since the kinetic energy and interaction energy of the particles are functionals only of the density. $[n]$ denotes a functional of the density $n(\mathbf{r}, \sigma)$ which depends upon both position in space $\mathbf{r}$ and spin σ.

Considering the a system of the ground state density $n^{(1)}(\mathbf{r})$ with external potential $V_{\mathrm{ext}}^{(1)}(\mathbf{r})$, the Eq. 2.7 is equal to the expectation value of the Hamiltonian in the unique ground state with wavefunction $\Psi^{(1)}$

$$E^{(1)} = E_{\mathrm{HK}}[n^{(1)}] = \left\langle \Psi^{(1)} \middle| \hat{H}^{(1)} \middle| \Psi^{(1)} \right\rangle. \tag{2.9}$$

Then considering a different density $n^{(2)}(\mathbf{r})$ with wavefunction $\Psi^{(2)}$, it is clear that the energy $E^{(2)}$ is larger than $E^{(1)}$:

$$E^{(1)} = \left\langle \Psi^{(1)} \middle| \hat{H}^{(1)} \middle| \Psi^{(1)} \right\rangle < \left\langle \Psi^{(2)} \middle| \hat{H}^{(1)} \middle| \Psi^{(2)} \right\rangle = E^{(2)}. \tag{2.10}$$

It is indicated that the minimum energy is given by the corresponding unique ground state density.

2.2 Kohn−Sham auxiliary system

DFT can be the exact theory of many-body systems since in principle the ground state density determines everything that is proved in the last section. However it is still a unfeasible many-body method because there is a great challenge to calculate excited state properties. Nevertheless as mentioned before nowadays DFT is the most widely used method for electronic structure calculations that is due to the approach proposed by Kohn and Sham in 1965. They gave the *ansatz* to remove the original many-body interacting problem by an auxiliary independent-particle problem and proved that formally it is possible to replace the many-electron problem by an exactly equivalent set of self-consistent one-electron equations [40]. This approach is remarkably successful because it involves independent particles but an interacting density, namely single-particle wavefunctions in a smaller Hilbert space, that is much easier to solve. Thus the approach of Kohn−Sham auxiliary system will be discussed in this section.

The basic interacting many-body system obeying the Hamiltonian (Eq. 2.1) can be replaced by Kohn−Sham approach with auxiliary system and solved more easily.

In their *ansatz*, the most basic idea is that the ground state density of the original interacting system is equal to that of some chosen non-interacting system. Thus all the difficult many-body terms can be incorporated into an exchange-correlation functional of the density, which leads to independent-particle equations for the non-interacting system that is exactly solvable, in practice numerically [37].

For proof, first it should be noticed that Kohn−Sham approach of an auxiliary system rests upon two assumptions:

Assumption 1. The exact ground state density can be represented by the ground state density of an auxiliary system of non-interacting particles, which is also called "non-interacting-V-representability".

Assumption 2. The auxiliary hamiltonian is chosen to have the usual kinetic operator and an effective local potential $V_{\text{eff}}^{\sigma}(\mathbf{r})$ acting on an electron of spin σ at $\mathbf{r}$.

Then on this auxiliary independent-particle system the auxiliary hamiltonian of actual calculations is

$$\hat{H}_{\text{aux}}^{\sigma} = -\frac{1}{2}\nabla^2 + V^{\sigma}(\mathbf{r}), \tag{2.11}$$

where Hartree atomic units, $\hbar = m_e = e = 4\pi/\epsilon_0 = 1$, are used and in order to define functionals for a range of densities the form of $V^{\sigma}(\mathbf{r})$ have to be used for all $V^{\sigma}(\mathbf{r})$ in the range, namely it is unspecified. Considering in a $N = N^{\uparrow} + N^{\downarrow}$ system independent electrons obey the hamiltonian 2.11, in which for ground state there is one electron in each of the N^{σ} orbitals $\psi_i^{\sigma}(\mathbf{r})$ with lowest eigenvalues ϵ_i^{σ}. The density of the auxiliary system is

$$n(\mathbf{r}) = \sum_{\sigma} n(\mathbf{r}, \sigma) = \sum_{\sigma} \sum_{i=1}^{N^{\sigma}} |\psi_i^{\sigma}(\mathbf{r})|^2, \tag{2.12}$$

which is the sums of squares of the orbitals for each spin. Then the independent-particle kinetic energy T_s is written as

$$T_s = -\frac{1}{2} \sum_{\sigma} \sum_{i=1}^{N^{\sigma}} \langle \psi_i^{\sigma} | \nabla^2 | \psi_i^{\sigma} \rangle = \frac{1}{2} \sum_{\sigma} \sum_{i=1}^{N^{\sigma}} \int \mathrm{d}\mathbf{r} |\nabla \psi_i^{\sigma}(\mathbf{r})|^2. \tag{2.13}$$

Thus, the classical Coulomb interaction energy is defined as

$$E^{\text{CC}} = E_{\text{Hartree}} + \int \mathrm{d}\mathbf{r} V_{\text{ext}}(\mathbf{r}) n(\mathbf{r}) + E_{II}, \tag{2.14}$$

where the Hartree energy of the self interacting electron density $n(\mathbf{r})$ is

$$E_{\text{Hartree}}[n] = \frac{1}{2} \int \mathrm{d}\mathbf{r} \mathrm{d}\mathbf{r}' \frac{n(\mathbf{r}) n(\mathbf{r}')}{|\mathbf{r} - \mathbf{r}'|}, \tag{2.15}$$

and E_{II} is the interaction among the positive nuclei. Then this Kohn−Sham approach to the full interacting many-body problem can be rewritten by using independent-particle kinetic energy T_s, classical Coulomb interaction energy E^{CC}, and exchange-correlation energy E_{xc} as

$$\begin{aligned} E_{\mathrm{KS}} &= T_s + E^{\mathrm{CC}} + E_{\mathrm{xc}} \\ &= T_s[n] + \int \mathrm{d}\mathbf{r} V_{\mathrm{ext}}(\mathbf{r}) n(\mathbf{r}) + E_{\mathrm{Hartree}}[n] + E_{II} + E_{\mathrm{xc}}[n]. \end{aligned} \tag{2.16}$$

where V_{ext} is the external potential of the nuclei and any other external fields, $\int \mathrm{d}\mathbf{r} V_{\mathrm{ext}}(\mathbf{r}) n(\mathbf{r})$ is the interaction of the electrons with the nuclei, and E_{II} is the interaction between the nuclei. In this case, E^{CC} is regarded as neutral grouping formed by terms V_{ext}, E_{Hartree}, and E_{II}. $[n]$ denotes a functional of the density $n(\mathbf{r}, \sigma)$ for T_s, E_{Hartree}, and E_{xc}. Especially for each spin, independent-particle kinetic energy T_s must be a unique functional of the density $n(\mathbf{r}, \sigma)$, even if it is given as a functional of the orbitals. Moreover, exchange-correlation energy E_{xc} contains all many-body effects of exchange and correlation. Comparing the Kohn−Sham (Eq. 2.16), Hohenberg−Kohn (Eq. 2.7), and the energy functional $E = E_{\mathrm{HK}}[n, s] \equiv E'_{\mathrm{HK}}[n]$, expressions for the total energy shows that E_{xc} can be written in terms of the Hohenberg−Kohn functional (Eq. 2.8) as

$$\begin{aligned} E_{\mathrm{xc}}[n] &= F_{\mathrm{HK}}[n] - (T_s[n] + E_{\mathrm{Hartree}}[n]) \\ &= T[n] + E_{\mathrm{int}}[n] - (T_s[n] + E_{\mathrm{Hartree}}[n]) \\ &= \langle \hat{T} \rangle - T_s[n] + \langle \hat{V}_{\mathrm{int}} \rangle - E_{\mathrm{Hartree}}[n]. \end{aligned} \tag{2.17}$$

The result derived from Eq. 2.17 means that E_{xc} is given by two differences. One is the difference of kinetic energies, and another one is the difference of internal interaction potential energies of the true interacting many-body system from the fictitious independent-particle system and electron-electron interactions replaced by the Hartree energy. If the universal functionals $E_{\mathrm{xc}}[n]$ defined in Eq. 2.17 were known, the exact ground state energy and density of the many-body electron problem could be found by solving the Kohn−Sham equations for independent-particles.

After foregoing preparation we can consider a feasible way to solve the ground state of Kohn− Sham auxiliary system. Solution of the Kohn−Sham auxiliary system for ground state can be viewed as the problem of minimization with respect to either the density $n(\mathbf{r}, \sigma)$ or the effective potential. Depending on Eq. 2.13-2.15 and 2.17 it can be found that except T_s other terms in Eq. 2.16 are considered to be functionals of the density, and T_s is expressed as a functional of the orbitals. By varying the

wavefunctions and using the chain rule, the variational equation is derived as

$$\frac{\delta E_{\mathrm{KS}}}{\delta \psi_i^{\sigma *}(\mathbf{r})} = \frac{\delta T_s}{\delta \psi_i^{\sigma *}(\mathbf{r})} + \left[\frac{\delta E_{\mathrm{ext}}}{\delta n(\mathbf{r},\sigma)} + \frac{\delta E_{\mathrm{Hartree}}}{\delta n(\mathbf{r},\sigma)} + \frac{\delta E_{\mathrm{xc}}}{\delta n(\mathbf{r},\sigma)} \right] \frac{\delta n(\mathbf{r},\sigma)}{\delta \psi_i^{\sigma *}(\mathbf{r})} = 0, \tag{2.18}$$

and it subjects to the orthonormalization constraints

$$\left\langle \psi_i^{\sigma} \middle| \psi_j^{\sigma'} \right\rangle = \delta_{i,j}\delta_{\sigma,\sigma'}. \tag{2.19}$$

Excepting the dependence of E_{Hartree} and E_{xc} on n, it is equivalent to the general derivation of the Schrödinger equation, which is also equivalent to the Rayleigh−Ritz principle [41, 42].

Substituting T_s and $n(\mathbf{r},\sigma)$ by using Eq. 2.12 and 2.13, formulas,

$$\frac{\delta T_s}{\delta \psi_i^{\sigma *}(\mathbf{r})} = -\frac{1}{2}\nabla^2 \psi_i^{\sigma}(\mathbf{r}), \qquad \frac{\delta n(\mathbf{r})}{\delta \psi_i^{\sigma *}(\mathbf{r})} = \psi_i^{\sigma}(\mathbf{r}), \tag{2.20}$$

are gotten. Then by using Lagrange multiplier it leads, a type of Schrödinger-like equation, the Kohn−Sham equations:

$$(H_{\mathrm{KS}}^{\sigma} - \varepsilon_i^{\sigma})\psi_i^{\sigma}(\mathbf{r}) = 0 \tag{2.21}$$

and Kohn−Sham Hamiltonian:

$$\begin{aligned} H_{\mathrm{KS}}^{\sigma}(\mathbf{r}) &= -\frac{1}{2}\nabla^2 + \frac{\delta E_{\mathrm{ext}}}{\delta n(\mathbf{r},\sigma)} + \frac{\delta E_{\mathrm{Hartree}}}{\delta n(\mathbf{r},\sigma)} + \frac{\delta E_{\mathrm{xc}}}{\delta n(\mathbf{r},\sigma)} \\ &= -\frac{1}{2}\nabla^2 + V_{\mathrm{ext}}(\mathbf{r}) + V_{\mathrm{Hartree}}(\mathbf{r}) + V_{\mathrm{xc}}^{\sigma}(\mathbf{r}) \\ &= -\frac{1}{2}\nabla^2 + V_{\mathrm{KS}}^{\sigma}(\mathbf{r}) \end{aligned} \tag{2.22}$$

where ε_i are eigenvalues. Formally Kohn−Sham equation (Eq. 2.21) is analogous to the full many-body Schrödinger equation, but Kohn−Sham equation is much easier to solve because only single-particle wavefunctions effectively coupled through the exchange-correlation potential $V_{\mathrm{xc}}^{\sigma}(\mathbf{r})$ are involved.

The exchange-correlation potential $V_{\mathrm{xc}}^{\sigma}(\mathbf{r})$ is the functional derivative of E_{xc} which can be written as

$$V_{\mathrm{xc}}^{\sigma}(\mathbf{r}) = \epsilon_{\mathrm{xc}}([n],\mathbf{r}) + n(\mathbf{r})\frac{\delta \epsilon_{\mathrm{xc}}([n],\mathbf{r})}{\delta n(\mathbf{r},\sigma)}, \tag{2.23}$$

where $\epsilon_{\rm xc}([n], \mathbf{r})$ is an energy per electron at point $\mathbf{r}$ and a functional only depends upon the density $n(\mathbf{r}', \sigma')$ in some neighborhood of point $\mathbf{r}$, which is defined by the expression of $E_{\rm xc}$ as follow,

$$E_{\rm xc}[n] = \int \mathrm{d}\mathbf{r}\ n(\mathbf{r})\epsilon_{\rm xc}\left([n], \mathbf{r}\right). \tag{2.24}$$

Kohn−Sham equations (Eq. 2.21-2.22) are independent of any approximation to the functional $E_{\rm xc}[n]$. Thus, as mentioned before, when the universal functional $E_{\rm xc}[n]$ are known the exact ground state can be found for the interacting system. Moreover when an approximate form for $E_{\rm xc}[n]$ describes the true exchange-correlation energy, the Kohn−Sham method provides a feasible approach to calculating the ground state properties of the many-body electron system.

2.3 Generalized-gradient approximations

In previous section, we discuss two-fold genius of Kohn−Sham auxiliary system. One is the construction of an auxiliary system that derives tractable independent-particle equations for solving interacting many-body problems. Another one, perhaps more important one, is by separating out the independent-particle kinetic energy and the long-range Hartree terms explicitly the remaining exchange-correlation energy $E_{\rm xc}[n]$, which expressed as a functional of the density, can be approximated as a local or nearly local functional of the density reasonably. Generally the exact functional $E_{\rm xc}[n]$ must be very complex. Thus there are some great works to make a remarkable simplification for the approximation of $E_{\rm xc}[n]$. Two most important approximate functionals are local density approximation (LDA) and generalized-gradient approximations (GGAs). In this section, we mainly discuss the generalized-gradient approximations (GGAs).

However before GAAs, we have to have a little discussion about LDA. The limit already pointed out by Kohn and Sham is it can often be considered that solids is close to the limit of the homogeneous electron gas. The limit let us learn about that the effects of exchange and correlation are local in character, which makes the local density approximation (LDA), more generally the local spin density approximation (LSDA). For LSDA, the exchange-correlation energy is written as a simple integral over all space with the exchange–correlation energy density at each point assumed

to be the same as in a homogeneous electron gas with that density,

$$\begin{aligned} E_{\rm xc}^{\rm LSDA}[n^\uparrow, n^\downarrow] &= \int {\rm d}^3 r n(\mathbf{r}) \epsilon_{\rm xc}^{\rm hom}(n^\uparrow(\mathbf{r}), n^\downarrow(\mathbf{r})) \\ &= \int {\rm d}^3 r n(\mathbf{r}) [\epsilon_x^{\rm hom}(n^\uparrow(\mathbf{r}), n^\downarrow(\mathbf{r})) + \epsilon_c^{\rm hom}(n^\uparrow(\mathbf{r}), n^\downarrow(\mathbf{r}))], \end{aligned} \quad (2.25)$$

where LSDA is formulated in terms either two spin densities $n^\uparrow(\mathbf{r})$ and $n^\downarrow(\mathbf{r})$, or they can be rewritten as the total density $n(\mathbf{r})$ and the fractional spin polarization $\zeta(\mathbf{r}) = \frac{n^\uparrow(\mathbf{r}) - n^\downarrow(\mathbf{r})}{n(\mathbf{r})}$. For unpolarized systems the LDA is simplified by $n^\uparrow(\mathbf{r}) = n^\downarrow(\mathbf{r}) = n(\mathbf{r})/2$.

The LSDA is a successful general local approximation and it would stimulate ideas for constructing improved functionals such as GGAs.

The development of various GGAs was led by LSDA and it overtook LSDA in several different cases with marked improvement. At the outset of progress, a functional of the magnitude of the gradient of the density $|\nabla^m n^\sigma|$ with the n for all points is beyond the local approximation, such as gradient expansion approximation (GEA). However GEA is not good enough because it violates the sum rules [43], which often leads to worse results. The basic problem is that in real materials gradients are too large than leads the expansion to break down.

The GGA term denotes a variety of methods to propose the modified behavior of functions at large gradients and preserve desired properites. There is a convenient way [44] to describe exchange-correlation energy $E_{\rm xc}[n]$ as the GGA form:

$$\begin{aligned} E_{\rm xc}^{\rm GGA}[n^\uparrow, n^\downarrow] &= \int {\rm d}^3 r n(\mathbf{r}) \epsilon_{\rm xc}(n^\uparrow, n^\downarrow, |\nabla n^\uparrow|, |\nabla n^\downarrow|, |\nabla^2 n^\uparrow|, |\nabla^2 n^\downarrow|, ...) \\ &\equiv \int {\rm d}^3 r n(\mathbf{r}) \epsilon_x^{\rm hom}(n) F_{\rm xc}(n^\uparrow, n^\downarrow, |\nabla n^\uparrow|, |\nabla n^\downarrow|, |\nabla^2 n^\uparrow|, |\nabla^2 n^\downarrow|, ...), \end{aligned} \quad (2.26)$$

where $F_{\rm xc}$ is dimensionless and $\epsilon_x^{\rm hom}(n)$ is the exchange energy of the unpolarized homogeneous electron gas. Due to the spin-scaling relation of exchange, $E_x[n^\uparrow, n^\downarrow] = 1/2 \left[E_x[2n^\uparrow] + E_x[n^\downarrow]\right]$, where $E_x[n]$ is the exchange energy for an unpolarized system of density $n(\mathbf{r})$, only the spin-unpolarized $F_x(n, |\nabla n|, ...)$ is necessary to be considered. Numerous forms F_x are proposed, but mainly for first-order variation in density normalized $F_x(n, |\nabla n|)$ are widely used. There are three well-known $F_x(n, |\nabla n|)$ forms which are Becke (B88) [45], Perdew and Wang (PW91) [46], and Perdew, Burke, and Enzerhof (PBE) [47]. Low-order cases of these forms are relevant for most physical applications, and different GGAs give similar improvement for many systems with small density gradient contributions by their nearly identical shapes. All these GGAs lead to lower exchange energies than LDA. For instance, rapidly

varying density regions in atoms than in condensed matter result in greater lowering of the exchange energy in atoms than in molecules and solids. This reduction of binding energy is one of the most important characteristics of GGAs nowadays for correcting LDA overbinding and improving agreement with experiments [48]. However for F_x in high-order it is a fact that different physical conditions lead to very different behaviors of F_x, which reflects not only the lack of knowledge of the large density gradient regions but also inherent difficulty of the density gradient expansion that one form of GGA shows the correct result for a certain physical property while others fail. This is a problem that it cannot be guaranteed that F_x form is superior for other properties namely different physical conditions, which will be the topic in future studies.

2.4 Full-potential local-orbital minimum-basis

Full-potential band-structure scheme based on the linear combination of overlapping nonorthogonal orbitals, namely full-potential local-orbital (FPLO) method, is an all-electron full-potential method to represent numerical solution of the Kohn −Sham equation, which is presented by Koepernik and Eschrig in 1999 [49].

FPLO is based on the DFT with Kohn−Sham approach that is mentioned in section 2.2. For solving this problem, there are two tasks. One is the solution of the Kohn−Sham equation, and another one is treatment of real space functions such as density and potential. To realize Kohn−Sham approach numerically, a significant step is to construct both the Kohn−Sham wavefunctions and the density/potential by similar means. In FPLO a linear combination of overlapping local orbitals is used to construct the Kohn−Sham solution, in which the localized overlapping potential contributions to represent the crystal potential is implied.

Firstly, the nonorthogonal local-orbital basis is discussed. A crystal potential decomposed as

$$\nu(\mathbf{r}) = \sum_{\mathbf{R}+\mathbf{s},L} \nu_{\mathbf{s},L}(|\mathbf{r}-\mathbf{R}-\mathbf{s}|)Y_L(\mathbf{r}-\mathbf{R}-\mathbf{s}) \tag{2.27}$$

by real spherical harmonics Y_L, where $\nu_{\mathbf{s},L}$ are local potentials. A representation of the extended crystal states is needed to solve the Kohn−Sham equations, in which it is a nonorthogonal local-orbital representation. The extended states are expanded in terms of localized atomiclike basis orbitals

$$\langle \mathbf{r}|\mathbf{R}\mathbf{s}L\rangle = \phi^l_{\mathbf{s}}(|\mathbf{r}-\mathbf{R}-\mathbf{s}|)Y_L(\mathbf{r}-\mathbf{R}-\mathbf{s}). \tag{2.28}$$

Then there is an ansatz that extended state labeled by crystal momentum $\mathbf{k}$ and band index n is constructed as a linear combinations of Bloch sums:

$$|\mathbf{k}n\rangle = \sum_{\mathbf{R}\mathbf{s}L} |\mathbf{R}\mathbf{s}L\rangle \, c_{L\mathbf{c}}^{\mathbf{k}n} e^{i\mathbf{k}(\mathbf{R}+\mathbf{s})}. \tag{2.29}$$

It is noticeable that there is no distinction between core and valence orbitals, namely all-electron treatment. Next inserting the Eq. 2.29 into the Kohn−Sham equation Eq. 2.21

$$H\,|\mathbf{k}n\rangle = |\mathbf{k}n\rangle\, \varepsilon_{\mathbf{k}n} \tag{2.30}$$

yields

$$\sum_{\mathbf{R}\mathbf{s}L} [\langle \mathbf{0}\mathbf{s}'L'|\, H\, |\mathbf{R}\mathbf{s}L\rangle - \langle \mathbf{0}\mathbf{s}'L'|\mathbf{R}\mathbf{s}L\rangle\, \varepsilon_{\mathbf{k}n}] c_{L\mathbf{c}}^{\mathbf{k}n} e^{i\mathbf{k}(\mathbf{R}+\mathbf{s})}, \tag{2.31}$$

where the first term is Hamiltonian and second term is overlap matrices:

$$H_{\mathbf{0}\mathbf{s}'\mathbf{R}\mathbf{s}}^{L'L} = \langle \mathbf{0}\mathbf{s}'L'|\, H\, |\mathbf{R}\mathbf{s}L\rangle\,, \tag{2.32}$$

$$S_{\mathbf{0}\mathbf{s}'\mathbf{R}\mathbf{s}}^{L'L} = \langle \mathbf{0}\mathbf{s}'L'|\mathbf{R}\mathbf{s}L\rangle\,. \tag{2.33}$$

It can be further simplified by the core-valence distinction. Core orbitals $|\mathbf{R}\mathbf{s}c\rangle$ obey

$$\langle \mathbf{R}'\mathbf{s}'c'|\mathbf{R}\mathbf{s}c\rangle = \delta_{c'c}\delta_{\mathbf{R}'+\mathbf{s}',\mathbf{R}+\mathbf{s}}, \tag{2.34}$$

$$H\,|\mathbf{R}\mathbf{s}c\rangle = |\mathbf{R}\mathbf{s}c\rangle\, \varepsilon_{\mathbf{s}c}. \tag{2.35}$$

Core orbital is strongly localized and does not noticeably deform. Then depending on Eq. 2.34, the overlap matrix contains four blocks:

$$S = \begin{pmatrix} S_{cc} & S_{cv} \\ S_{vc} & S_{vv} \end{pmatrix} = \begin{pmatrix} \langle \mathbf{R}'\mathbf{s}'c'|\mathbf{R}\mathbf{s}c\rangle & \langle \mathbf{R}'\mathbf{s}'c'|\mathbf{R}\mathbf{s}v\rangle \\ \langle \mathbf{R}'\mathbf{s}'v'|\mathbf{R}\mathbf{s}c\rangle & \langle \mathbf{R}'\mathbf{s}'v'|\mathbf{R}\mathbf{s}v\rangle \end{pmatrix}, \tag{2.36}$$

where c and v are subscripts for core orbitals and valence orbitals separately. Now the Hamiltonian matrix can be simplified as

$$H = \begin{pmatrix} H_{cc} & H_{cc}S_{cv} \\ S_{cv}^{\dagger}H_{cc} & H_{vv} \end{pmatrix} \tag{2.37}$$

where matrix elements are

$$H_{cc} = \langle \mathbf{R}'\mathbf{s}'c' | \, H \, | \mathbf{R}\mathbf{s}c \rangle = \varepsilon_{\mathbf{s}c}\delta_{c'c}\delta_{\mathbf{R}'+\mathbf{s}',\mathbf{R}+\mathbf{s}}, \tag{2.38}$$
$$H_{vv} = \langle \mathbf{R}'\mathbf{s}'v' | \, H \, | \mathbf{R}\mathbf{s}v \rangle \, .$$

For reducing the dimension of the problem, an algebraic transformation is introduced to make a special form of Eq. 2.36 and 2.37. Due to the core-core block of S is the unit matrix, a simplified Cholesky decomposition of S is performed as

$$S = S^l S^r = \begin{pmatrix} 1 & 0 \\ S^l_{vc} & S^l_{vv} \end{pmatrix} \begin{pmatrix} 1 & S^r_{vc} \\ 0 & S^r_{vv} \end{pmatrix}, \tag{2.39}$$

with implied relations:

$$S_{vc} = S^l_{vc} = S^{r\dagger}_{cv} = S^\dagger_{cv}, \quad S^l_{vv} S^r_{vv} = S_{vv} - S_{vc} S_{cv}.$$

The inverse of this Cholesky decomposition is

$$S^{l-1} = \begin{pmatrix} 1 & 0 \\ -S^{l-1}_{vv} S_{vc} & S^{l-1}_{vv} \end{pmatrix}, \quad S^{r-1} = \begin{pmatrix} 1 & -S_{cv} S^{r-1}_{vv} \\ 0 & S^{r-1}_{vv} \end{pmatrix}. \tag{2.40}$$

Then by defining $c^{\mathbf{k}n}_{L\mathbf{c}}$ is the matrix elements of C and $E = diag(\varepsilon_{\mathbf{k}n})$, the Eq. 2.31 becomes

$$HC = SCE. \tag{2.41}$$

By using unitary matrix $D = S^r C$, it can be rewritten as

$$S^{l-1} H S^{r-1} D = DE, \tag{2.42}$$

where $S^{l-1}HS^{r-1}$ is diagonalized by D. Because the core-core block of $S^{l-1}HS^{r-1}$ is already diagonal and core-valence block vanishes by considering Eq. 2.37 and 2.40, we can get $D_{cc} = 1$ and $D_{cv} = D_{vc} = 0$. Thus the eigenvalue problem of Eq. 2.31 is reduced into

$$S^{l-1}_{vv}(H - S_{vc} H_{cc} S_{vc}) S^{r-1}_{vv} D_{vv} = D_{vv} E_v. \tag{2.43}$$

The wavefunction coefficient matrix C is obtained as

$$C = S^{r-1} D = \begin{pmatrix} 1 & -S_{cv} S^{r-1}_{vv} D_{vv} \\ 0 & S^{r-1}_{vv} D_{vv} \end{pmatrix}. \tag{2.44}$$

2.5 Virtual crystal approximation

For studying electronic structure of disordered alloys, solid solutions, and some doping materials by the application of DFT calculation, it is required to find some approximation for the treatment of the alloy disorder. A direct approach is to make use of the supercell approximation, namely using one or more disordered configurations in a supercell with artificially imposed periodic boundary conditions. Such calculations require a very large supercells in order to mimic the distribution of local chemical environments, which will leads an extremely heavy calculation. Thus, a much simpler and computationally less expensive approach is to employ the virtual crystal approximation (VCA) in which one studies a crystal with the primitive periodicity, but composed of fictitious virtual atoms that interpolate between the behavior of the atoms in the parent compounds [50]. This technique has seen wide use in DFT calculations.

Chapter 3

Random phase approximation

At first the study of spin fluctuations was started round the magnetic instability or in the quantum critical regime as the problem of weak itinerant ferro- and antiferromagnetism in the early 1970s [51]. This theory resolved the classical difficulties of the Stoner theory that a new mechanism for the Curie–Weiss (CW) susceptibility without local moment was presented and the Curie temperature was corrected properly. Then the singular behaviours and/or quantum critical indices at the magnetic instabilities at absolute zero temperature was predicted. Furthermore it was found that anomalous behaviours discovered in the two-dimensional electron systems in the cuprates could be interpreted. Superconductivity was also included, namely that T_c was evaluated successfully and the symmetry of the order parameter was confirmed, which was regarded as the spin fluctuations induced superconductivity [52]. Thus, the spin fluctuation mechanism is considered to be at least one promising choice for the central mechanism of strong correlation electron systems including strongly correlated superconductors [53].

The random phase approximation (RPA) was proposed as one of the schemes to realize spin fluctuation theory, which is used to calculate properties of electronic systems with a high density [54]. In this chapter, we will apply the PRA to the multi-orbital Hubbard model and obtain some physical quantities.

3.1 Hamiltonian of Hubbard model

We will start the derivation from the multi-orbital Hubbard-Hund Hamiltonian [55] described as

$$H = H_0 + H_I. \tag{3.1}$$

H_0 is tight-binding Hamiltonian described as

$$H_0 = \sum_{\varrho} \sum_{ij} \sum_{\ell\ell'} t_{ij}^{\ell\ell'} c_{i\ell\varrho}^{\dagger} c_{j\ell'\varrho}, \tag{3.2}$$

where $t_{ij}^{\ell\ell'}$ are the hoppings connecting sites i and j for orbitals ℓ and ℓ', and H_I is

$$\begin{aligned} H_I &= U \sum_{i,\ell} n_{i\ell\uparrow} n_{i\ell\downarrow} + \frac{U'}{2} \sum_{i,\ell,\ell'\neq\ell} n_{i\ell} n_{i\ell'} \\ &\quad - \frac{J}{2} \sum_{i,\ell,\ell'\neq\ell} \mathbf{S}_{i\ell} \cdot \mathbf{S}_{i\ell'} \\ &\quad + \frac{J'}{2} \sum_{i,\ell,\ell'\neq\ell,\varrho} c_{i\ell\varrho}^{\dagger} c_{i\ell\bar{\varrho}}^{\dagger} c_{i\ell'\bar{\varrho}} c_{i\ell'\varrho}, \end{aligned} \tag{3.3}$$

where c is the annihilation operator, $\mathbf{S}_{i\ell}$ is spin operator, and U, U', J, J' are interaction parameters of the intraorbital Coulomb repulsion, the interorbital Coulomb repulsion, the Hund's rule coupling, and the pair-hopping term separately. The density operator is given by

$$n_{\ell}(\mathbf{q}) = \sum_{\mathbf{k}\varrho} c_{\ell\varrho}^{\dagger}(\mathbf{k}+\mathbf{q}) c_{\ell\varrho}(\mathbf{k}), \tag{3.4}$$

where ϱ denotes the spin of the electrons, and $\mathbf{k}$ and $\mathbf{q}$ are denotations of momentum.

3.2 Derivation for the non-interacting susceptibility

Using Kubo formula [56], time-ordered expectation value of an operator A_i after a small perturbation of a physical system by operator A_j, where i and j denote a set of quantum number given by

$$\chi_{ij}(\mathbf{q}, \nu_n) = \int_0^{\beta} \mathrm{d}\tau e^{\mathrm{i}\nu_n \tau} \left\langle T_\tau A_i(\mathbf{q}, \tau) A_j(-\mathbf{q}, 0) \right\rangle, \tag{3.5}$$

is defined as the so-called susceptibility χ_{ij} associated with operators A_i and A_j, and it should be noticed that the susceptibility χ_{ij} is a function of momentum $\mathbf{q}$ and bosonic Matsubara frequencies ν_n.

Inserting Eq. 3.4 into Eq. 3.5, the non-interacting charge susceptibility χ_0 is defined as

$$
\begin{aligned}
(\chi_0)^{\ell}_{\ell'}(\mathbf{q}, \mathrm{i}\nu_n) &= \frac{1}{2}\int_0^{\beta} \mathrm{d}\tau e^{\mathrm{i}\nu_n\tau} \left\langle T_\tau n_\ell(\mathbf{q},\tau) n_{\ell'}(-\mathbf{q},0)\right\rangle \qquad (3.6)\\
&= \frac{1}{2}\int_0^{\beta} \mathrm{d}\tau e^{\mathrm{i}\nu_n\tau} \sum_{\mathbf{k}\mathbf{k}'}\sum_{\varrho\varrho'} \\
&\quad \times \left\langle T_\tau c^{\dagger}_{\ell\varrho}(\mathbf{k}+\mathbf{q},\tau) c_{\ell\varrho}(\mathbf{k},\tau) c^{\dagger}_{\ell'\varrho'}(\mathbf{k}'-\mathbf{q},0) c_{\ell'\varrho'}(\mathbf{k}',0)\right\rangle . \qquad (3.7)
\end{aligned}
$$

Because the susceptibility is a two-particle Green's function written on the Matsubara frequency axis as the Fourier transformation of a time-ordered two-particle expectation value, Eq. 3.7 becomes

$$
\begin{aligned}
(\chi_0)^{\ell}_{\ell'}(\mathbf{q}, \mathrm{i}\nu_n) &= \frac{1}{2}\int_0^{\beta} \mathrm{d}\tau e^{\mathrm{i}\nu_n\tau} \sum_{\mathbf{k}\mathbf{k}'}\sum_{\varrho\varrho'} \times [G_{\ell\varrho}(\mathbf{k},0) G_{\ell'\varrho'}(\mathbf{k}',0)\delta_{\mathbf{q},0} \\
&\quad - G_{\ell\varrho}(\mathbf{k}',-\tau) G_{\ell'\varrho'}(\mathbf{k},\tau)\delta_{\mathbf{k}+\mathbf{q},\mathbf{k}'}]\delta_{\varrho,\varrho'}\delta_{\ell\ell'}, \qquad (3.8)
\end{aligned}
$$

where Green's functions are rearranged by applying Wick's theorem (Eq. 3.9) to the time-ordered expectation value.

$$
\begin{aligned}
\langle T(ABCD)\rangle &= \langle T(AB)\rangle \langle T(CD)\rangle + (-1)\langle T(AC)\rangle \langle T(BD)\rangle \\
&\quad + (-1)^3 \langle T(AD)\rangle \langle T(CB)\rangle . \qquad (3.9)
\end{aligned}
$$

Assuming that the Hamiltonian does not allow for change in the orbital quantum numbers ℓ, ℓ' and the spin quantum number ϱ, ϱ', and neglecting the term with $\mathbf{q} = 0$ because the first term in Eq. 3.8 contributes only for $\mathbf{q} = 0$, the Eq. 3.8 becomes

$$
(\chi_0)^{\ell}_{\ell'}(\mathbf{q}, \mathrm{i}\nu_n) = -\frac{1}{2}\int_0^{\beta} \mathrm{d}\tau e^{\mathrm{i}\nu_n\tau} \sum_{\mathbf{k},\varrho\varrho'} G_{\ell'\varrho'}(\mathbf{k},\tau) G_{\ell\varrho}(\mathbf{k}+\mathbf{q},-\tau)\delta_{\varrho\varrho'}\delta_{\ell\ell'}, \qquad (3.10)
$$

which is the non-interacting charge susceptibility with a simple expression and the negative sign is due to time-ordering.

Similarly, for non-interacting spin susceptibility it is defined as

$$
(\chi_1)^{\ell}_{\ell'}(\mathbf{q}, \mathrm{i}\nu_n) = \frac{2}{3}\int_0^{\beta} \mathrm{d}\tau e^{\mathrm{i}\nu_n\tau} \left\langle T_\tau \mathbf{S}_\ell(\mathbf{q},\tau) \cdot S_{\ell'}(-\mathbf{q},0)\right\rangle , \qquad (3.11)
$$

by using generalized Abrikosov pseudo-fermion operators in Eq. 3.12:

$$
\mathbf{S}_\ell(\mathbf{q}) = \frac{1}{2}\sum_{\mathbf{k}\ell\ell'} c^{\dagger}_{\ell\varrho}(\mathbf{k}+\mathbf{q})\boldsymbol{\sigma}_{\varrho\varrho'} c_{\ell\varrho'}, \qquad (3.12)
$$

where $\boldsymbol{\sigma}$ denotes the vector of Pauli matrices given by

$$\begin{aligned}
&\boldsymbol{\sigma} = (\sigma_x, \sigma_y, \sigma_z)\,, \\
&\sigma_x = \begin{pmatrix} 0 & 1 \\ 1 & 0 \end{pmatrix}, \quad \sigma_y = \begin{pmatrix} 0 & -\mathrm{i} \\ \mathrm{i} & 0 \end{pmatrix}, \quad \sigma_z = \begin{pmatrix} 1 & 0 \\ 0 & -1 \end{pmatrix}.
\end{aligned} \tag{3.13}$$

Next the explicit representation of the spin-operator Eq. 3.12 and the Pauli matrices Eq. 3.13 were inserted into Eq. 3.11 with the scalar product of spin-operators and then we can acquire

$$\begin{aligned}
(\chi_1)^{\ell}_{\ell'}(\mathbf{q}, \mathrm{i}\nu_n) \;=\; & \frac{1}{6}\int_0^{\beta} \mathrm{d}\tau e^{\mathrm{i}\nu_n\tau} \sum_{\mathbf{k}\mathbf{k}'\varrho} \\
& \times \Big\langle T_\tau \big[2c^{\dagger}_{\ell\varrho}(\mathbf{k}+\mathbf{q},\tau) c_{\ell\bar{\varrho}}(\mathbf{k},\tau) c^{\dagger}_{\ell'\bar{\varrho}}(\mathbf{k}'-\mathbf{q},0) c_{\ell'\varrho}(\mathbf{k}',0) \\
& + c^{\dagger}_{\ell\varrho}(\mathbf{k}+\mathbf{q},\tau) c_{\ell\varrho}(\mathbf{k},\tau) c^{\dagger}_{\ell'\varrho}(\mathbf{k}'-\mathbf{q},0) c_{\ell'\varrho}(\mathbf{k}',0) \\
& - c^{\dagger}_{\ell\varrho}(\mathbf{k}+\mathbf{q},\tau) c_{\ell\varrho}(\mathbf{k},\tau) c^{\dagger}_{\ell'\bar{\varrho}}(\mathbf{k}'-\mathbf{q},0) c_{\ell'\bar{\varrho}}(\mathbf{k}',0) \big]. \Big\rangle
\end{aligned} \tag{3.14}$$

Again we apply Wick's theorem (Eq. 3.9) and neglect the term with $\mathbf{q} = 0$. There is the non-interacting spin susceptibility with

$$\begin{aligned}
(\chi_1)^{\ell}_{\ell'}(\mathbf{q}, \mathrm{i}\nu_n) \;=\; & -\frac{1}{6}\int_0^{\beta} \mathrm{d}\tau e^{\mathrm{i}\nu_n\tau} \\
& \times \sum_{\mathbf{k}\varrho\varrho'} \left[G_{\ell'\varrho'}(\mathbf{k},\tau) G_{\ell\varrho}(\mathbf{k}+\mathbf{q},-\tau) (\delta_{\varrho\varrho'} + 2\delta_{\varrho\bar{\varrho}'}) \right] \delta_{\ell\ell'},
\end{aligned} \tag{3.15}$$

of which the negative sign is also due to time-ordering. Comparing the expressions for the non-interacting charge susceptibility (Eq. 3.10) and the non-interacting spin susceptibility (Eq. 3.15), it is easy to find that actually they are equal in the paramagnetic case, where $G_{\ell\varrho}$=$G_{\ell\bar{\varrho}}$. Assuming that superconductivity emerges from a paramagnetic metal, the non-interacting paramagnetic susceptibility can be calculated and we can concentrate on it as the central object of our theory. Nevertheless, we cannot neglect the spin quantum number that would lead to diagram counting error in further calculations.

Then the expression for the non-interacting paramagnetic susceptibility will be derived as follow. The unperturbed imaginary-frequency Matsubara Green's function connecting orbitals ℓ and ℓ' in Lehmann representation is

$$G_{\ell\ell'}(\mathbf{k}, \mathrm{i}\omega_n) = \sum_{\lambda} \frac{a^{\ell *}_{\lambda}(\mathbf{k}) a^{\ell'}_{\lambda}(\mathbf{k})}{\mathrm{i}\omega_n - E_{\lambda}}, \tag{3.16}$$

where the summation over electronic bands is indicated by the sum over λ, matrix elements $a_\lambda^\ell(\mathbf{k})$ from the diagonalization of the kinetic part of the Hamiltonian connect orbital and band space, E_λ is the energy eigenvalues of the kinetic Hamiltonian which is assumed that absorbs the chemical potential μ, and the star $*$ denotes the complex conjugate. Considering the Fourier transform of the imaginary-time Green's function

$$G(\lambda,\tau) = \frac{1}{\beta}\sum_n e^{-\mathrm{i}\omega_n\tau} G(\lambda,\mathrm{i}\omega_n), \tag{3.17}$$

and inserting Eq. 3.17 into Eq. 3.10, we get

$$\begin{aligned}
\chi^{\ell_4\ell_2}_{\ell_1\ell_3}(\mathbf{q},\mathrm{i}\nu_n) &= -\frac{1}{\beta^2}\int_0^\beta \mathrm{d}\tau e^{-\mathrm{i}\nu_n\tau}\sum_{\mathbf{k}} \\
&\quad\times\left[\sum_{\omega_n} e^{-\mathrm{i}\omega_n\tau} G_{\ell_4\ell_2}(\mathbf{k},\mathrm{i}\omega_n)\sum_{\omega_n'} e^{\mathrm{i}\omega_n'\tau} G_{\ell_1\ell_3}(\mathbf{k}+\mathbf{q},\mathrm{i}\omega_n')\right] \\
&= -\frac{1}{\beta^2}\int_0^\beta \mathrm{d}\tau e^{-\mathrm{i}\nu_n\tau}\sum_{\boldsymbol{k},\omega_n,\omega_n'} \\
&\quad\times\left[e^{-\mathrm{i}\omega_n\tau} G_{\ell_4\ell_2}(\mathbf{k},\mathrm{i}\omega_n) e^{\mathrm{i}\omega_n'\tau} G_{\ell_1\ell_3}(\mathbf{k}+\mathbf{q},\mathrm{i}\omega_n')\right].
\end{aligned} \tag{3.18}$$

Now Green's function does not depend on time and the integration will be

$$\chi^{\ell_4\ell_2}_{\ell_1\ell_3}(\mathbf{q},\mathrm{i}\nu_n) = -\frac{1}{\beta^2}\sum_{\mathbf{k},\omega_n,\omega_n'} G_{\ell_4\ell_2}(\mathbf{k},\mathrm{i}\omega_n) G_{\ell_1\ell_3}(\mathbf{k}+\mathbf{q},\mathrm{i}\omega_n')\frac{e^{\mathrm{i}\beta(-\nu_n-\omega_n+\omega_n')}-1}{\mathrm{i}(-\nu_n-\omega_n+\omega_n')}. \tag{3.19}$$

Summing over all positive and negative Matsubara frequencies, the fraction in Eq. 3.19 does not contribute, except $-\nu_n = \omega_n - \omega_n'$. The fraction will be

$$\lim_{-\nu_n\to\omega_n-\omega_n'} \frac{e^{\mathrm{i}\beta(-\nu_n-\omega_n+\omega_n')}-1}{\mathrm{i}(-\nu_n-\omega_n+\omega_n')} = \lim_{-\nu_n\to\omega_n-\omega_n'} \frac{\mathrm{i}\beta e^{\mathrm{i}\beta(-\nu_n-\omega_n+\omega_n')}}{\mathrm{i}} = \beta. \tag{3.20}$$

Thus, Eq. 3.19 becomes the non-interacting susceptibility

$$\chi^{\ell_4\ell_2}_{\ell_1\ell_3}(\mathbf{q},\mathrm{i}\nu_n) = -\frac{1}{\beta}\sum_{\mathbf{k},\omega_n} G_{\ell_4\ell_2}(\mathbf{k},\mathrm{i}\omega_n) G_{\ell_1\ell_3}(\mathbf{k}+\mathbf{q},\mathrm{i}\omega_n+\mathrm{i}\nu_n), \tag{3.21}$$

which clearly is a Matsubara sum over a product of Green's functions.

Then by inserting the explicit form of the Matsubara Green's function in orbital space, Eq. 3.21 becomes

$$\begin{aligned}\chi^{\ell_4\ell_2}_{\ell_1\ell_3}(\mathbf{q},\mathrm{i}\nu_n) &= -\frac{1}{\beta}\sum_{\mathbf{k},\omega_n}\sum_{l}\frac{a^{\ell_4*}_l(\mathbf{k})a^{\ell_2}_l(\mathbf{k})}{\mathrm{i}\omega_n - E_l(\mathbf{k})}\sum_{m}\frac{a^{\ell_1*}_m(\mathbf{k}+\mathbf{q})a^{\ell_3}_m(\mathbf{k}+\mathbf{q})}{\mathrm{i}\omega_n+\mathrm{i}\nu_n - E_m(\mathbf{k}+\mathbf{q})} \\ &= -\frac{1}{\beta}\sum_{\mathbf{k},\omega_n}\sum_{l,m} a^{\ell_4*}_l(\mathbf{k})a^{\ell_2}_l(\mathbf{k})a^{\ell_1*}_m(\mathbf{k}+\mathbf{q})a^{\ell_3}_m(\mathbf{k}+\mathbf{q}) \\ &\quad\times\frac{1}{\mathrm{i}\omega_n - E_l(\mathbf{k})}\frac{1}{\mathrm{i}\omega_n+\mathrm{i}\nu_n - E_m(\mathbf{k}+\mathbf{q})}. \end{aligned} \tag{3.22}$$

In there we have to evaluate the summation over Matsubara frequencies. By using residue theorem there is

$$\begin{aligned} &\frac{1}{\beta}\sum_{\omega_n}\frac{1}{\mathrm{i}\omega_n - E_l(\mathbf{k})}\frac{1}{\mathrm{i}\omega_n+\mathrm{i}\nu_n - E_m(\mathbf{k}+\mathbf{q})} \qquad (3.23)\\ =\ &\frac{1}{\beta}\sum_{\omega_n}\frac{1}{\mathrm{i}\nu_n - E_m(\mathbf{k}+\mathbf{q}) + E_l(\mathbf{k})}\left[\frac{1}{\mathrm{i}\omega_n - E_l(\mathbf{k})} - \frac{1}{\mathrm{i}\omega_n+\mathrm{i}\nu_n - E_m(\mathbf{k}+\mathbf{q})}\right] \\ &\big(\text{assume}\quad z_1 = E_l(k),\ z_2 = -\mathrm{i}\nu_n + E_m(\mathbf{k}+\mathbf{q})\big) \\ =\ &\frac{1}{\beta}\left[\frac{1}{z_1+\mathrm{i}\nu_n - E_m(\mathbf{k}+\mathbf{q})}\sum_{\omega_n}\frac{1}{\mathrm{i}\omega_n - z_1} + \frac{1}{z_2 - E_l(\mathbf{k})}\sum_{\omega_n}\frac{1}{\mathrm{i}\omega_n - z_2}\right] \\ =\ &-\frac{1}{\beta}\left[\lim_{z\to E_l(\mathbf{k})}\frac{1}{z+\mathrm{i}\nu_n - E_m(\mathbf{k}+\mathbf{q})}\frac{-\beta}{1+e^{\beta z}} + \lim_{z\to -\mathrm{i}\nu_n + E_m(\mathbf{k}+\mathbf{q})}\frac{1}{z - E_l(\mathbf{k})}\frac{-\beta}{1+e^{\beta z}}\right] \\ =\ &\frac{n_{\mathrm{F}}\left(E_l(\mathbf{k})\right) - n_{\mathrm{F}}\left(E_m(\mathbf{k}+\mathbf{q})\right)}{E_l(\mathbf{k}) - E_m(\mathbf{k}+\mathbf{q}) + \mathrm{i}\nu_n}, \qquad (3.24)\end{aligned}$$

in which the definition of the Fermi function is used in the last step. Thus, the non-interacting paramagnetic susceptibility Eq. 3.22 can be rewritten via the Eq. 3.24:

$$\begin{aligned}\chi^{\ell_4\ell_2}_{\ell_1\ell_3}(\mathbf{q},\mathrm{i}\nu_n) &= -\sum_{\mathbf{k},l,m} a^{\ell_4*}_l(\mathbf{k})a^{\ell_2}_l(\mathbf{k})a^{\ell_1*}_m(\mathbf{k}+\mathbf{q})a^{\ell_3}_m(\mathbf{k}+\mathbf{q}) \\ &\quad\times\frac{n_{\mathrm{F}}\left(E_l(\mathbf{k})\right) - n_{\mathrm{F}}\left(E_m(\mathbf{k}+\mathbf{q})\right)}{E_l(\mathbf{k}) - E_m(\mathbf{k}+\mathbf{q}) + \mathrm{i}\nu_n}. \end{aligned} \tag{3.25}$$

This form of paramagnetic susceptibility is a tensor of four orbital indices, momentum transfer $\mathbf{q}$ and the bosonic Matsubara frequency ν_n, which describes bosonic excitations and are associated with transitions of energy-state and momentum-state in the electronic structure, where the continuation to real-frequency axis is performed

by the replacement of $i\nu_n \to \nu + i\eta$, a real frequency plus a small imaginary frequency, with the limit of $\eta \to 0$. Clearly, for the computation of the non-interacting paramagnetic susceptibility the diagonalization of the kinetic part of the Hamiltonian is necessary.

3.3 Derivation for the RPA susceptibility

Then for beyond the non-interacting susceptibility susceptibility we will discuss the higher order terms. By using the final expression of Green's function in terms of connected diagrams (Eq. 3.26),

$$\begin{aligned} G(\lambda, t-t') &= -\mathrm{i}\,\langle\phi_0|Tc_\lambda(t)c_\lambda^\dagger(t')S(\infty,-\infty)|\phi_0\rangle_{\mathrm{con}} \\ &= -\mathrm{i}\sum_{n=0}^{\infty}\frac{(\mathrm{i})^n}{n!}\int_{-\infty}^{\infty}\mathrm{d}t_1\cdots\mathrm{d}t_n \\ &\quad\times\langle\phi_0|Tc_\lambda(t)c_\lambda^\dagger(t')V(t_1)\cdots V(t_n)|\phi_0\rangle_{\mathrm{con}}\,, \end{aligned} \tag{3.26}$$

we can write the full susceptibility, which is analogy to non-interacting paramagnetic susceptibility, up to infinite order:

$$\begin{aligned} \chi_{\ell_1\ell_3}^{\ell_4\ell_2}(\mathbf{q},\mathrm{i}\nu_n) &= A\int_0^\beta d\tau e^{-\mathrm{i}\nu_n\tau}\sum_{\mathbf{k}\mathbf{k}'}\sum_{\alpha\beta\delta\epsilon}\sum_{n=0}^{\infty}\frac{(-1)^n}{n!}\times \\ &\quad\left\langle T_\tau c_{\ell_4\alpha}^\dagger(\mathbf{k},\tau)c_{\ell_1\beta}^\dagger(\mathbf{k}',0)c_{\ell_3\delta}(\mathbf{k}'-\mathbf{q},0)c_{\ell_2\epsilon}(\mathbf{k}+\mathbf{q},\tau)S^n\right\rangle_{\mathrm{con}} \end{aligned} \tag{3.27}$$

where α, β, δ, and ϵ denote the spin quantum numbers, of which restrictions have to be adapted to the charge and spin channel with prefactor A respectively. From Eq. 3.7 we know the prefactor A=1/2 to the charge channel terms with α=ϵ, β=δ. And to the spin channel, the terms α=δ, β=ϵ, $\alpha\neq\beta$ contribute with prefactor A=1/3, terms α=β=δ=ϵ contribute with prefactor A=1/6, and terms α=ϵ, β=δ, $\alpha\neq\beta$ contribute with prefactor A=-1/6 depending on Eq. 3.14.

Due to the spin indices α, β, δ, and ϵ give a prefactor for the contribution of each diagram to charge and spin susceptibility. Thus, both diagrams contribute to the charge susceptibility with a prefactor of A=1/2. From the expansion Eq. 3.27 with the sign the first order contribution in the intra-orbital Coulomb repulsion to the charge susceptibility is

$$-\sum_u \chi_{\ell_1\ell_3}^{uu}(\mathbf{q})U\chi_{uu}^{\ell_4\ell_2}(\mathbf{q}). \tag{3.28}$$

Similarly, the first order contribution in the intra-orbital Coulomb repulsion to the spin susceptibility is

$$+\sum_{u}\chi^{uu}_{\ell_1\ell_3}(\mathbf{q})U\chi^{\ell_4\ell_2}_{uu}(\mathbf{q}). \tag{3.29}$$

Then we will give a simple case to write down the random phase approximation for the single-orbital Hubbard model. In this case, the tensor $\chi^{\ell_4\ell_2}_{\ell_1\ell_3}$ becomes a scalar. To generate higher order diagrams only needs us to insert additional interaction vertices into the bubble and ladder topology diagrams. Because Green's functions that mix spin are forbidden by the kinetic Hamiltonian, a mixture of both is not allowed. Therefore, the charge and spin susceptibilities of the single-orbital Hubbard model are

$$\chi_c = \chi_0 - \chi_0 U\chi_0 + \chi_0 U\chi_0 U\chi_0 - \ldots = \chi_0 - \chi_0 U\chi_c, \tag{3.30}$$
$$\chi_s = \chi_0 + \chi_0 U\chi_0 + \chi_0 U\chi_0 U\chi_0 + \ldots = \chi_0 + \chi_0 U\chi_s, \tag{3.31}$$

which only differ by a minus sign. Here, χ_c denotes the charge susceptibility, χ_s denotes the spin susceptibility, and χ_0 is the susceptibility susceptibility. Then Eqs.3.30 and 3.31 can be solved for the susceptibilities at infinite expansion order:

$$\chi_c = \frac{\chi_0}{1+U\chi_0}, \tag{3.32}$$
$$\chi_s = \frac{\chi_0}{1-U\chi_0}. \tag{3.33}$$

In analogy to the scalar equations of the single-orbital case (Eqs.3.32 and 3.33), for the multi-orbital case the tensor equations of susceptibilities are written as

$$\begin{aligned}(\chi_c)^{\ell_4\ell_2}_{\ell_1\ell_3} &= (\chi_0)^{\ell_4\ell_2}_{\ell_1\ell_3} - \sum_{abcd}(\chi_0)^{ab}_{\ell_1\ell_3}(U_c)^{cd}_{ab}(\chi_0)^{\ell_4\ell_2}_{cd} + \ldots \\ &= (\chi_0)^{\ell_4\ell_2}_{\ell_1\ell_3} - \sum_{abcd}(\chi_0)^{ab}_{\ell_1\ell_3}(U_c)^{cd}_{ab}(\chi_c)^{\ell_4\ell_2}_{cd}, \qquad (3.34)\\ (\chi_s)^{\ell_4\ell_2}_{\ell_1\ell_3} &= (\chi_0)^{\ell_4\ell_2}_{\ell_1\ell_3} + \sum_{abcd}(\chi_0)^{ab}_{\ell_1\ell_3}(U_s)^{cd}_{ab}(\chi_0)^{\ell_4\ell_2}_{cd} + \ldots \\ &= (\chi_0)^{\ell_4\ell_2}_{\ell_1\ell_3} + \sum_{abcd}(\chi_0)^{ab}_{\ell_1\ell_3}(U_s)^{cd}_{ab}(\chi_s)^{\ell_4\ell_2}_{cd}. \qquad (3.35)\end{aligned}$$

Again, similar as the single-orbital case, by inverting Eqs.3.34 and 3.35 in orbital space we can obtain the the charge and spin susceptibilities at infinite expansion

order:

$$\left[(\chi_c^{\mathrm{RPA}})_{\ell_1\ell_3}^{\ell_4\ell_2}\right]^{-1} = \left[(\chi_0)_{\ell_1\ell_3}^{\ell_4\ell_2}\right]^{-1} + (U_c)_{\ell_1\ell_3}^{\ell_4\ell_2}, \tag{3.36}$$

$$\left[(\chi_s^{\mathrm{RPA}})_{\ell_1\ell_3}^{\ell_4\ell_2}\right]^{-1} = \left[(\chi_0)_{\ell_1\ell_3}^{\ell_4\ell_2}\right]^{-1} - (U_s)_{\ell_1\ell_3}^{\ell_4\ell_2}. \tag{3.37}$$

Since the interaction tensor is simply a collection of constant numbers, the charge and spin susceptibilities up to infinite expansion order can be obtained by calculating and inverting non-interacting multi-orbital susceptibility in orbital space using the random phase approximation with the low cost, which actually is an important advantage of computational efficiency for the RPA method.

3.4 Derivation for the two-electron pairing vertex

To calculate the two-electron pairing vertex is the main goal of this chapter. With pairing vertex we can clearly understand the characteristics of the superconducting pairing symmetry in momentum and orbital space. The perturbation expansion of the particle-particle interaction can be derived from the perturbation expansion for the susceptibility (Eq. 3.27) and be written as

$$V_{\ell_1\ell_3}^{\ell_4\ell_2}(\mathbf{k},\mathbf{k}',\mathrm{i}\nu_n) = \int_0^\beta \mathrm{d}\tau e^{-\mathrm{i}\nu_n\tau} \sum_{\mathbf{k}\mathbf{k}'}\sum_{\varrho}\sum_{n=0}^{\infty}\frac{(-1)^n}{n!}\times \left\langle T_\tau c_{\ell_3\bar{\varrho}}^\dagger(-\mathbf{k},0)c_{\ell_4\varrho}^\dagger(\mathbf{k},0)c_{\ell_2\varrho}(\mathbf{k}',\tau)c_{\ell_1\bar{\varrho}}(-\mathbf{k}',\tau)S^n\right\rangle_{\mathrm{con}}. \tag{3.38}$$

Because we focus on spin-singlet superconductivity, spins with opposite directions at the external legs have to be fixed. For the two-particle vertex $\Gamma_{\ell_1\ell_3}^{\ell_4\ell_2}$, we have to cut off all external legs of $V_{\ell_1\ell_3}^{\ell_4\ell_2}$ to generate $\Gamma_{\ell_1\ell_3}^{\ell_4\ell_2}$ that can be written by the charge and spin susceptibilities (Eqs.3.36 and 3.37) as

$$\Gamma_{\ell_1\ell_3}^{\ell_4\ell_2}(\mathbf{k},\mathbf{k}') = \left[\frac{3}{2}U_s\chi_s^{\mathrm{RPA}}(\mathbf{k}-\mathbf{k}')U_s + \frac{1}{2}U_s - \frac{1}{2}U_c\chi_c^{\mathrm{RPA}}(\mathbf{k}-\mathbf{k}')U_c + \frac{1}{2}U_c\right]_{\ell_1\ell_3}^{\ell_4\ell_2}. \tag{3.39}$$

The two-particle vertex $\Gamma_{\ell_1\ell_3}^{\ell_4\ell_2}$ in Eq. 3.39 contains information about electron-pairing mediated by the charge and spin fluctuation processes included in the RPA diagram expansion, which, however, is still written in orbital space. For obtaining he symmetry of the superconducting pairing for electrons living on the Fermi surface, there is an idea that when all frequencies are set to zero the singlet-symmetrized two-particle vertex $\Gamma_{\ell_1\ell_3}^{\ell_4\ell_2}$ transforms into band space. Thus, by using the eigenvectors of

H_0, this vertex in orbital space is projected onto band space

$$\Gamma_{ij}(\mathbf{k},\mathbf{k}') = \sum_{\ell_1,\ell_2,\ell_3,\ell_4} a_i^{\ell_3 *}(-\mathbf{k}) a_i^{\ell_1 *}(\mathbf{k}) \mathrm{Re}\left[\Gamma^{\ell_4\ell_2}_{\ell_1\ell_3}(\mathbf{k},\mathbf{k}')\right] a_j^{\ell_4}(\mathbf{k}') a_j^{\ell_2}(-\mathbf{k}'), \tag{3.40}$$

where the band index i is associated with momentum $\mathbf{k}$ and the band index j is associated with momentum $\mathbf{k}'$. These combinations can be calculated easily from the kinetic Hamiltonian. In Eq. 3.40, the two-particle vertex is accessible to calculations where Fermi surface can be discretized by the inserted discretized momenta $\mathbf{k}$ and $\mathbf{k}'$, and $\Gamma_{ij}(\mathbf{k},\mathbf{k}')$ can be determined by a set of discretized momenta and diagonalized in the combined indices $(i,\mathbf{k})$ and $(j,\mathbf{k}')$. These eigenfunctions are possible symmetries of the superconducting gap on the Fermi surface.

Considering an eigenvalue problem for the two-particle vertex, in which there is the pairing amplitude λ and a dimensionless symmetry function $g(\mathbf{k})$, the gap equation, which is solved for the pairing eigenvalue λ_i and the gap function $g_i(\mathbf{k})$, can be written as

$$\lambda_i g_i(\mathbf{k}) = -\sum_{j,\mathbf{k}'} \Gamma_{ij}(\mathbf{k},\mathbf{k}') g_j(\mathbf{k}'), \tag{3.41}$$

$$\lambda_i g_i(\mathbf{k}) = -\sum_{j,\mathbf{k}'} \frac{\Gamma_{ij}(\mathbf{k},\mathbf{k}')}{\hbar|\mathbf{v}(\mathbf{k}')|} g_j(\mathbf{k}'), \tag{3.42}$$

$$\lambda_i g_i(\mathbf{k}) = -\sum_{j} \oint_{C_j} \frac{\mathrm{d}k'_{||}}{2\pi} \frac{1}{4\pi v_\mathrm{F}(\mathbf{k}')} \left[\Gamma_{ij}(\mathbf{k},\mathbf{k}') + \Gamma_{ij}(\mathbf{k},-\mathbf{k}')\right] g_j(\mathbf{k}'), \tag{3.43}$$

where the definition of Fermi velocity is

$$\delta\left(E_{\mathbf{k}_i} - E_\mathrm{F}\right) = \frac{\delta\left(\mathbf{k}_i - \mathbf{k}_\mathrm{F}\right)}{|\nabla_{\mathbf{k}_i} E(\mathbf{k})|_{\mathbf{k}=\mathbf{k}_i}} = \frac{\delta\left(\mathbf{k}_i - \mathbf{k}_\mathrm{F}\right)}{\hbar|\mathbf{v}(\mathbf{k}_i)|}. \tag{3.44}$$

These equations (Eq. 3.41-3.43) allows us to extract a symmetry function, which characterizes the superconducting state in momentum space, and a dimensionless measure for the pairing strength.

Chapter 4

Dynamical mean-field theory

Dynamical mean-field theory (DMFT) is a standard method and theoretical tool employed extensively for strongly correlated systems [57], where one-electron description breaks down due to that the strength of the electron-electron interactions is comparable to or larger than the kinetic energy. Thus DMFT includes d and/or f electrons to show rich quantum phenomena. The full account of local correlations responding for local moment is taken by DMFT which is good to be used to address long-range ordering.

For formalizing DMFT, it is necessary to apply some physical models such as Hubbard models. Generally DMFT is combined with density functional theory (DFT) based on *abinitio*, namely first-principles, calculations, which is called DMFT+DFT. This composite framework, DMFT+DFT, is widely used for various types of materials, such as cuprates [58], iron-based superconductors [59, 60], f-electron system materials [61, 62], *etc.*

Then in DMFT calculation, the basic process is that an original lattice model is mapped onto an effective Anderson impurity problem to subject to a self-consistency condition. The impurity is used to offer the intuitive picture of the local dynamics for quantum many-body system. Theoretically, this mapping is exact for models of correlated electrons in the limit of large lattice coordination or infinite spatial dimensions [57], which is an extension for the mean-field construction from classical statistical mechanics to quantum problems.

4.1 Local impurity self-consistent approximation

In DMFT calculation, as mentioned before, an essential idea of approximation is to replace a lattice model by a single-site quantum impurity problem embedded

in an effective medium determined self-consistently. The self-consistency condition captures the translation invariance and coherence effects of the lattice [57]. This approach is defined as the local impurity self-consistent approximation (LISA) .

LISA is a natural generalization of the Weiss mean-field theory familiar from classical statistical mechanics to quantum many-body problem. In classical statistical mechanics, exact dynamical mean-field theory relies on the case of large spatial dimensions or more appropriately large lattice coordination limit. In a broader context, on the limit of large dimensions, this method was generalized on strongly correlated fermion models, which leads to the LISA method [63]. In LISA, for lattice models of correlated fermions, there is a nontrivial limit of infinite spatial dimensions that can be derive from the scaling of the hopping amplitude. And by perturbation theory the potential usefulness of the limit is demonstrated from their local nature. Moreover, it is found that LISA equations can be described in the context of the periodic Anderson model [64]. Then there is a significant progress of main content of the LISA approach that the functional equations can be interpreted as an Anderson impurity model subject to a self-consistent bath [65–68]. Thus the treated Anderson impurity mode can be a reliable technique to study correlated electrons in large dimensions.

Then for solving these dynamical mean-field equations in Anderson impurity mode, there are a lot of numerical methods were implemented. The quantum Monte Carlo (QMC) algorithm [69] is a not only earlier but also important method that is applied to this problem [68, 70, 71]. However there is no single technique that is outstandingly more appropriate than others. Then the understanding of the many-body phenomena is improved by the combination of these various numerical methods together with analytical approximations. Similarly, a lot of software packages are developed to perform DMFT+DFT calculations. Toolbox for Research on Interacting Quantum Systems (TRIQS) project is a package that includes QMC impurity solver and an interface of DFT codes [72–74]. The ALPS project performs DMFT by simple Hubbard models with implementations of several continuous-time QMC (CT-QMC) impurity solvers [75–78]. w2dynamics implements a developed QMC algorithm and provides DFT+DMFT by Python program [79]. DMFTwDFT supports various DFT codes and the CT-QMC impurity solver in their featured interface [80]. DFT+embedded DMFT Functional (eDMFT) is constructed as a full set of DFT+DMFT functionalities software [81].

4.2 Dynamical mean-field equations

Mean-field theory aims to replace the lattice problem with many degrees of freedom by a single-site effective problem with less degrees of freedom using an approx-

imation. It is feasible due to the underlying physical idea that the dynamics at a certain site, which will be discussed, can be considered as the interaction of the degrees of freedom at this site with an external bath that is created by all other degrees of freedom on other sites.

There is a simplest picture, Ising model with ferromagnetic couplings $J_{ij} > 0$ between nearest-neighbor sites of a lattice with coordination z, to describe this idea:

$$H = -\sum_{\langle ij \rangle} J_{ij} S_i S_j - h \sum_i S_i. \tag{4.1}$$

For Weiss mean-field theory views of each given site, labeled o, governed by an effective Hamiltonian is:

$$H_{\text{eff}} = -h_{\text{eff}} S_o, \tag{4.2}$$

where the effective field h_{eff} contains all interactions with the other degrees of freedom:

$$h_{\text{eff}} = h + \sum_i J_{oi} m_i = h + zJm, \tag{4.3}$$

where $m_i = \langle S_i \rangle$ is the magnetization at site i. $J_{ij} = J$ for nearest-neighbor sites $m_i = m$ depends on an assumption of translation invariance. Here h_{eff} is already related to a local quantity, which it can be calculated from the single-site effective model H_{eff} in turn. Combining Eq. 4.3 with $m = \tanh(\beta h_{\text{eff}})$, it is the well-known mean-field equation for the magnetization:

$$m = \tanh(\beta h + z\beta J m). \tag{4.4}$$

Generally these mean-field equations are an approximation of the true solution of the Ising model. In the limitation of the coordination of large lattice these equations become exact, which is natural because when the number of the neighbors of given site is growth these neighbors can be treated globally as an external bath and the spatial fluctuations of the local field become negligible. Namely in Eq. 4.3 it is clear that the coupling J must be scaled by $J = J^*/z$ following a sensible limit $z \to \infty$.

Directly extending these ideas into quantum many-body systems, the Hubbard model will be:

$$H = -\sum_{\langle ij \rangle, \sigma} t_{ij} (c^+_{i\sigma} c_{j\sigma} + c^+_{j\sigma} c_{i\sigma}) + U \sum_i n_{i\uparrow} n_{i\downarrow}. \tag{4.5}$$

For simplicity, it is assumed that no symmetry breaking occurs, which means that it is dealing with the translation-invariant paramagnetic phase. Combining the mean-field description with this Hamiltonian Eq. 4.5, we have a single-site effective dynamics described in terms of an imaginary-time action for the fermionic degrees of freedom $(c_{o\sigma},\, c^{+}_{o\sigma})$:

$$S_{\text{eff}} = -\int_0^\beta \mathrm{d}\tau \int_0^\beta \mathrm{d}\tau' \sum_\sigma c^{+}_{o\sigma}(\tau)\mathcal{G}_0^{-1}(\tau-\tau')c_{o\sigma}(\tau') + U\int_0^\beta \mathrm{d}\tau n_{o\uparrow}(\tau)n_{o\downarrow}(\tau), \quad (4.6)$$

where $\mathcal{G}_0(\tau-\tau')$ plays the role of the Weiss effective field above, of which physical content is effective amplitude for a fermion created on the isolated site at time τ (coming from the external bath) and destroyed at time τ' (backing to the bath). Comparing with classical case this Weiss function is generalized to be a function of time instead of a single number, in which it is necessary to take into account local quantum fluctuations. In this case, the spatial fluctuations of the mean-field theory are frozen but it takes full account of local temporal fluctuations, which is the origin of named 'dynamical'. It should be careful that $\mathcal{G}_0$ is a bare Green's function for the impurity local effective action S_{eff} and does not be the non-interacting local Green's function of the original lattice model.

A closed set of mean-field equations procured by Eq. 4.6 with the expression relating $\mathcal{G}_0$ to local quantities computed from S_{eff} is in complete analogy with Eq. 4.3. Thus, the self-consistency condition is

$$\mathcal{G}_0(\mathrm{i}\omega_n)^{-1} = \mathrm{i}\omega_n + \mu + G(\mathrm{i}\omega_n)^{-1} - R[G(\mathrm{i}\omega_n)], \quad (4.7)$$

where $G(i\omega_n)$ is the on-site interacting Green's function calculated from the impurity local effective action S_{eff}:

$$G(\tau-\tau') \equiv -\langle Tc(\tau)c^{+}(\tau)\rangle_{S_{\text{eff}}}, \quad (4.8)$$

$$G(\mathrm{i}\omega_n) = \int_0^\beta \mathrm{d}\tau G(\tau)e^{\mathrm{i}\omega_n\tau}, \qquad \omega_n \equiv \frac{(2n+1)\pi}{\beta}, \quad (4.9)$$

and $R(G)$ the reciprocal function of the Hilbert transform of the density of states corresponding to the near lattice. Then the definition of Hilbert transform $\tilde{D}(\zeta)$ and its reciprocal function R are:

$$\tilde{D} \equiv \int_{-\infty}^{+\infty} \mathrm{d}\epsilon \frac{D(\epsilon)}{\zeta-\epsilon}, \qquad R\left[\tilde{D}(\zeta)\right] = \zeta, \quad (4.10)$$

where the non-interacting density of states $D(\epsilon)$ is:

$$D(\epsilon) = \sum_{\mathbf{k}} \delta(\epsilon - \epsilon_{\mathbf{k}}), \qquad \epsilon_{\mathbf{k}} \equiv \sum_{ij} t_{ij} e^{\mathrm{i}\mathbf{k}\cdot(\mathbf{R}_i - \mathbf{R}_j)}. \tag{4.11}$$

In principle G is computable as a functional of $\mathcal{G}_0$ by using Eq. 4.6, Eq. 4.7, and Eq. 4.8 form a closed system of functional equations for the impurity local effective action S_{eff}, the on-site Green's function G, and the Weiss function $\mathcal{G}_0$. These equations are the basic equations of the LISA method, which, especially for S_{eff}, are contributed by a lot of researchers.

Instructively, there are two simple limits to check these equations:

(1) the non-interacting limit U=0:

By solving Eq. 4.6 yields $G(\mathrm{i}\omega_n) = \mathcal{G}_0(\mathrm{i}\omega_n)$ and Eq. 4.7, there is

$$G(\mathrm{i}\omega_n) = D(\mathrm{i}\omega_n + \mu), \tag{4.12}$$

which is reduced to to the free on-site Green's function.

(2) the atomic limit $t_{ij} = 0$:

In this limit, there is only collection of disconnected sites and $D(\epsilon)$ becomes a δ function with $\tilde{D}(\zeta) = 1/\zeta$. $\mathcal{G}_0(\mathrm{i}\omega_n)^{-1} = \mathrm{i}\omega_n + \mu$ is implied from Eq. 4.7. The effective action S_{eff} becomes essentially local in time and describes a four-state Hamiltonian yielding

$$G(\mathrm{i}\omega_n)_{\text{at}} = \frac{1 - n/2}{\mathrm{i}\omega_n + \mu} + \frac{n}{2(\mathrm{i}\omega_n + \mu - U)}, \tag{4.13}$$

with

$$\frac{n}{2} = \frac{e^{\beta\mu} + e^{\beta(2\mu - U)}}{1 + 2e^{\beta\mu} + e^{\beta(2\mu - U)}}. \tag{4.14}$$

By solving above coupled equations yields local quantities, we also have to reconstruct all the $\mathbf{k}$-dependent correlation functions of the original lattice Hubbard model. Thus, the Fourier transform of the one particle Green's function

$$G_{ij}(\tau - \tau') \equiv -\left\langle T c_{i,\sigma}(\tau) c^{+}_{j,\sigma}(\tau') \right\rangle \tag{4.15}$$

can be shown to read

$$G(\mathbf{k}, \mathrm{i}\omega_n) = \frac{1}{\mathrm{i}\omega_n + \mu - \epsilon_{\mathbf{k}} - \Sigma(\mathrm{i}\omega_n)}, \tag{4.16}$$

where the self-energy can be calculated from the solution of the effective on-site problem that

$$\Sigma(\mathrm{i}\omega_n) = \mathcal{G}_0(\mathrm{i}\omega_n)^{-1} - G^{-1}(\mathrm{i}\omega_n), \tag{4.17}$$

which is $\mathbf{k}$-independent in the approach of purely local in space: $\Sigma_{ij}(\mathrm{i}\omega_n) = \delta_{ij}\Sigma(\mathrm{i}\omega_n)$.

4.3 DCore

Several DMFT program packages are mentioned in section 4.1. In our study we use DCore which is an open-source program package that implements (DFT+)DMFT calculations for multi-orbital systems [82, 83].

The process of computation of DCore is exhibited in Fig. 4.1. Clearly the main

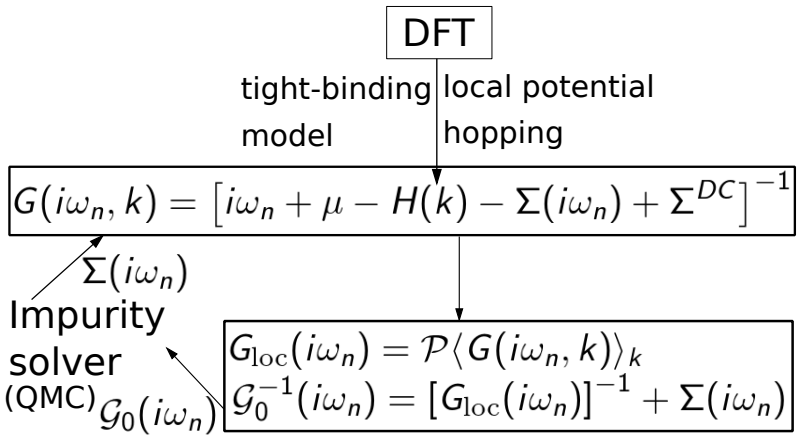

Figure 4.1: The main process of DMFT self-consistency cycle by DCore.

idea of DCore is to compute self-energy Σ by solving an impurity problem depended on following equations:

$$G(\mathrm{i}\omega_n, k) = \left[\mathrm{i}\omega_n + \mu - H(k) - \Sigma(\mathrm{i}\omega_n) + \Sigma^{\mathrm{DC}}\right]^{-1}, \tag{4.18}$$

$$G_{\mathrm{loc}}(\mathrm{i}\omega_n, s) = \mathcal{P}_s\langle G(k)\rangle_k, \tag{4.19}$$

$$\mathcal{G}_0^{-1}(\mathrm{i}\omega_n, s) = [G_{\mathrm{loc}}(\mathrm{i}\omega_n, s)]^{-1} + \Sigma(\mathrm{i}\omega_n, s), \tag{4.20}$$

$$\Sigma^{\mathrm{imp}}_{\varrho\varrho'}(\mathrm{i}\omega_n, s) \leftarrow \mathcal{G}_0(\mathrm{i}\omega_n, s), \tag{4.21}$$

$$\Sigma_{\varrho\varrho'}(\mathrm{i}\omega_n, s) \leftarrow \Sigma^{\mathrm{imp}}_{\varrho\varrho'}(\mathrm{i}\omega_n, s) \tag{4.22}$$

Here, $\omega_n \equiv (2n+1)\pi T$ is a fermionic Matsubara frequency at temperature T, $\langle\cdots\rangle_k$ denotes an average over the momentum space, s indexes correlated shells, $\mathcal{P}$ is the projector to the s-th correlated shell, and ϱ denotes spin. Σ^{DC} is double-counting corrections as

$$\Sigma^{\mathrm{DC}}_{\alpha\beta}(s) = \sum_{\gamma\delta} \left[U_{\alpha\gamma\beta\delta}(s) - U_{\alpha\gamma\delta\beta}(s)\right] \langle c^\dagger_{s\gamma} c_{s\delta}\rangle_0, \tag{4.23}$$

where $U_{\alpha\gamma\beta\delta}(s)$ denotes a spin-full four-rank Coulomb tensor with index spin orbitals α, γ, β, δ, and $\langle\cdots\rangle_0$ indicates the expectation value at the initial (Kohn-Sham) state with k-summation included.

Creation and annihilation operators $c^\dagger$ and c are defined as

$$c^\dagger_{\mathbf{k}s\alpha} = \frac{1}{\sqrt{N}} \sum_{\mathbf{R}} e^{\mathrm{i}\mathbf{k}\cdot\mathbf{R}} c^\dagger_{\mathbf{R}s\alpha}, \tag{4.24}$$

$$c_{\mathbf{k}s\alpha} = \frac{1}{\sqrt{N}} \sum_{\mathbf{R}} e^{-\mathrm{i}\mathbf{k}\cdot\mathbf{R}} c_{\mathbf{R}s\alpha}. \tag{4.25}$$

where N denotes the number of $\mathbf{k}$ points, $\mathbf{k}$ is momentum index, and $\mathbf{R}$ is the coordinates of a unit cell.

Chapter 5

Titanium oxypnictide superconductors

About a decade ago, a new group of superconductors join in the whole superconductors family, which is titanium-based superconductors. Titanium-based superconductors are analogous to cuprates or iron-based superconductors because of two reasons. One is that Fe and Ti both of them are transition metal of which physical properties are mainly contributed by electrons in $3d$ orbitals. Another is the square lattice environment of Ti atoms is the analogy to cuprates or iron-based superconductors. Thus, it is expected that we can find some extraordinary behaviors or properties in titanium-based superconductors.

As mentioned in section 1.2, the first layered titanium oxypnictides $Na_2Ti_2As_2O$ and $Na_2Ti_2Sb_2O$ are found three decades ago [8]. Then the discoveries of superconductivity in $BaTi_2Pn_2O$ (Pn = pnictogen) with doping and pressure open a big gate of the group of titanium-based superconductors [11, 12, 18, 23–25]. Thus it becomes a hot topic to seek new high T_c titanium-based materials of which superconductivity favors the phase that spin-density wave (SDW) or charge-density wave (CDW) is suppressed. However, even if some new titanium-based superconductors are found nowadays, the question of tendency of T_c, namely superconducting mechanism of titanium materials, is still unsolved with a clear answer. In this chapter, by studying susceptibility, gap equation and other physical properties, we will give our own understanding of T_c and superconducting mechanism of titanium-based superconductor.

5.1 Methods

Shown in section 1.2, Fig. 1.4, the space group of $BaTi_2Pn_2O$ (Pn = pnictogen) is $P4/mmm$. In this study, the space group of $BaTi_2Pn_2O$ (Pn = pnictogen) will not be changed along doping or pressure increase. For investigating titanium oxypnictides on different doping or pressure level, we use experimental lattice parameters and smoothly interpolate the lattice parameters to sample the crystal structures of doping or pressure at regular intervals. Depending on the interpolated lattice parameters, we use density functional theory (DFT) by full-potential local-orbital (FPLO) code and the generalized gradient approximation (GGA) exchange-correlation functional to optimize positions of pnictogen atoms, which are the only free positions in this $P4/mmm$ crystal structures. For $BaTi_2Sb_2O$ case, it should be note that the deviation in the Ti−Sb distance and the Sb−Ti−Sb angle is only 0.2% between the experimental and relaxed structure. This gives us confidence that the relaxation is reliable also for the doping series for which no experimental Sb position is available, in contrast to the well-known difficulties of the DFT structure prediction for iron-based superconductors [84]. The alkali-doping x is modelled by using the virtual crystal approximation (VCA) for Ba using a nuclear charge between $Z = 55$ and 56.

For performing electronic structure FPLO within GGA is used to the exchange and correlation potentia, and then physical properties like density of states (DOS), band structure, Fermi surface, etc. are calculated. Next we make the tight-binding model for doped or pressured titanium oxypnictide via the projected Wannier Functions in FPLO, in which we obtain 26 band tight-binding model including five $3d$ orbital characters and one $4s$ orbital characters for two Ti atoms, five $5d$ for Ba, three $5p$ or $6p$ of two pnictogen atoms, and three $2p$ of O. Based on the 26 band tight-binding model, the non-interacting susceptibilities $\chi^{\ell_4\ell_2}_{\ell_1\ell_3}(\mathbf{q})$ can be calculated.

Then by applying random-phase approximation (RPA) and spin-fluctuation theory, the pairing instabilities are investigated by solving the gap equation on the Fermi surface, where interaction parameters, intraorbital Coulomb repulsion $U = 2$ eV, interorbital Coulomb repulsion $U' = 1$ eV, Hund's rule coupling $J = 0.5$ eV, and pair hopping $J' = 0.5$ eV, are applied to Ti $3d$ orbitals.

On the other hand, the environment of Ti atom should be noticed. The Ti atom is surrounded by 4 pnictogen atoms as the midpoint of a rectangle namely $x - y$ plane and 2 oxygen atoms that can be considered as top and bottom namely z axis. These 6 atoms make an TiO_2Pn_4 octahedron of which center is Ti atom. Due to this environment and depending on the crystal field theory, the orbital character of Ti should be organized in t_{2g} ($3d_{xy}$, $3d_{xz}$, $3d_{yz}$) and e_g ($3d_{z^2}$, $3d_{x^2-y^2}$) orbitals.

5.2 Titanium oxypnictide with alkali-doping

After the discoveries of superconductivity in $BaTi_2Sb_2O$ [14] and $BaTi_2Bi_2O$ [15], it is found that for titanium oxypnictides T_c can be increased via alkali-doping. T_c was risen to 5.5 K in $Ba_{1-x}Na_xTi_2Sb_2O$ [18,21], to 6.1 K in $Ba_{1-x}K_xTi_2Sb_2O$ [23], to 5.4 K in $Ba_{1-x}Rb_xTi_2Sb_2O$ [24], and to 4.4 K in $Ba_{1-x}Cs_xTi_2Sb_2O$ [25]. Superconductivity of alkali-doped titanium oxypnictide will be studied in this section.

Before the computation of DFT, by using the experimental data from Ref. [18,23, 24] we make the interpolation of lattice parameters of $Ba_{1-x}Na_xTi_2Sb_2O$, $Ba_{1-x}K_xTi_2Sb_2O$, and $Ba_{1-x}Rb_xTi_2Sb_2O$ that is shown in Fig. 5.1. This smooth interpolation

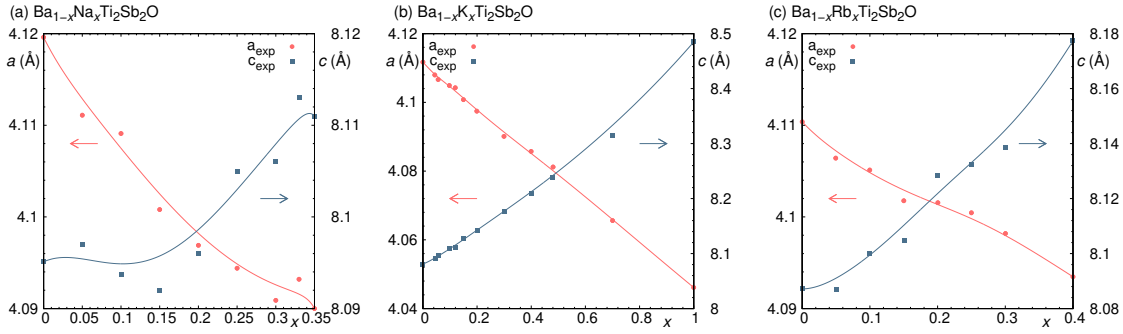

Figure 5.1: Interpolation of experimental lattice constants.

will help us to reduce errors rather that lose detial, for example modifying the small nonmonotonous behavior of $Ba_{1-x}Na_xTi_2Sb_2O$. Then we can use interpolating lat-

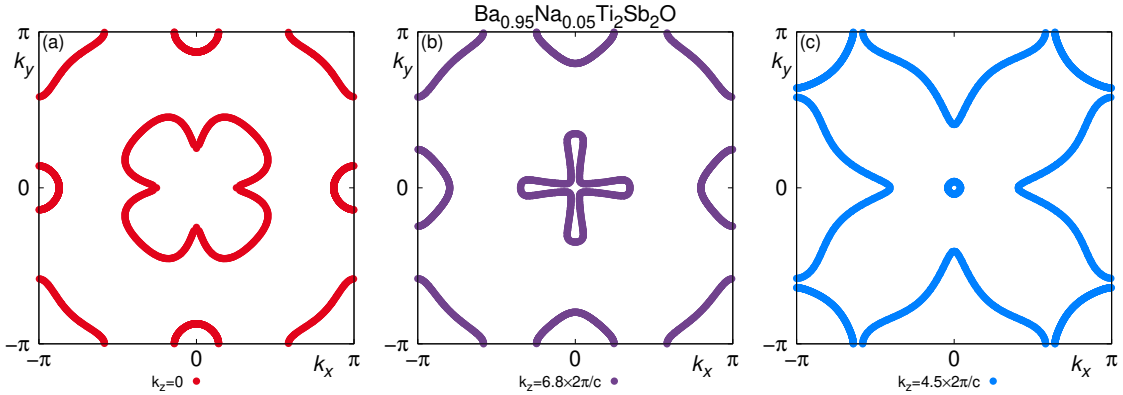

Figure 5.2: Fermi surface of $Ba_{0.95}Na_{0.05}Ti_2Sb_2O$ at $k_z = 0$, $k_z = 0.5\pi$ and $k_z = \pi$.

tice parameters on fixed interval to study the electronic structure of these titanium oxypnictides with alkali-doping by DFT calculation using FPLO with VCA.

5.2.1 Results from DFT calculation

In DFT calculation, inspecting band structure and Fermi surface is the most direct way to study the electronic structure of materials. Thus, firstly, we show some Fermi surface cuts of $Ba_{0.95}Na_{0.05}Ti_2Sb_2O$, on different k_z in Fig. 5.2, of which the 5% doping level and k_z value are decided by the photoemission intensity map experiment from Fig. 2 in Ref. [85] for comparison. Comparing these two figures, we can find that the typical crossing form Fermi surface around Γ point, shape changing of Fermi surface with variation of k_z around $X(Y)$ point and almost unchanged Fermi surface around M point are comparable with experimental results.

Then, by DFT calculation the band structure with the identified most relevant orbital characters on path Y-Γ-X-M-Γ-Z-R-A-Z-T and corresponding density of states of $BaTi_2Sb_2O$ are shown in Fig. 5.3, where Ti $3d$ and Sb $5p$ orbital characters are highlighted. It is shown that Ti $3d$ and Sb $5p$ orbitals are dominated on Fermi

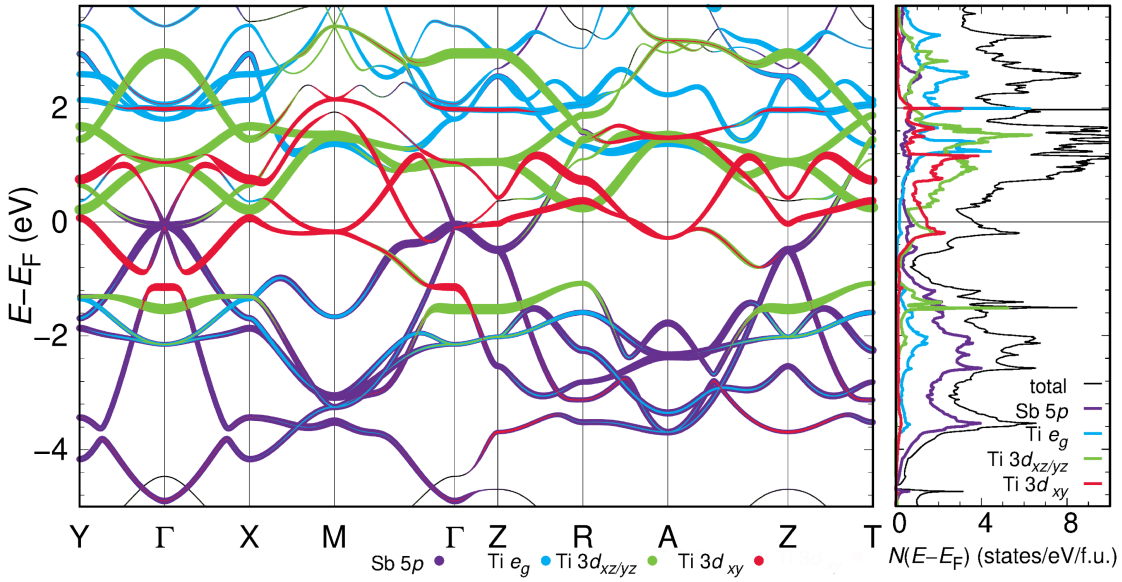

Figure 5.3: GGA band structure on path Y-Γ-X-M-Γ-Z-R-A-Z-T and DOS of $BaTi_2Sb_2O$, where $\mathbf{q} = (\pi, 0, 0)$ is labeled as X, $\mathbf{q} = (0, \pi, 0)$ as Y, $\mathbf{q} = (\pi, \pi, 0)$ as M, $\mathbf{q} = (0, 0, \pi)$ as Z, $\mathbf{q} = (0, \pi, \pi)$ as R, $\mathbf{q} = (\pi, \pi, \pi)$ as A and $\mathbf{q} = (\pi, 0, \pi)$ as T.

level, but there is quite strong hybridization by the contribution of many orbitals for the states close to the Fermi level. When we focus on Ti $3d$ orbitals further, the sequence of dominant orbitals is $3d_{xy}$ and $3d_{xz,yz}$ (t_{2g}) orbitals and there is almost no contribution from $3d_{z^2}$ and $3d_{x^2-y^2}$ (e_g) orbitals. In addition, density of states shows that $3d_{xy}$ orbital is absolutely dominating this Fermi level, which indicates that when we study physical properties we should first consider the influence of $3d_{xy}$ orbital. Because of this reason, the local coordinate system for Ti, which is used in Fig. 5.3 and following studies for visualizing Ti $3d_{xy}$ orbital handily and reasonably, is set as z axis points along the Ti−O bond and x and y axes point along the Ti−Sb bonds. This is the natural local system to choose within the TiO_2Sb_4 octahedron (mentioned in section 5.1 and Fig. 1.4) since it makes $3d_{xz}$ and $3d_{yz}$ degenerate.

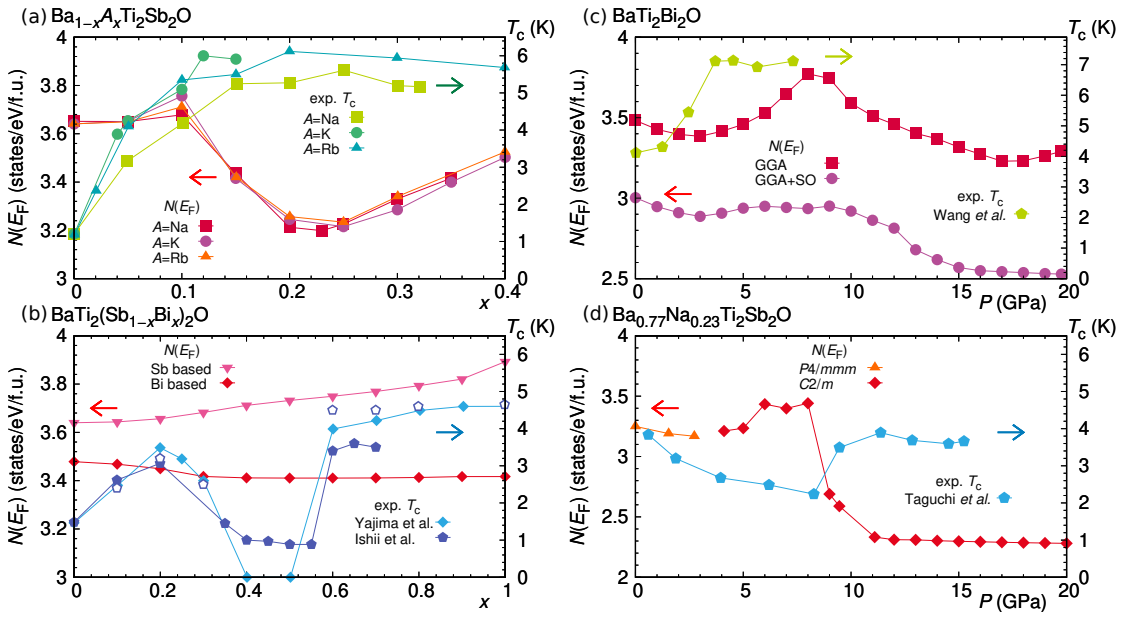

Figure 5.4: Density of states at the Fermi level $N(E_F)$ varying with doping level x compare with T_c for (a) $Ba_{1-x}A_xTi_2Sb_2O$ along alkali-doping, (b) $BaTi_2(Sb_{1-x}Bi_x)_2O$ along isovalent doping, (c) $BaTi_2Bi_2O$ along pressure, and (d) $Ba_{0.77}Na_{0.23}Ti_2Sb_2O$, data of T_c from Ref. [11–13, 18, 23, 24, 86].

On the other hand, we would like to consider the effect of hole doping by using Fig. 5.3. If we shift the Fermi level by using rigid bands approximation like Ref. [26, 27], the density of states on Fermi level $N(E_F)$ will be increased. Thus by using

McMillan formula

$$T_c = 1.336 T_D \exp\left(\frac{-1}{N(E_\mathrm{F})V}\right), \tag{5.1}$$

where Debye temperature T_D and electron-phonon coupling potential V are assumed as constant, we can explain the increasing T_c. However the tendency of $N(E_\mathrm{F})$ cannot compare with T_c for not only $Ba_{1-x}Na_xTi_2Sb_2O$ but also other titanium oxypnictides $BaTi_2Pn_2O$, which is shown in Fig. 5.4. It is clear that we cannot predict T_c by $N(E_\mathrm{F})$ using McMillan formula, which leads titanium oxypnictides $BaTi_2Pn_2O$ to be far from conventional superconductor. Thus, we have to consider to be beyond DFT for analyzing more and more physical properties.

Then for analysing physical properties further, we construct tight-binding models for $BaTi_2Sb_2O$ and the alkali-doping series by using projective Wannier functions in FPLO. The comparison between DFT and tight-binding models is shown in Fig. 5.5

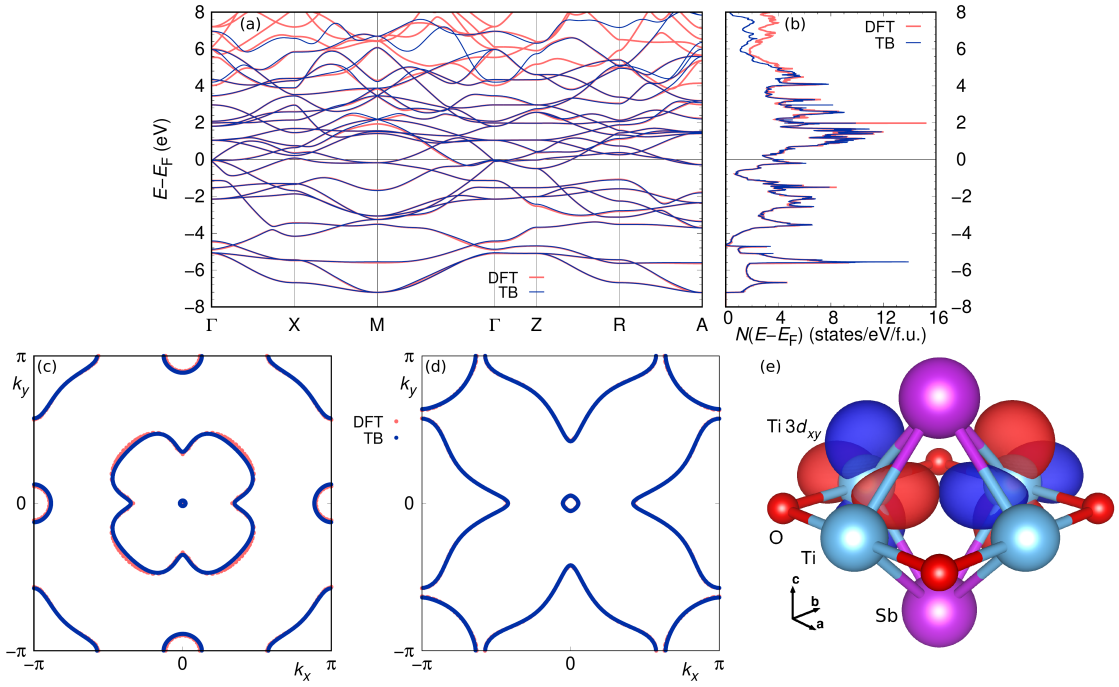

Figure 5.5: Comparison between the DFT and tight-binding models for (a) band structure, (b) DOS, (c) Fermi surface at $k_z = 0$, and (d) Fermi surface at $k_z = \pi$ of $BaTi_2Sb_2O$. And (e) there is the Ti $3d_{xy}$ Wannier functions within the TiO_2Sb_4 layer of $BaTi_2Sb_2O$.

(a) for band structure, (b) for DOS, and (c) and (d) for Fermi surface. Obviously these tight-binding models are good to fit with DFT result, which can be used to study physical properties of whole $Ba_{1-x}Na_xTi_2Sb_2O$ doping series. And Fig. 5.5 (e) shows the $3d_{xy}$ Wannier functions at both titanium sites, Ti site 1 (Ti1) and Ti site 2 (Ti2), based on the coordinate choice mentioned before.

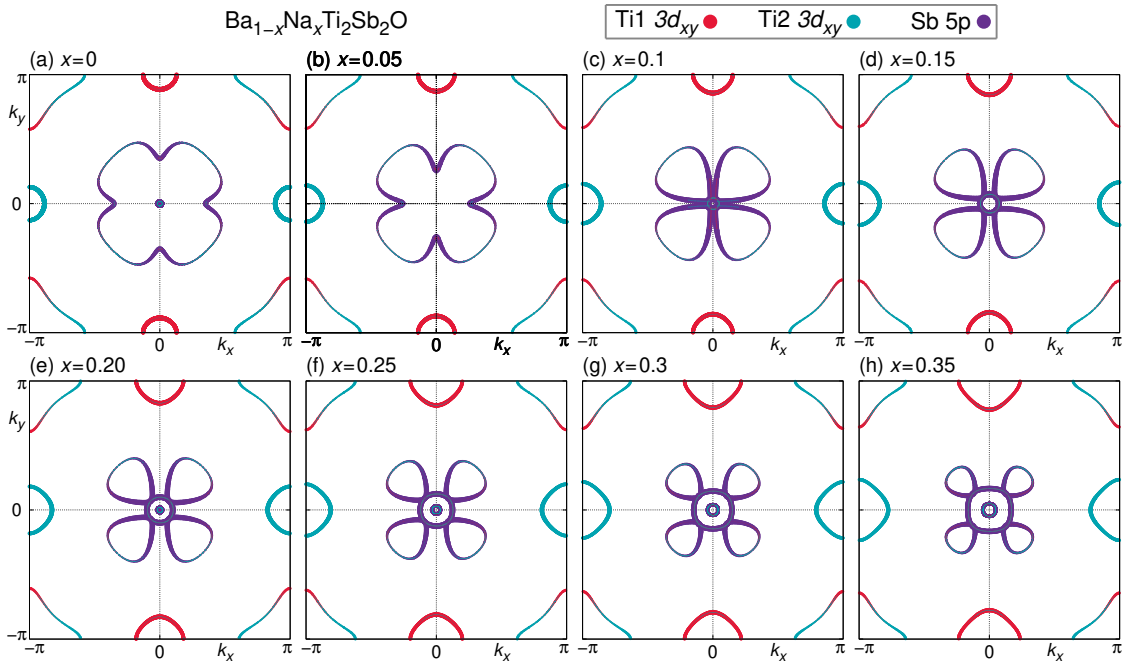

Figure 5.6: Fermi surface of $Ba_{1-x}Na_xTi_2Sb_2O$ at $k_z = 0$ as function of doping level x.

Next we will move to the main question of this section, *i.e.* the effect of alkali-doping. First we analyze the Fermi-surface evolution of $Ba_{1-x}Na_xTi_2Sb_2O$. As an example, the cut of Fiermi surface at $k_z = 0$ with increasing Na doping is exhibited in Fig. 5.6, where we only highlight the Ti $3d_{xy}$ and Sb $5p$ orbitals because relative contributions to the density of states at the Fermi-level $N(E_F)$ are 74%, 20%, 4% and 1% for Ti, Sb, Ba, and O, respectively. And $3d_{xy}$ and $5p$ orbitals mainly contribute to the whole density of states of Ti and Sb respectively. The comparison of weights of Ti $3d$ orbitals for Ti1 is shown in Fig. 5.7. The $3d_{xy}$ orbital clearly dominates, followed in importance by $3d_{yz}$ and $3d_{xz}$. The $3d_{z^2}$ character is very faint, and the $3d_{x^2-y^2}$ character is negligible. It is clear that the contribution of $3d_{xy}$ orbital is much larger than other orbitals, which will be proved again in the following study of susceptibility. For Sb $5p$, the situation of orbital weights on Fermi surface is

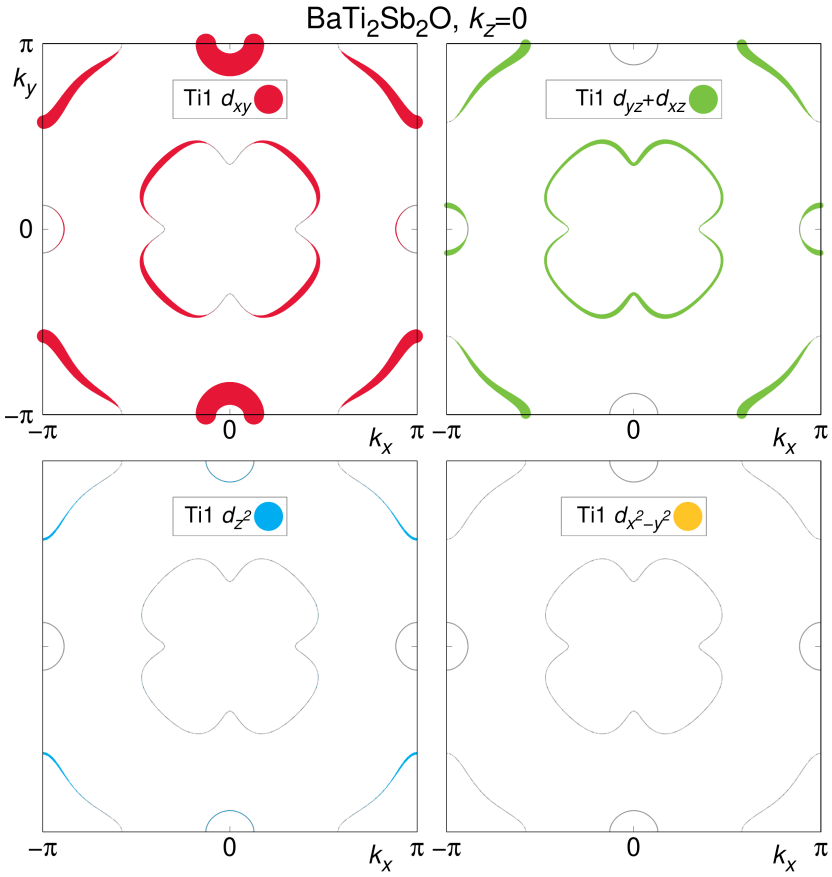

Figure 5.7: Ti1 $3d_{xy}$ orbital weights on Fermi surface of $BaTi_2Sb_2O$at $k_z = 0$. All weights are shown with the same scale. Weights of the Ti2 site are 90° rotated with respect to the first so that the sum has the C_4 symmetry of the space group.

same. That is the reason why we only consider these two orbitals in Fig. 5.6. The characteristics of Fermi surface are discussed as follow. Around Γ(0, 0), the Fermi surface mainly contributed by Sb $5p$ are changed a lot both shape and width. This complicated reconstruction can be understood by tracing which orbital fillings are depleted by the holes introduced as a function of alkali-doping level x. Thus, by using integrated density of states we check doping for each element in DFT calculation and tight-binding model both that are shown in Fig. 5.8. In fact, it is easy to find that the majority of doped holes are in Sb orbitals whereas Ti $3d$ orbitals are nearly unaffected. The changes seen in Fermi surfaces with Ti $3d$ character are due to stronger Sb−Ti bonding upon hole doping rather than due to a Fermi level shift.

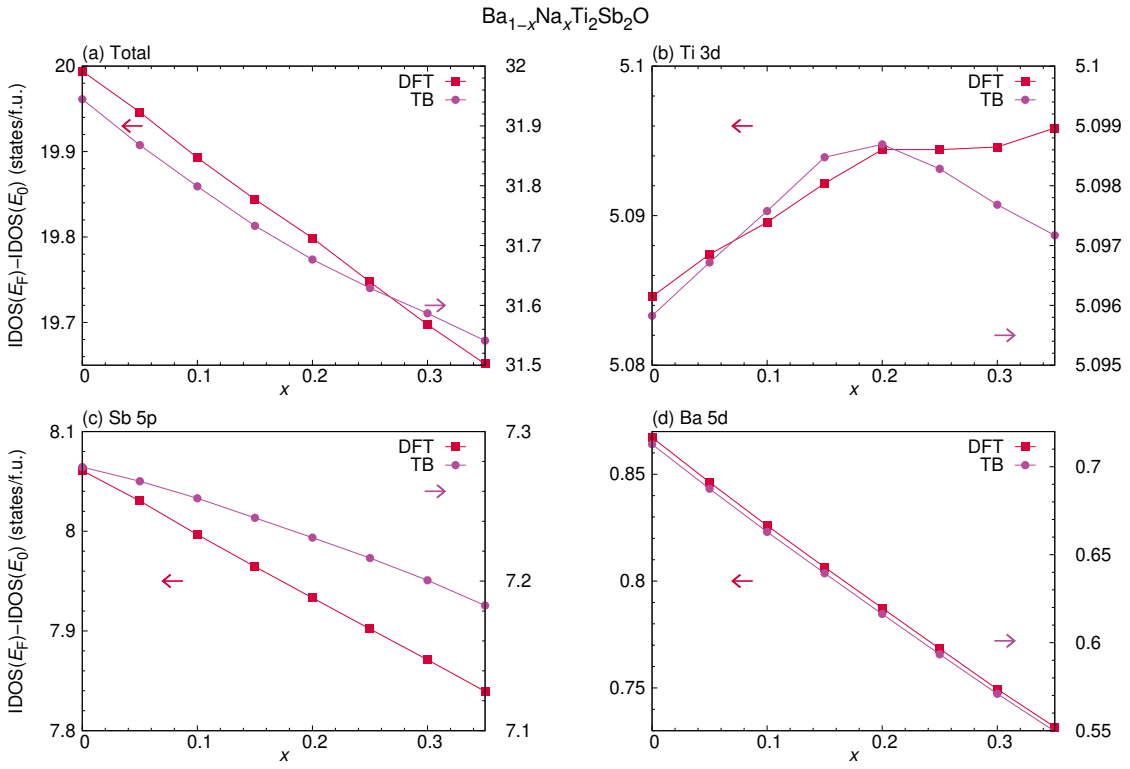

Figure 5.8: Integrated DOS of (a) total $Ba_{1-x}Na_xTi_2Sb_2O$, (b) Ti $3d$ orbitals, (c) Sb $5p$ orbitals and (d) Ba $5d$ orbitals both for DFT calculation and tight-binding model.

It is a little misleading that alkali-doping effects on Sb but does not effect on Ti directly. Even if the variation and reconstruction is huge for Sb dominated Fermi surface, we have to mention again that physical properties of $Ba_{1-x}Na_xTi_2Sb_2O$ are dominated by Ti $3d$ orbitals and hugely reconstructed Fermi surface of Sb orbitals do not change the physical properties of whole material, which is proved in the before density of states on Fermi level and the after susceptibilities and gap function. Therefore we mainly focus on the variation Fermi surface contributed by Ti. For Ti $3d$ dominated Fermi surfaces, around $X(\pi, 0)$, and $Y(0, \pi)$, they grow up obviously. But on $M(\pi, \pi)$, Fermi surfaces shrink slightly. And for last two locations, Fermi surfaces is contributed by $3d_{xy}$ orbital, which is consistent with our expectation. Comparing with band structure (Fig. 5.3), we can find that at X point there is hole-type character and at M point there is electron-type. The variation of Fermi surfaces with alkali-doping gives a hint that when we consider the susceptibility the nesting

vectors (π, 0) or (0, π) might lead a great change, which should be investigated carefully.

Moreover, the behavior of Fermi surfaces with alkali-doping suggests that VCA is a good tool to study the alkali-doping in titanium oxypnictide, which is also proven by the comparison between Fig. 5.2 and experimental [85] . Thus, the VCA is definitely successful to predict electronic structure of titanium oxypnictide with alkali-doping.

5.2.2 Results from RPA calculation

Next, beyond DFT, for measuring the relative importance of the Fermi surface changes, the susceptibility of $Ba_{1-x}Na_xTi_2Sb_2O$ is investigated. The non-interacting susceptibilities of each main orbital of Ti and Sb of $BaTi_2Sb_2O$ are shown in Fig. 5.9, which is calculated with the 26 band tight-binding models on 50×50×50 integration meshes. In Fig. 5.9, clearly susceptibilities of Ti $3d_{xy}$ orbitals are absolutely

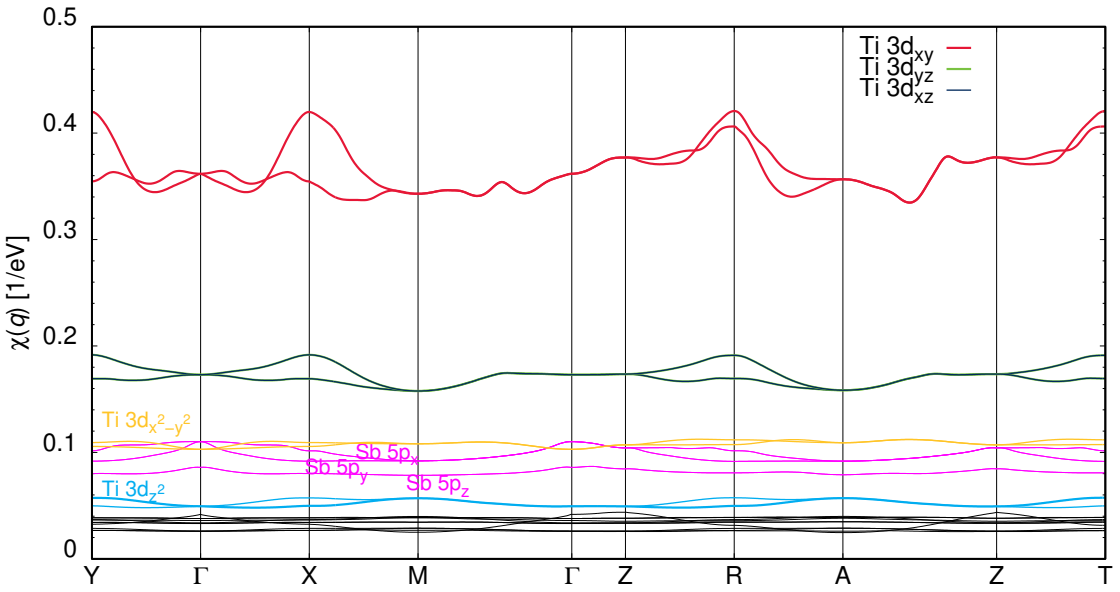

Figure 5.9: Non-interacting susceptibilities of $BaTi_2Sb_2O$ for main orbitals Ti $3d$, Ti $4s$, Sb $5p$, Ba $5d$, and O $2p$, in which orbitals of Ti and Sb are marked.

dominant. Then, as same as density of states the second largest susceptibilities is contributed by Ti $3d_{xz}$ and $3d_{yz}$ orbitals. Susceptibilities of Ti $3d_{z^2}$, $3d_{x^2-y^2}$, and Sb $5p$ are just the third largest. It is a little surprising that susceptibilities of Sb $5p$ are only quarter of susceptibilities of Ti $3d_{xy}$ orbitals, which, however, is one more strong

evidence to support our claim that $Ba_{1-x}Na_xTi_2Sb_2O$ physical properties are dominated by Ti $3d$ orbitals and not by Sb orbitals. Then we exhibit total susceptibility only with susceptibilities of $3d_{xy}$, $3d_{xz}$, and $3d_{yz}$, namely t_{2g} orbitals of Ti, via doping increase in Fig. 5.10. The behavior of total susceptibility and susceptibilities of each

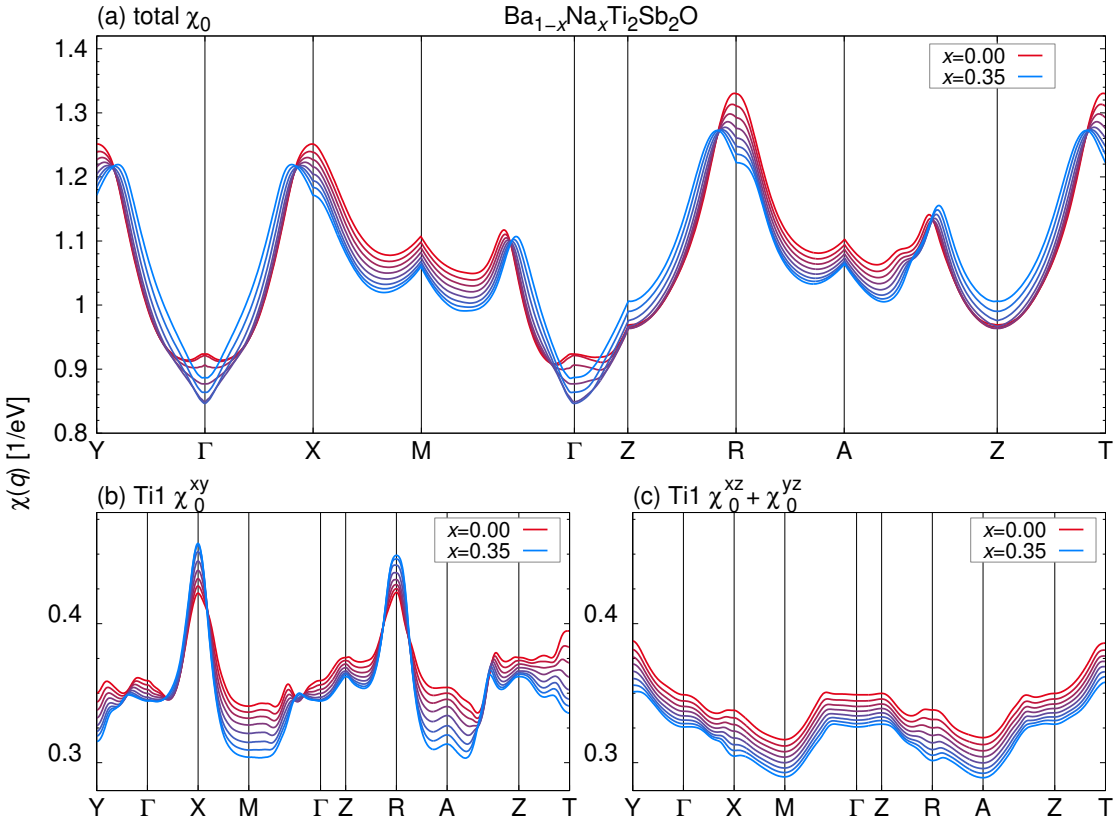

Figure 5.10: Non-interacting susceptibilities of $Ba_{1-x}Na_xTi_2Sb_2O$ for eight doping levels x. (a) total, (b) $3d_{xy}$ contribution from Ti1, (c) $3d_{xz}$ and $3d_{xz}$ contributions from Ti1.

orbital will be discussed separately. For total susceptibility showing in Fig. 5.10(a), it is clearly peaked at X, $\mathbf{q} = (\pi, 0, 0)$, and Y, $\mathbf{q} = (0, \pi, 0)$, which has been noted based on the Lindhard function calculated without matrix elements [26, 27]. With doping increasing even if the intensity of peaks around $X(Y)$ points is decreasing, comparing the ratio of total susceptibility χ_0 on X (or Y) and Γ, $\mathbf{q} = (0, 0, 0)$, actually the weight, namely importance, of peaks around $X(Y)$ points is increasing. Because, at the same time, total susceptibility χ_0 on Γ decreases largely. Moreover with increasing doping, the peaks around $X(Y)$ move toward to Γ. From the per-

spective of nesting vectors this behavior is due to the variation of shape of Fermi surface, but for deeply understanding this behavior it is needed to study the behavior further. For susceptibilities of each orbital there are some differences. It should be mentioned that becasue we only show susceptibilities of $3d$ orbitals for Ti1 atom, there is no symmetry on X and Y points for itself, and the symmetry can be found when susceptibilities are checked in the both of Ti sites, namely Ti1 and Ti2. In Fig. 5.10(b) there is the susceptibility of Ti $3d_{xy}$. First we focus on the Γ-X path. The most remarkable feature is that at X point peak of susceptibility becomes higher and sharper with increasing dpoing and it do not move toward to Γ point. But the valley between Γ and X trends to move toward to Γ. Meanwhile the tendency of intensity of susceptibility with increasing dpoing is changed. Close to X susceptibility increases with increased dpoing and oppositely close to Γ susceptibility decreases with increased dpoing. Then we look at the Y-Γ path. Generally susceptibility is decreased with increasing dpoing. However close to the midpoint of Y-Γ path there is a small interval that susceptibility almost does not be changed and the valley of susceptibility evolves to a small peak. Considering the symmetry of Ti1 and Ti2, reason of total susceptibility moving toward to Γ point can be explained by making the superposition for two Ti $3d_{xy}$ susceptibilities, which connects the total susceptibility and susceptibilities of each orbital and also shows the domination of Ti $3d_{xy}$ orbital. Furthermore on the Z-R path, even though the Fermi surface shows substantial k_z dispersion, we can find the improved nesting also in the R to Z like on the Γ-X path. Moreover comparing with Ti $3d_{xy}$, there are no special characteristics given by susceptibility of $3d_{xz}$+$3d_{yz}$. These comparatively featureless susceptibility

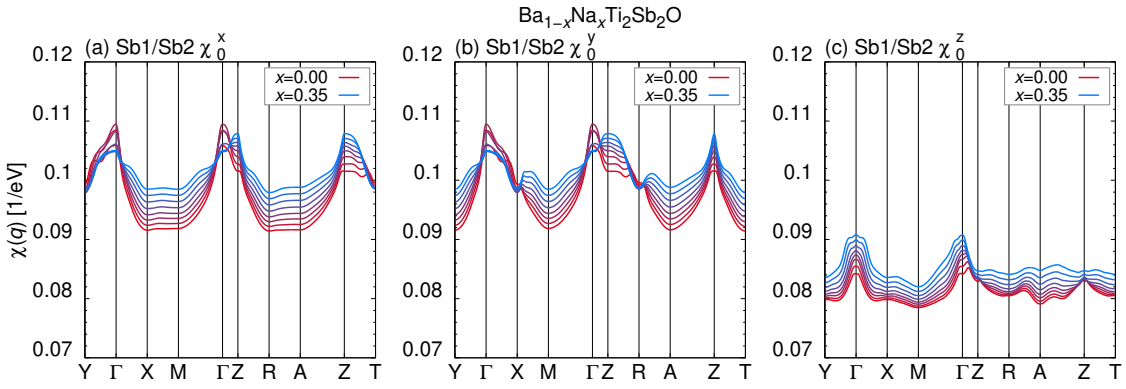

Figure 5.11: Sb contribution to the non-interacting susceptibilities for $Ba_{1-x}Na_xTi_2Sb_2O$ with doping.

uniformly decreases with doping shown in Fig. 5.10(c). Thus, the susceptibility of

$3d_{xz}$+$3d_{yz}$ just shifts with doping, which can be understood as Ti $3d_{xz}$ and $3d_{yz}$ do not dominate the physical properties of $Ba_{1-x}Na_xTi_2Sb_2O$. On the other hand, the Sb susceptibilities with doping are shown in Fig. 5.11. Similar with previous discussion, Sb susceptibilities are small, almost flat with respect to $\mathbf{q}$, and featureless with doping. It is proven again that physical properties of $Ba_{1-x}Na_xTi_2Sb_2O$ do not be decided by Sb.

For investigating $Ba_{1-x}Na_xTi_2Sb_2O$ further, we calculated non-interacting susceptibility and RPA interacting spin susceptibility both on the $q_z = 0$ 2D cuts of nesting vector plane, which is based on a 3D calculation of χ_0 on 25×25×9 grid using a 25×25×9 integration grid and $q_z = 0$ cuts are extracted using a 100×100 interpolation grid. In Fig. 5.12 we exhibit three doping level, $x = 0.00$, $x = 0.20$, and $x = 0.35$. For non-interacting susceptibility, with doping increased, we can find peaks

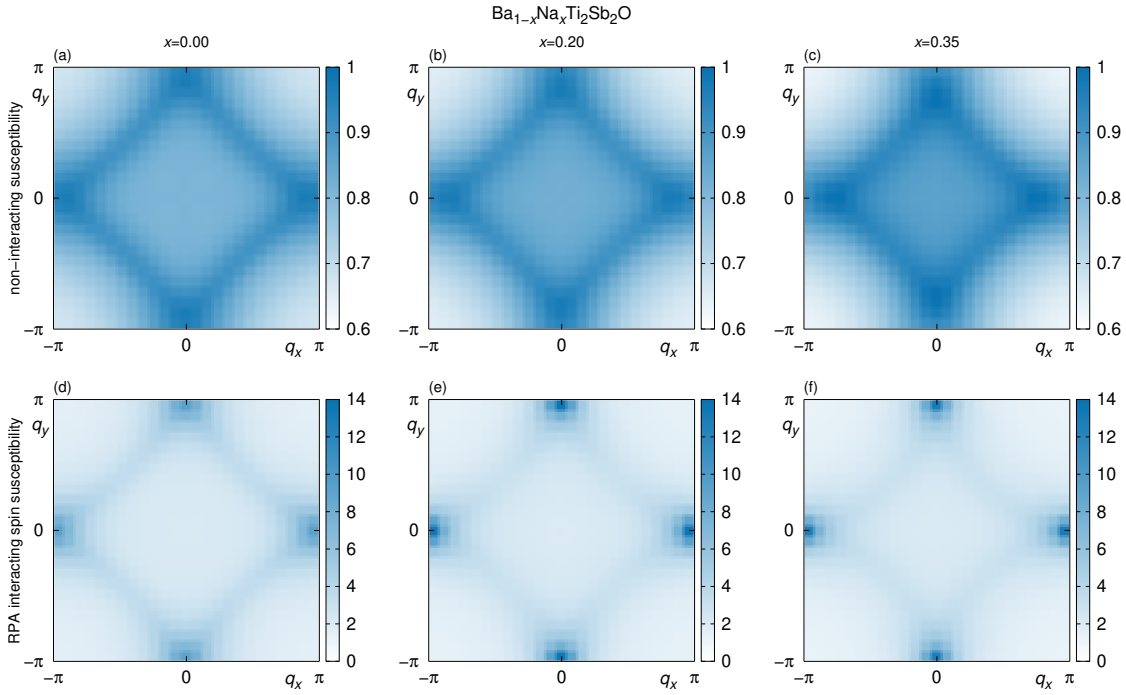

Figure 5.12: Non-interacting susceptibility χ_0 and RPA interacting spin susceptibility χ_s for $Ba_{1-x}Na_xTi_2Sb_2O$.

located on X and Y points move toward to Γ, which is mentioned before in Fig. 5.10 non-interacting susceptibilities on path. This result of 2D non-interacting susceptibility is good to compare with the result of rigid band approximation in Ref. [26]. It is confirmed again that our VCA result is effective to predict these materials. More-

over considering that the variation of Fermi surface is due to stronger Sb−Ti bonding upon hole doping rather than Fermi level shift, we would like to mention that our theoretical approximation using VCA is closer to real materials than rigid band approximation for reproducing or predicting Fermi surface, density of states and band structure. On the other hand for RPA interacting spin susceptibility, peaks located on X and Y point do not be moved but they are intensified with increased doping obtained by RPA, reminiscent of single orbital system behavior. These instabilities would now favor stripe-type magnetism, which is discussed in several theoretical studies but do not be observed experimentally for these materials [87].

Now we already have the complete data of susceptibility, and note that alkali-doping seems to lead to an overall decrease in susceptibility but strongly enhances the susceptibility of the Ti $3d_{xy}$ orbitals, we can expect them to be the main actor in T_c changes with doping. Then we will calculate pairing vertex and gap function to investigate physical properties of $Ba_{1-x}Na_xTi_2Sb_2O$ further. Since the similarity of susceptibilities along the $k_z = 0$ and $k_z = \pi$ paths in Fig. 5.10 indicates a high degree of two dimensionalit. We focus on the $k_z = 0$ cuts of pairing of leading parameter of gap function that are shown in Fig. 5.13. First of all, the largest intensity of pairing

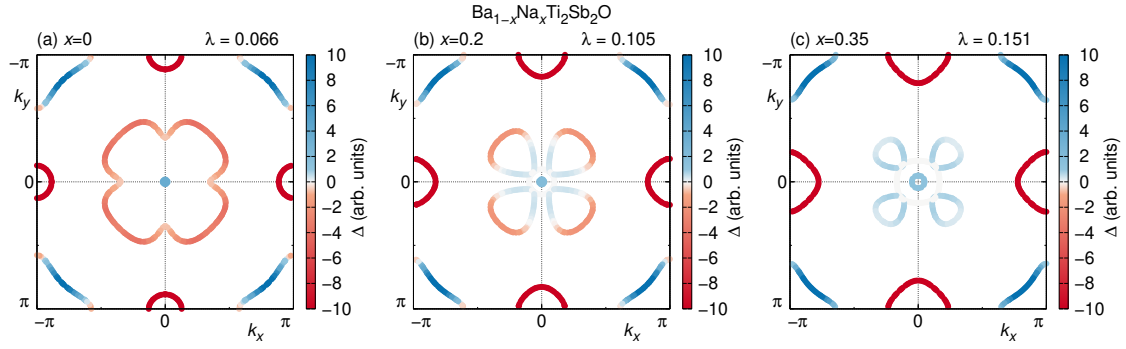

Figure 5.13: Eigen functions for the leading eigenvalue of the gap equation at zero doping (a), at middle doping (b) and at maximal doping (c), the sign-changing s-wave persists at all doping levels.

is located on the Fremi surface around X and Y points, and then on M points the intensity is still strong but the sign of pairing is changed, which favors a sign-changing s-wave superconducting order parameter. Comparing with the pairing intensity on Fremi surface around X, Y, or M, the pairing on the Fremi surface around Γ point is weak. Again it is consistent with our earlier explanation that Ti $3d$ orbitals, especially $3d_{xy}$ orbitals, dominate the physical properties of $Ba_{1-x}Na_xTi_2Sb_2O$ but orbitals of Sb are not dominant. Furthermore subleading d_{xy}- and $d_{x^2-y^2}$-type so-

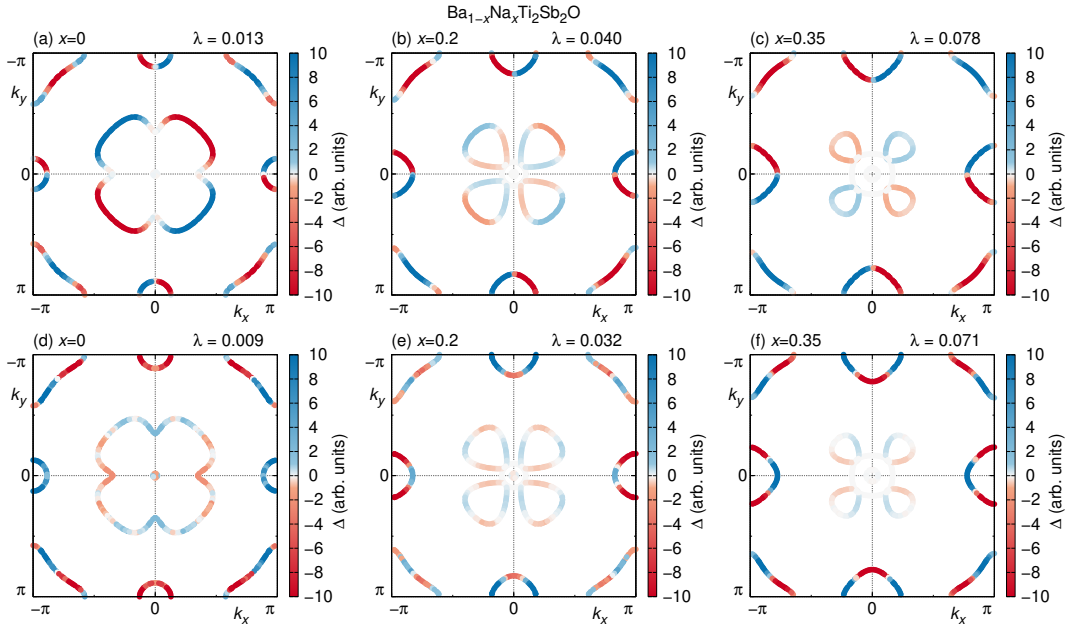

Figure 5.14: Eigen functions for the subleading eigenvalue of the gap equation at zero doping in first column, middle doping in second column, and maximal doping in third column. First row is subleading d_{xy}-type solutions and second row is second subleading $d_{x^2-y^2}$-type solutions.

lutions are shown in Fig. 5.14, of which have far smaller eigenvalues. Therefore subleading eigenvalues of gap equation are irrelevant in $Ba_{1-x}Na_xTi_2Sb_2O$. Then we only consider the leading eigenvalue of gap equation. The leading pairing symmetry shows that $Ba_{1-x}Na_xTi_2Sb_2O$ is a s-wave superconductor. Combining these features we can make a conclusion that $Ba_{1-x}Na_xTi_2Sb_2O$ and other alkali-doped titanium oxypnictides are the sign-changing s-wave unconventional superconductor. One more thing should be mentioned even though there are only three doping levels plotted in Fig. 5.13, features of gap equation and eigenvalues do not be changed on other doping level.

Then we will discuss the variation of leading eigenvalue of the gap equation along doping level. However before that situations of other alkali-doped titanium oxypnictides have to be mentioned. All characteristics of physical properties, like Fermi surface, susceptibility and so on, of K or Rb doped $BaTi_2Sb_2O$ are similar with physical properties of Na doping that are shown in several previous figures. Thus we do not show the details of $Ba_{1-x}K_xTi_2Sb_2O$ and $Ba_{1-x}Rb_xTi_2Sb_2O$. But for leading eigenvalues they have to be exhibited to compare with T_c.

Leading eigenvalue λ and T_c are shown in Fig. 5.15 (a) and for comparison the density of states on Fermi level $N(E_F)$ is shown in Fig. 5.15 (b), where T_c data are gotten from Ref. [18, 21, 23, 24]. In Fig. 5.15 (a), we can find that the tendency of

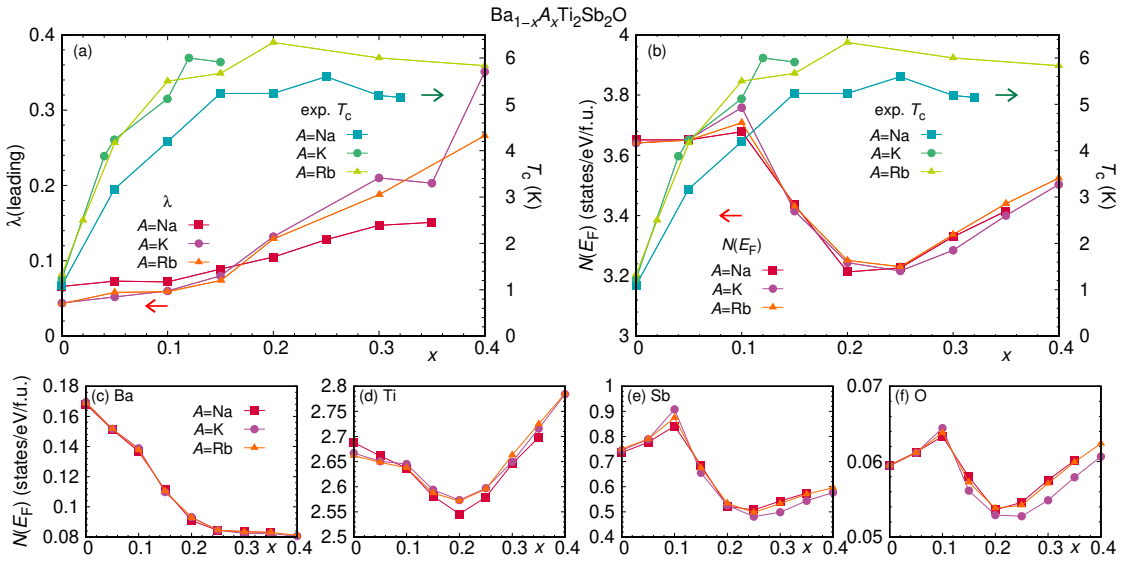

Figure 5.15: (a) Leading eigenvalues λ of the gap equation as a function of doping level x compare with T_c. (b) Density of states at the Fermi level $N(E_F)$ varying with doping level x compare with T_c. (c)-(f) Varied $N(E_F)$ for Ba, Ti, Sb, and O separately.

leading eigenvalues of all alkali-doped titanium oxypnictides are good to predict the T_c of themselves. As mentioned before, the BCS McMillan formula Eq. 5.1 is another way to understand the T_c tendencies. Thus, as a comparison we show the density of states on Fermi level $N(E_F)$ of $Ba_{1-x}A_xTi_2Sb_2O$ with their T_c again in Fig. 5.15 (b). Unfortunately, there is very little similarity between $N(E_F)$ and T_c evolution with doping. For example, in the case of $Ba_{1-x}Na_xTi_2Sb_2O$ T_c quickly increases from $T_c = 1.2$ K to a maximum that is reached between doping levels of $x = 0.1$ to 0.3. Meanwhile, $N(E_F)$ remains constant until $x = 0.1$ before going through a minimum around $x = 0.2$. Namely, T_c of alkali-doped titanium oxypnictides cannot be explained by the density of states at the Fermi level using BCS formula like conventional superconductors, and it is clearly explained by the susceptibility trends.

Additionally, for understanding the behavior of the density of states on Fermi level, $N(E_F)$ is separate into each element shown in Fig. 5.15 (c)-(f). By checking the difference of $N(E_F)$ with varying doping, it is found that the variation of $N(E_F)$

of whole system is mainly controlled by Sb and the second large influence comes from Ti. This behavior consists with our discussion that alkali-doping directly effects on Sb, and then Ti is influenced by the Sb−Ti bonding. It should be noticed that for titanium oxypnictides superconductivity is supposed to relate with the behavior of Ti 3d orbitals. Thus this Sb controlled density of states on Fermi level gives an answer of the question that why T_c cannot be expected by $N(E_F)$ using BCS formula. However, beyond x=0.2, variation of $N(E_F)$ of Ti is larger than Sb, comparing with Fermi surface shown in Fig. 5.6, which is the consequence of shrunken Fermi surface of Sb 5p orbitals. If it is considered as Ti beats Sb to controls the Fermi surface, it might be another perspective to understand the superconductivity of alkali-doped titanium oxypnictides.

Combining evidences shown above we can conclude again that these alkali-doped titanium oxypnictides are the sign-changing s-wave unconventional superconductors, of which T_c can be explained by the leading eigenvalues λ of the gap equation with increasing doping.

5.3 Conclusion

In this chapter, we use density functional theory and spin-fluctuation theory to study the electronic structure and superconducting properties of $Ba_{1-x}Na_xTi_2Sb_2O$. We modeled the crystal structure evolution using an interpolation of experimental lattice parameters and antimony position is predicted by relaxation using DFT with fixed lattice parameters.

The density of states at the Fermi-level $N(E_F)$ shows a trend which is in sharp contrast to the evolution of the superconducting T_c. It would be an indication that transition temperatures may not be accounted for by an electron-phonon mechanism.

Although the band structure and density of states show that constituents of $Ba_{1-x}A_xTi_2Sb_2O$ (A = Na, K, and Rb) are strongly hybridized and many orbitals lie close to the Fermi level, we have found that the susceptibility is completely dominated by the Ti $3d_{xy}$ orbitals.

We find that the trend of T_c can be satisfactorily explained by a spin-fluctuation pairing mechanism. There is a sign-changing s-wave order parameter with nonuniform gap size on the various Fermi surface sheets which is absolutely dominant for all doping levels of $Ba_{1-x}Na_xTi_2Sb_2O$.

Chapter 6

Phase transition and magnetism in ternary chromium tellurides

Ternary chromium tellurides are a sort of layered materials with honeycomb lattice of Cr atoms, in which extraordinary properties are searching by theoretical researchers and willing to be made as new-type of devices by engineers.

At the beginning of investigation of chromium tellurides $CrSiTe_3$ and $CrGeTe_3$ initially investigators consider them as bulk ferromagnetic semiconductors [88–90] with Curie temperatures (ordering temperatures) $T_{\text{Curie}} = 32$ K [91] and $T_{\text{Curie}} = 61$ K [92], respectively.

In 2020, superconductivity with a structure transition of $CrSiTe_3$ under pressure is reported [36], which is an exciting for chromium tellurides. However, in another study that concentrates on structure of $CrSiTe_3$ under pressure, they do not find the structure transition along increasing pressure [93].

On the other hand, similarly, under pressure an insulator-metal transition of $CrGeTe_3$ is reported [94].

In this chapter, we will employ density functional theory (DFT), energy mapping and dynamical mean-field theory (DMFT) to study the electronic, magnetic properties, and phase transition of $CrGeTe_3$ along increasing pressure.

6.1 Methods

The crystal structure with space group $R\bar{3}$ of $CrSiTe_3$ and $CrGeTe_3$ is shown in Fig. 1.6, section 1.3, of which trigonal crystal system lets us know that we have to consider this structure carefully and to use hexagonal structure or rhombohedral structure case by case depends on the requirements of calculation.

Before calculating electronic structure we have to decided the lattice parameters. Because only a few studies report the evolution of lattice parameters and variation of atoms sites with varying crystal structure of $CrSiTe_3$ and $CrGeTe_3$ along pressure. Thus, we have two different way to decided the parameters, (1) to use experimental structure directly, (2) to relax crystal structure under pressure to get the predicted structure with lattice parameters and atoms sites. At the beginning, we try to use the Vienna Ab initio Simulation Package (VASP) to make relaxation and predict the structure under pressure. Then we found a very big problem shown in Fig. 6.1. The

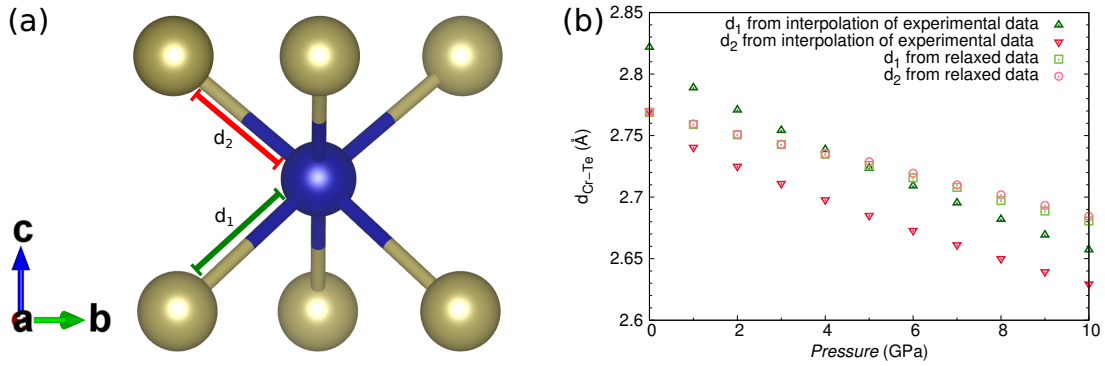

Figure 6.1: The distance of Cr-Te bonds for experimental data and relaxation data separately. (a) Two Cr-Te bonds are marked in $CrTe_6$ distorted triangular prism. (b) Variation of distance of two Cr-Te bonds along pressure for experimental data and relaxation data separately.

problem is that experimental data give two Cr-Te bonds with different distances but in DFT the relaxation forces these two Cr-Te bonds to be identical. It is a total catastrophe that leads us to give up on using relaxation structure. Thus, our study only focus on $CrGeTe_3$ of which experimental data of lattice parameters and atom sites are sufficient for calculation.

Firstly, we use the experimental data to run DFT to get electronic structure of $CrGeTe_3$, in which we can get electronic structure of material. Secondly, we apply the DFT with GGA+U in Heisenberg model to study exchange couplings to derive Curie-Weiss temperature θ_{CW} that is the important result to compare with experiment. Thirdly, for explaining the pressure-temperature phase diagram from expertment, we apply the DFMT for investigating the finite temperature cases.

6.2 Electronic structure

The crystal structure and lattice parameters of $CrGeTe_3$ along increasing pressure is reported in Ref. [95] detailedly. Before DFT calculation we will prepare a interpolation by using these data to get smooth parameters along pressure and to avoid experimental error, which is exhibited in Fig. 6.2. Only in this way, we can

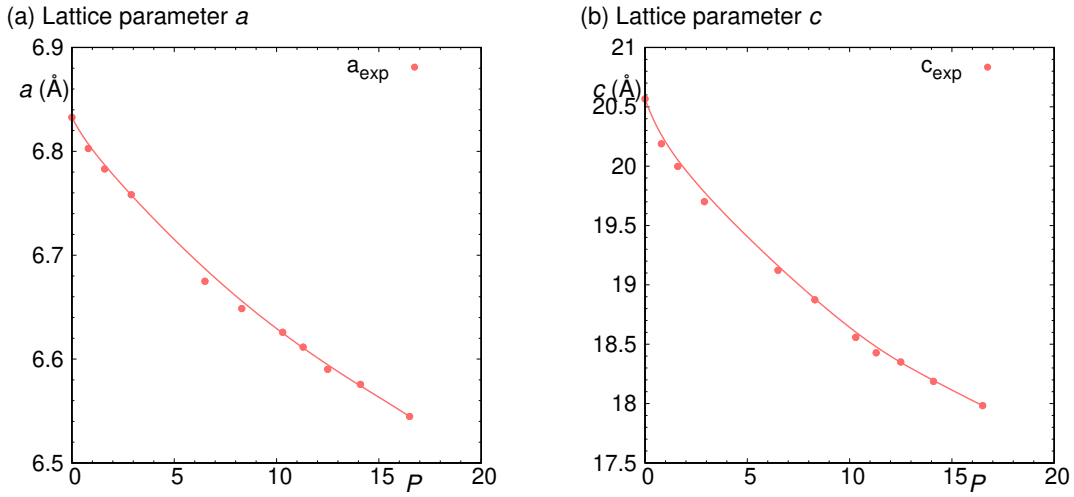

Figure 6.2: Interpolation of experimental lattice constants of $CrGeTe_3$.

apply DFT calculation along pressure reasonably.

By apply this data into DFT, we obtain the electronic structure of $CrGeTe_3$ in ferromagnetic state. The band structure with highlighted orbital character is exhibited in Fig. 6.3, where we can find that Cr $3d_{yz}$, Cr $3d_{xz}$, and Te $5p$ orbitals are most close to Fermi level. Moreover, this natural degeneracy of Cr $3d_{yz}$ and $3d_{xz}$ orbitals prove that our understanding of the environment of Cr is correct, in which around Cr atom, 6 Te atoms made the distorted triangular prism $CrTe_6$ and did not make an octahedron.

Furthermore, there is another characteristic of structure of $CrGeTe_3$ shown in the Fig. 6.4(c) that there is a honeycomb lattice made by Cr atom. Then we apply DFT with GGA+U for investigating exchange couplings of Cr in Heisenberg model. We set several spin configurations of Cr atoms and make a supercell like Fig. 6.4(c). For different spin configurations we can get different total energies by DFT with GGA+U. And we know that in Heisenberg model the total energies can be calculated by exchange couplings. Reversely, we can solve a part of exchange couplings by using different total energies of different spin configurations. Then we get the evolution of

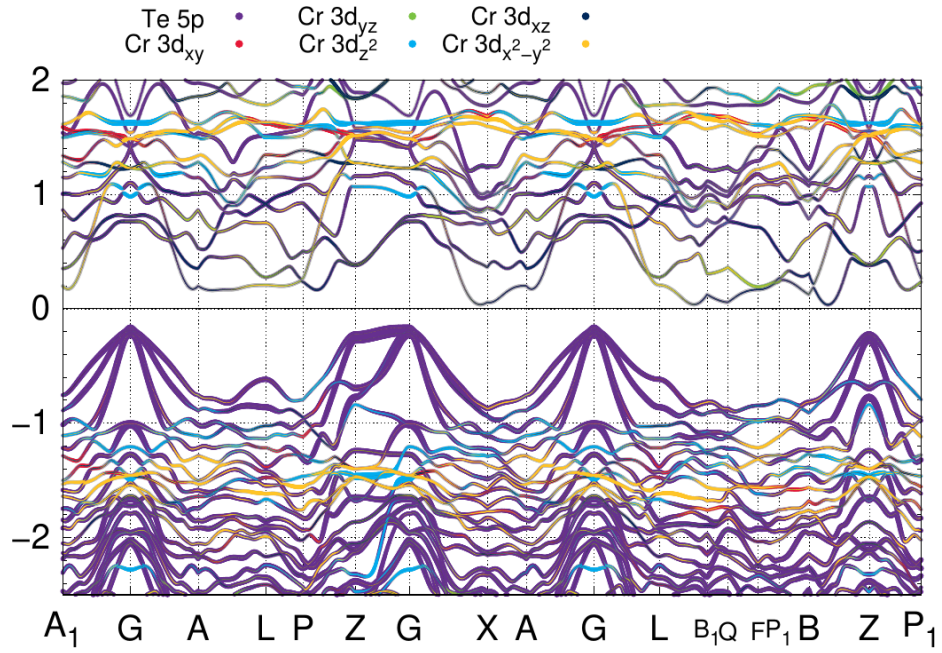

Figure 6.3: Band structure with highlighted Cr 3d and Te 5p orbitals.

exchange couplings J_1, J_2, J_3, J_4, J_5, J_6, J_7, and J_9 in Fig. 6.4(a).

With increasing pressure we can find that ferromagnetic coupling J_1 and antiferromagnetic coupling J_2 are increased together, which is difficult to decide that the material will keep ferromagnetic state or antiferromagnetic state because of competition. Moreover, by using these couplings the Curie-Weiss temperature θ_{CW} can be computed, of which the evolution along pressure is shown in Fig. 6.4(b). It is exciting that not only the quantitative value of θ_{CW} is close to experimental value but also the behavior of θ_{CW}, with increasing pressure first keeping almost constant and then suddenly rising, is similar to the results of Ref. [94]. Furthermore, in Fig. 6.4(d) the averaged charge gap will be closed around 5GPa, which supports the insulator-mental transition of $CrGeTe_3$. We think that from DFT with GGA+U calculation these results are comparable with experiment.

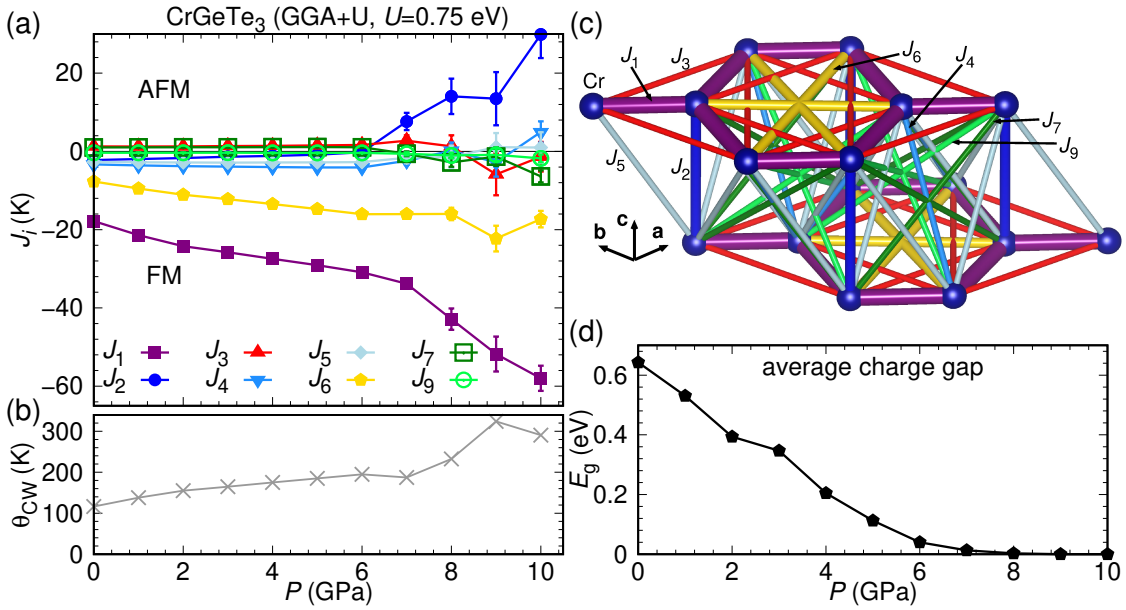

Figure 6.4: Energy mapping by DFT with GGA+U to predicted (a) exchange couplings of Cr, (b) Curie-Weiss temperature $\theta_{\rm CW}$ and (d) avearged charge gap.

6.3 Insulator-metal transition

We already find the insulator-mental transition in Fig. 6.4(d). Next, we will show more evidence of insulator-mental transition of $CrGeTe_3$. First, we exhibit the band structure and density of states along pressure in Fig. 6.5. Obviously, at 0GPa, Fig. 6.5(a), there is insulating state and at 5GPa, Fig. 6.5(b), it already becomes metallic state. On the other hand, combining Fig. 6.3 and 6.5, it is still a little surprise that on Fermi level the dominant orbitals are not Cr $3d$ orbitals but Te $5p$ orbitals. This result push us to consider the importance of coupling between Cr $3d$ and Te $5p$ orbitals. Moreover for Te $5p$ orbitals, because Te is an enough heavy element, it is necessary to include the spin-orbital coupling.

Then, by using Wannier functions we pick up the local potential and hopping to make the (Wannier90 type) tight-binding model into the DMFT calculation. In DMFT calculation, we consider Cr $3d$ and Te $5p$ orbitals together and also introduce the spin-orbital coupling. The DMFT spectral function is exhibited in Fig. 6.6. However there is a numerical problem for Fermi level that should be moved down about -0.2eV, which is already shifted in Fig. 6.6. These figures are thought as another evidence of insulator-mental transition at finite temperature that can be

compared with the angle-resolved photoemission spectroscopy (ARPES) results from experiment.

6.4 Conclusion

In this chapter, we use density functional theory and dynamical mean-field theory to study the electronic structure, spectral function, and pressure-temperature phase diagram of $CrGeTe_3$. The crystal structure evolution along pressure is modeled by using an interpolation of experimental lattice parameters and antimony position.

The density of states by DFT shows that in this material the importance of Te $5p$ orbitals is same as Cr $3d$ orbitals. Applying DFT with GGA+U in Heisenberg model, the Curie-Weiss temperature θ_{CW} is calculated by energy mapping along pressure, of which value and trend are both comparable with experiment.

The insulator-metal transition along pressure is observed both in DFT band structure and DMFT spectral function.

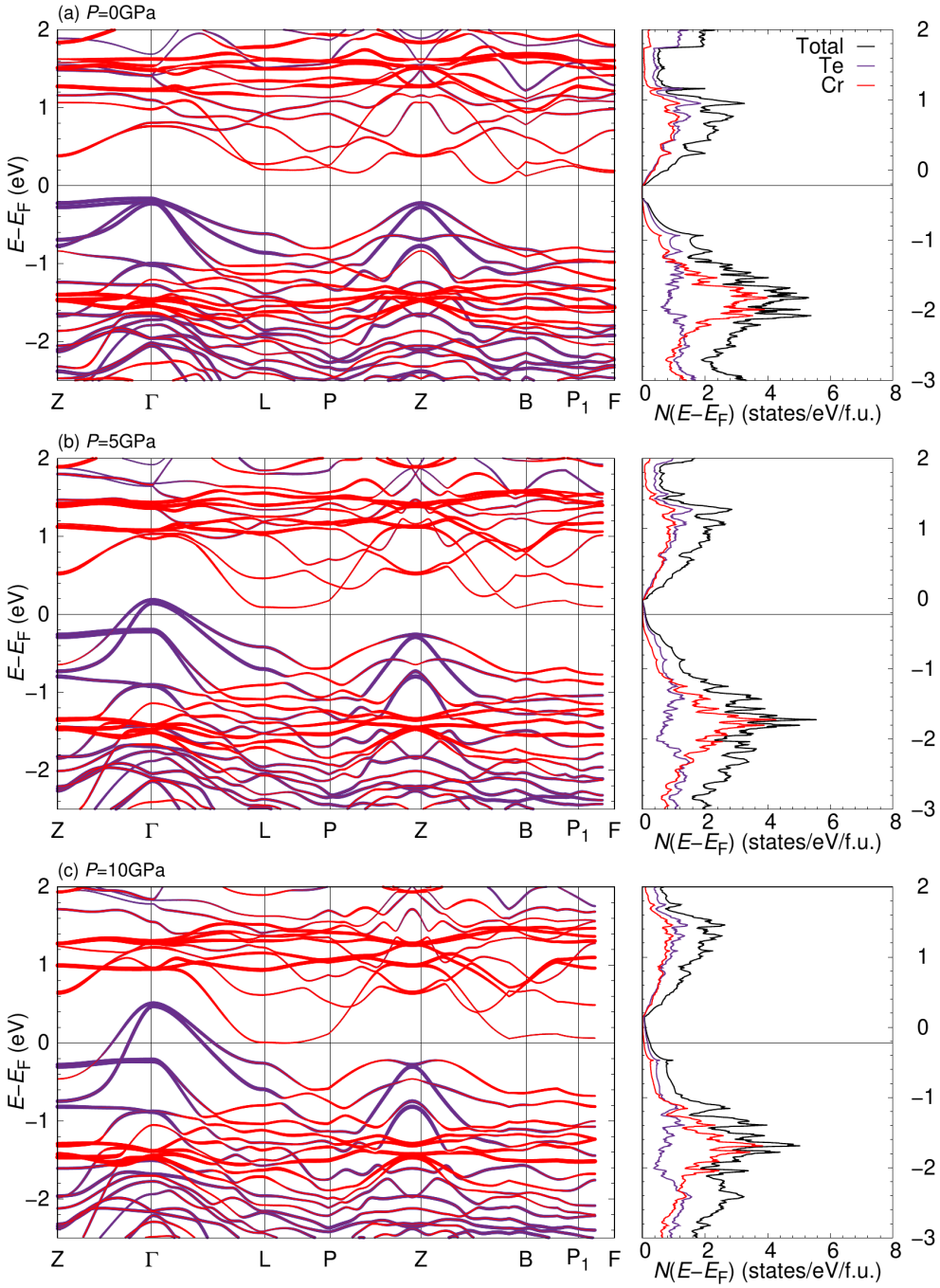

Figure 6.5: Insulator-metal transition shown by DFT band structure and density of states at 0, 5, and 10GPa. Cr is marked by red and Te is marked by violet.

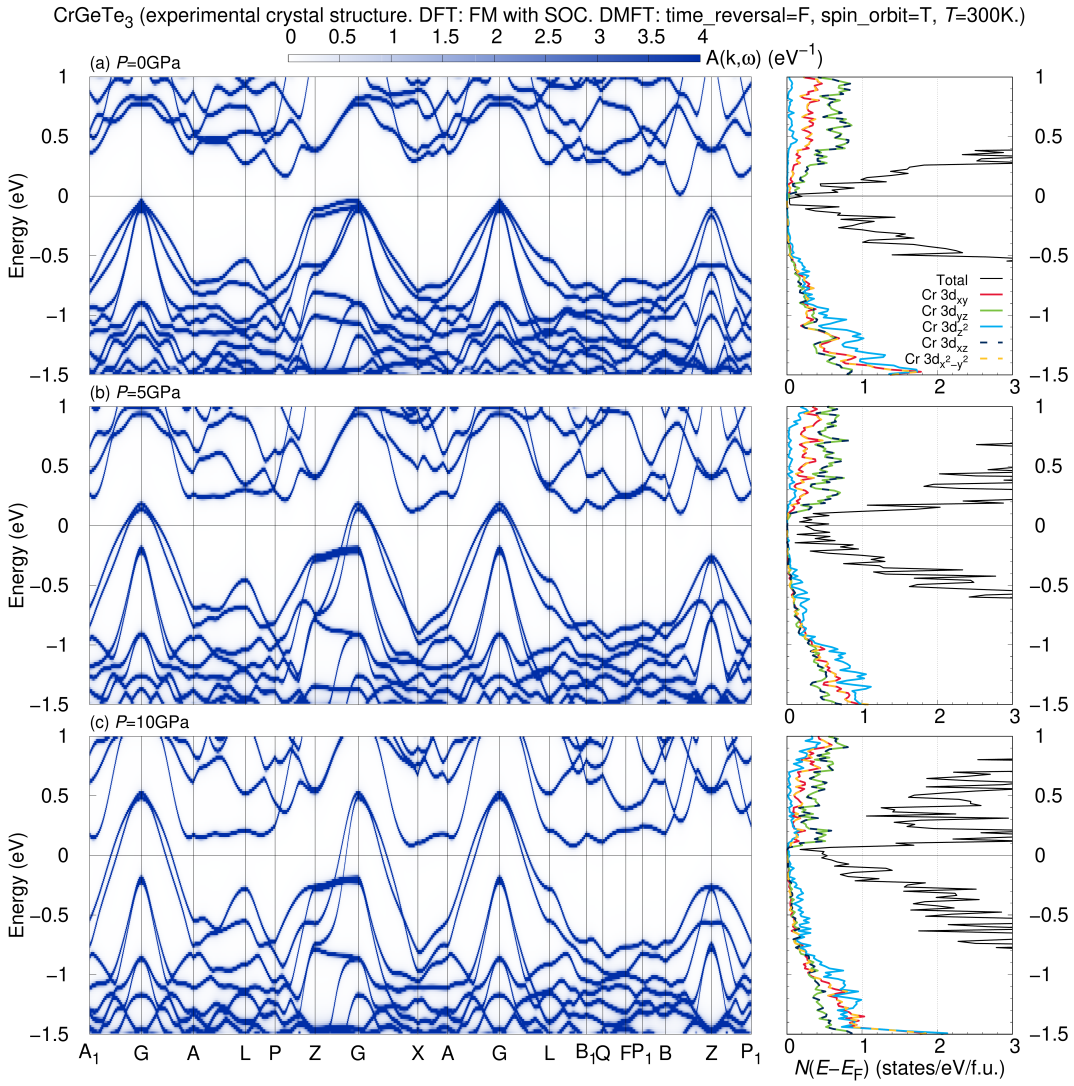

Figure 6.6: Insulator-metal transition shown by DMFT spectral function at 0, 5, and 10GPa.

Chapter 7

Summary and Outlook

In this thesis, we used several theoretical methods, including density functional theory, spin-fluctuation theory, and dynamical mean-field theory, to investigate two kinds of materials, titanium oxypnictides and chromium tellurides, which both belong to $3d$ electron system like cuprates and iron-based superconductors.

In chapter 1, we introduce the background of superconductor and superconductivity, previous studies and crystal structure of titanium-based superconductors and ternary chromium tellurides. In chapter 2, one of the most powerful theories for today's studies of many-body system, the density functional theory (DFT) is introduced. We give the details of Kohn-Sham auxiliary system and Generalized-gradient approximations (GGA). Moreover, solving process of Full-potential local-orbital (FPLO) minimum-basis codes is discussed. In chapter 3, beyond DFT, we introduce the random phase approximation (RPA) to realize the spin fluctuation theory, in which the electron-electron interaction is considered. In this framework, we exhibit the derivation of susceptibilities and two-electron pairing vertex. In chapter 4, we discuss another method for strongly correlated systems, the dynamical mean-field theory, which is a useful method to calculate finite temperature cases and to compare with experimental results. In chapter 5 and 6, physical properties of titanium oxypnictides and chromium tellurides are investigate separately.

7.1 Titanium oxypnictides

For titanium oxypnictides, the electronic structures of $Ba_{1-x}A_xTi_2Sb_2O$ with varying alkali-doping (A=Na, K, Rb) are investigated theoretically. By using DFT , we determine density of states and band structure with the orbital character. However, only using the density of states at the Fermi-level $N(E_F)$ cannot explain the

evolution of the superconducting T_c, which indicates that transition temperatures may not be accounted for by an electron-phonon mechanism. Then we extract a tight-binding model for $Ba_{1-x}A_xTi_2Sb_2O$ by using projective Wannier functions and apply the RPA to calculate susceptibilities and pairing vertex for revealing the superconducting order parameters of the gap function. The gap function shows the sign-changing s-wave character for all doping level, and leading eigenvalues λ of gap function is good to predict the T_c of titanium oxypnictides with alkali-doping. Combining with the result of McMillan formula, our study gives the evidence to support that titanium oxypnictides are unconventional superconductors.

Next, when we know that the alkali doping do not effect on Ti directly, how it works to control electronic structure and superconductivity is an interesting question that will be studied in future. Moreover, explaining the nontrivial transition temperature trends of titanium based superconductors with isoelectronic doping and pressure are interesting future fields of study. Methodologically, it may be important to consider also the energy dependence within the FLEX.

7.2 Chromium tellurides

For chromium tellurides, we study the insulator-metal transition of $CrGeTe_3$ along increasing pressure. The insulator-metal transition along pressure is observed both in DFT and DMFT of which results can be used to compare ARPES experimentally. From energy mapping by using DFT with GGA+U, a comparable Curie-Weiss temperature θ_{CW} varying with pressure is given.

Then, by combining the DMFT spectral function and energy mapping in Heisenberg model, we want to thoroughly explain the pressure-temperature phase diagram of $CrGeTe_3$ from experiment.

References

[1] M. Strasik, J. R. Hull, J. A. Mittleider, J. F. Gonder, P. E. Johnson, K. E. McCrary, and C. R. McIver. An overview of boeing flywheel energy storage systems with high-temperature superconducting bearings. *Supercond. Sci. Technol.*, 23:034021, 2010.

[2] Habibo Brechna. *Superconducting magnet systems*. Springer, 1973.

[3] Arno Godeke. A review of the properties of Nb_3Sn and their variation with A15 composition, morphology and strain state. *Supercond. Sci. Technol.*, 19:R68, 2006.

[4] H. Kamerlingh Onnes. Further experiments with liquid helium. C. on the change of electric resistance of pure metals at very low temperatures, etc. IV. The resistance of pure mercury at helium temperatures. *Commun. Phys. Lab. Univ. Leiden, b*, 120, 1911.

[5] John Bardeen, Leon N. Cooper, and John R. Schrieffer. Theory of superconductivity. *Phys. Rev.*, 108:1175, 1957.

[6] J. George Bednorz and K. Alex Müller. Possible high T_c superconductivity in the Ba-La-Cu-O system. *Z. Phys. B Condens. Matter*, 64:189, 1986.

[7] Yoichi Kamihara, Hidenori Hiramatsu, Masahiro Hirano, Ryuto Kawamura, Hiroshi Yanagi, Toshio Kamiya, and Hideo Hosono. Iron-based layered superconductor: LaOFeP. *J. Am. Chem. Soc.*, 128:10012, 2006.

[8] A. Adam and H-U. Schuster. Darstellung und kristallstruktur der pnictidoxide $Na_2Ti_2As_2O$ und $Na_2Ti_2Sb_2O$. *Z. Anorg. Allg. Chem.*, 584:150, 1990.

[9] E.A. Axtell III, Tadashi Ozawa, Susan M. Kauzlarich, and Rajiv R.P. Singh. Phase transition and spin-gap behavior in a layered tetragonal pnictide oxide, 1997.

[10] W. E. Pickett. Electronic instability in inverse-K_2NiF_4-structure $Na_2Sb_2Ti_2O$. *Phys. Rev. B*, 58:4335, 1998.

[11] Takeshi Yajima, Kousuke Nakano, Fumitaka Takeiri, Yasumasa Nozaki, Yoji Kobayashi, and Hiroshi Kageyama. Two superconducting phases in the isovalent solid solutions $BaTi_2Pn_2O$ (Pn= As, Sb, and Bi). *J. Phys. Soc. Jpn.*, 82:033705, 2013.

[12] Yanan Wang, Huan Li, Tomoya Taguchi, Ai Suzuki, Akari Miura, Hidenori Goto, Ritsuko Eguchi, Takafumi Miyazaki, Yen-Fa Liao, Hirofumi Ishii, and Yoshihiro Kubozono. Superconducting behavior of $BaTi_2Bi_2O$ and its pressure dependence. *Phys. Chem. Chem. Phys.*, 22:23315, 2020.

[13] Tomoya Taguchi, Yanan Wang, Xiaofan Yang, Huan Li, Yasuhiro Takabayashi, Kouichi Hayashi, Takafumi Miyazaki, Yen-Fa Liao, Hirofumi Ishii, Hidenori Goto, Ritsuko Eguchi, and Yoshihiro Kubozono. Emergence of a pressure-driven superconducting phase in $Ba_{0.77}Na_{0.23}Ti_2Sb_2O$. *Inorganic Chemistry*, 60:3585, 2021.

[14] Takeshi Yajima, Kousuke Nakano, Fumitaka Takeiri, Toshio Ono, Yuko Hosokoshi, Yoshitaka Matsushita, James Hester, Yoji Kobayashi, and Hiroshi Kageyama. Superconductivity in $BaTi_2Sb_2O$ with a d^1 square lattice. *J. Phys. Soc. Jpn.*, 81:103706, 2012.

[15] Takeshi Yajima, Kousuke Nakano, Fumitaka Takeiri, James Hester, Takafumi Yamamoto, Yoji Kobayashi, Naruki Tsuji, Jungeun Kim, Akihiko Fujiwara, and Hiroshi Kageyama. Synthesis and physical properties of the new oxybismuthides $BaTi_2Bi_2O$ and $(SrF)_2Ti_2Bi_2O$ with a d^1 square net. *J. Phys. Soc. Jpn.*, 82:013703, 2012.

[16] Hui-Fei Zhai, Wen-He Jiao, Yun-Lei Sun, Jin-Ke Bao, Hao Jiang, Xiao-Jun Yang, Zhang-Tu Tang, Qian Tao, Xiao-Feng Xu, Yu-Ke Li, Chao Cao, Jian-Hui Dai, Zhu-An Xu, and Guang-Han Cao. Superconductivity, charge- or spin-density wave, and metal-nonmetal transition in $BaTi_2(Sb_{1-x}Bi_x)_2O$. *Phys. Rev. B*, 87:100502, 2013.

[17] X. F. Wang, Y. J. Yan, J. J. Ying, Q. J. Li, M. Zhang, N. Xu, and X. H. Chen. Structure and physical properties for a new layered pnictide-oxide: $BaTi_2As_2O$. *J. Condens. Matter Phys.*, 22:075702, 2010.

[18] Phuong Doan, Melissa Gooch, Zhongjia Tang, Bernd Lorenz, Angela Möller, Joshua Tapp, Paul C. W. Chu, and Arnold M. Guloy. $Ba_{1-x}Na_xTi_2Sb_2O$ ($0.0 \leq x \leq 0.33$): A layered titanium-based pnictide oxide superconductor. *J. Am. Chem. Soc.*, 134:16520, 2012.

[19] R. H. Liu, D. Tan, Y. A. Song, Q. J. Li, Y. J. Yan, J. J. Ying, Y. L. Xie, X. F. Wang, and X. H. Chen. Physical properties of the layered pnictide oxides $Na_2Ti_2P_2O$ (P=As, Sb). *Phys. Rev. B*, 80:144516, 2009.

[20] Shunsaku Kitagawa, K. Ishida, Kousuke Nakano, Takeshi Yajima, and H. Kageyama. s-wave superconductivity in superconducting $BaTi_2Sb_2O$ revealed by $^{121/123}$Sb-NMR/nuclear quadrupole resonance measurements. *Phys Rev. B*, 87:060510, 2013.

[21] Fabian von Rohr, Andreas Schilling, Reinhard Nesper, Chris Baines, and Markus Bendele. Conventional superconductivity and charge-density-wave ordering in $Ba_{1-x}Na_xTi_2Sb_2O$. *Phys. Rev. B*, 88:140501(R), 2013.

[22] Y. Nozaki, K. Nakano, T. Yajima, H. Kageyama, B. Frandsen, L. Liu, S. Cheung, T. Goko, Y. J. Uemura, T. S. J. Munsie, T. Medina, G. M. Luke, J. Munevar, D. Nishio-Hamane, and C. M. Brown. Muon spin relaxation and electron/neutron diffraction studies of $BaTi_2(As_{1-x}Sb_x)_2O$: Absence of static magnetism and superlattice reflections. *Phys Rev. B*, 88:214506, 2013.

[23] Ursula Pachmayr and Dirk Johrendt. Superconductivity in $Ba_{1-x}K_xTi_2Sb_2O$ ($0 \leq x \leq 1$) controlled by the layer charge. *Solid State Sci.*, 28:31, 2014.

[24] Fabian von Rohr, Reinhard Nesper, and Andreas Schilling. Superconductivity in rubidium-substituted $Ba_{1-x}Rb_xTi_2Sb_2O$. *Phys. Rev. B*, 89:094505, 2014.

[25] Yanan Wang, Xiaofan Yang, Tomoya Taguchi, Huan Li, Tong He, Hidenori Goto, Ritsuko Eguchi, Takafumi Miyazaki, Yen-Fa Liao, Hirofumi Ishii, and Yoshihiro Kubozono. Preparation and characterization of superconducting $Ba_{1-x}Cs_xTi_2Sb_2O$, and its pressure dependence of superconductivity. *Jpn. J. Appl. Phys.*, 58:110603, 2019.

[26] David J. Singh. Electronic structure, disconnected fermi surfaces and antiferromagnetism in the layered pnictide superconductor $Na_xBa_{1-x}Ti_2Sb_2O$. *New J. Phys.*, 14:123003, 2012.

[27] Guangtao Wang, Huiping Zhang, Lin Zhang, and Chang Liu. The electronic structure and magnetism of $BaTi_2Sb_2O$. *J. Appl. Phys.*, 113:243904, 2013.

[28] Melissa Gooch, Phuong Doan, Zhongjia Tang, Bernd Lorenz, Arnold M. Guloy, and Paul C. W. Chu. Weak coupling BCS-like superconductivity in the pnictide oxide $Ba_{1-x}Na_xTi_2Sb_2O$ (x = 0 and 0.15). *Phys. Rev. B*, 88:064510, 2013.

[29] Sirko Kamusella, Phuong Doan, Til Goltz, Hubertus Luetkens, Rajib Sarkar, Arnold Guloy, and Hans-Henning Klauss. Cdw order and unconventional s-wave superconductivity in $Ba_{1-x}Na_xTi_2Sb_2O$. In *J. Phys. Conf. Ser.*, volume 551, page 012026. IOP Publishing, 2014.

[30] Cheng Gong, Lin Li, Zhenglu Li, Huiwen Ji, Alex Stern, Yang Xia, Ting Cao, Wei Bao, Chenzhe Wang, Yuan Wang, Z. Q. Qiu, R. J. Cava, Steven G. Louie, Jing Xia, and Xiang Zhang. Discovery of intrinsic ferromagnetism in two-dimensional van der Waals crystals. *Nature*, 546:265, 2017.

[31] Xingxing Li and Jinlong Yang. $CrXTe_3$ (X= Si, Ge) nanosheets: two dimensional intrinsic ferromagnetic semiconductors. *J. Mater. Chem. C*, 2:7071, 2014.

[32] Cheng Gong and Xiang Zhang. Two-dimensional magnetic crystals and emergent heterostructure devices. *Science*, 363:eaav4450, 2019.

[33] Michael A. McGuire, Hemant Dixit, Valentino R. Cooper, and Brian C. Sales. Coupling of crystal structure and magnetism in the layered, ferromagnetic insulator CrI_3. *Chem. Mater.*, 27:612, 2015.

[34] Bevin Huang, Genevieve Clark, Efrén Navarro-Moratalla, Dahlia R. Klein, Ran Cheng, Kyle L. Seyler, Ding Zhong, Emma Schmidgall, Michael A. McGuire, David H. Cobden, Wang Yao, Di Xiao, Pablo Jarillo-Herrero, and Xiaodong Xu. Layer-dependent ferromagnetism in a van der Waals crystal down to the monolayer limit. *Nature*, 546:270, 2017.

[35] Yujun Deng, Yijun Yu, Yichen Song, Jingzhao Zhang, Nai Zhou Wang, Zeyuan Sun, Yangfan Yi, Yi Zheng Wu, Shiwei Wu, Junyi Zhu, Jing Wang, Xian Hui Chen, and Yuanbo Zhang. Gate-tunable room-temperature ferromagnetism in two-dimensional Fe_3GeTe_2. *Nature*, 563:94, 2018.

[36] Wanping Cai, Hualei Sun, Wei Xia, Changwei Wu, Ying Liu, Hui Liu, Yu Gong, Dao-Xin Yao, Yanfeng Guo, and Meng Wang. Pressure-induced superconductivity and structural transition in ferromagnetic $CrSiTe_3$. *Phys. Rev. B*, 102:144525, 2020.

[37] Richard M. Martin. *Electronic structure: basic theory and practical methods*. Cambridge university press, 2020.

[38] Pierre Hohenberg and Walter Kohn. Inhomogeneous electron gas. *Phys. Rev.*, 136:B864, 1964.

[39] N. David Mermin. Thermal properties of the inhomogeneous electron gas. *Phys. Rev.*, 137:A1441, 1965.

[40] Walter Kohn and Lu Jeu Sham. Self-consistent equations including exchange and correlation effects. *Phys. Rev.*, 140:A1133, 1965.

[41] John William Strutt and John William Strutt Baron Rayleigh. *The theory of sound*, volume 1. Macmillan, 1894.

[42] Walter Ritz. Über eine neue methode zur lösung gewisser variationsprobleme der mathematischen physik. *Journal für die reine und angewandte Mathematik*, 135:1, 1909.

[43] Frank Herman, John P. Van Dyke, and Irene B. Ortenburger. Improved statistical exchange approximation for inhomogeneous many-electron systems. *Phys. Rev. Lett.*, 22:807, 1969.

[44] John P. Perdew and Kieron Burke. Comparison shopping for a gradient-corrected density functional. *Int. J. Quant. Chem.*, 57:309, 1996.

[45] Axel D. Becke. Density-functional exchange-energy approximation with correct asymptotic behavior. *Phys. Rev. A*, 38:3098, 1988.

[46] John P. Perdew and Yue Wang. Accurate and simple analytic representation of the electron-gas correlation energy. *Phys. Rev. B*, 45:13244, 1992.

[47] John P. Perdew, Kieron Burke, and Matthias Ernzerhof. Generalized gradient approximation made simple. *Phys. Rev. Lett.*, 77:3865, 1996.

[48] Wolfram Koch and Max C. Holthausen. *A chemist's guide to density functional theory*. John Wiley & Sons, 2015.

[49] Klaus Koepernik and Helmut Eschrig. Full-potential nonorthogonal local-orbital minimum-basis band-structure scheme. *Phys. Rev. B*, 59:1743, 1999.

[50] L. Bellaiche and David Vanderbilt. Virtual crystal approximation revisited: Application to dielectric and piezoelectric properties of perovskites. *Phys. Rev. B*, 61:7877, 2000.

[51] Toru Moriya. *Spin fluctuations in itinerant electron magnetism*, volume 56. Springer Science & Business Media, 2012.

[52] Toru Moriya and Kazuo Ueda. Spin fluctuations and high temperature superconductivity. *Adv. Phys.*, 49:555, 2000.

[53] Tôru Moriya and Kazuo Ueda. Antiferromagnetic spin fluctuation and superconductivity. *Rep. Prog. Phys.*, 66:1299, 2003.

[54] Daniel Guterding. *Microscopic modelling of organic and iron-based superconductors*. PhD thesis, Johann Wolfgang Goethe-Universität, Frankfurt am Main, 2017.

[55] Siegfried Graser, T. A. Maier, P. J. Hirschfeld, and D. J. Scalapino. Near-degeneracy of several pairing channels in multiorbital models for the fe pnictides. *New J. Phys.*, 11:025016, 2009.

[56] Gerald D. Mahan. *Many-particle physics*. Springer Science & Business Media, 2013.

[57] Antoine Georges, Gabriel Kotliar, Werner Krauth, and Marcelo J. Rozenberg. Dynamical mean-field theory of strongly correlated fermion systems and the limit of infinite dimensions. *Rev. Mod. Phys.*, 68:13, 1996.

[58] Cédric Weber, Kristjan Haule, and Gabriel Kotliar. Strength of correlations in electron- and hole-doped cuprates. *Nat. Phys.*, 6:574, 2010.

[59] Markus Aichhorn, Leonid Pourovskii, and Antoine Georges. Importance of electronic correlations for structural and magnetic properties of the iron pnictide superconductor LaFeAsO. *Phys. Rev. B*, 84:054529, 2011.

[60] Z.P. Yin, Kristjan Haule, and Gabriel Kotliar. Kinetic frustration and the nature of the magnetic and paramagnetic states in iron pnictides and iron chalcogenides. *Nat. Mater.*, 10:932, 2011.

[61] J.H. Shim, Kristjan Haule, and Gabriel Kotliar. Modeling the localized-to-itinerant electronic transition in the heavy fermion system $CeIrIn_5$. *Science*, 318:1615, 2007.

[62] S. Yu Savrasov, G. Kotliar, and Elihu Abrahams. Correlated electrons in δ-plutonium within a dynamical mean-field picture. *Nature*, 410:793, 2001.

[63] Walter Metzner and Dieter Vollhardt. Correlated lattice fermions in d=∞ dimensions. *Phys. Rev. Lett.*, 62:324, 1989.

[64] Y. Kuramoto and T. Watanabe. Theory of momentum-dependent magnetic response in heavy-fermion systems. *Phys. B + C*, 148:80, 1987.

[65] Fusayoshi J. Ohkawa. Electron correlation in the hubbard modelin d=∞ dimension. *J. Phys. Soc. Jpn.*, 60:3218, 1991.

[66] Fusayoshi J. Ohkawa. Heavy electrons in the Mott-transition region. *Prog. Theor. Phys. Suppl.*, 106:95, 1991.

[67] Antoine Georges and Gabriel Kotliar. Hubbard model in infinite dimensions. *Phys. Rev. B*, 45:6479, 1992.

[68] M. Jarrell. Hubbard model in infinite dimensions: A quantum Monte Carlo study. *Phys. Rev. Lett.*, 69:168, 1992.

[69] Jorge E. Hirsch and R. Martin Fye. Monte Carlo method for magnetic impurities in metals. *Phys. Rev. Lett.*, 56:2521, 1986.

[70] M. J. Rozenberg, X.Y. Zhang, and G. Kotliar. Mott-Hubbard transition in infinite dimensions. *Phys. Rev. Lett.*, 69:1236, 1992.

[71] Antoine Georges and Werner Krauth. Numerical solution of the d=∞ Hubbard model: Evidence for a Mott transition. *Phys. Rev. Lett.*, 69:1240, 1992.

[72] Olivier Parcollet, Michel Ferrero, Thomas Ayral, Hartmut Hafermann, Igor Krivenko, Laura Messio, and Priyanka Seth. TRIQS: A toolbox for research on interacting quantum systems. *Comput. Phys. Commun.*, 196:398, 2015.

[73] Priyanka Seth, Igor Krivenko, Michel Ferrero, and Olivier Parcollet. TRIQS/CTHYB: A continuous-time quantum Monte Carlo hybridisation expansion solver for quantum impurity problems. *Comput. Phys. Commun.*, 200:274, 2016.

[74] Markus Aichhorn, Leonid Pourovskii, Priyanka Seth, Veronica Vildosola, Manuel Zingl, Oleg E. Peil, Xiaoyu Deng, Jernej Mravlje, Gernot J. Kraberger, Cyril Martins, Michel Ferrero, and Olivier Parcollet. TRIQS/DFTTools: A TRIQS application for ab initio calculations of correlated materials. *Comput. Phys. Commun.*, 204:200, 2016.

[75] B. Bauer, L. D. Carr, H. G. Evertz, A. Feiguin, J. Freire, S. Fuchs, L. Gamper, J. Gukelberger, E. Gull, S. Guertler, A. Hehn, R. Igarashi, S. V. Isakov, D. Koop, P.N. Ma, P. Mates, H. Matsuo, O. Parcollet, G. Pawłowski, J. D. Picon, L. Pollet, E. Santos, V. W. Scarola, U. Schollwöck, C. Silva, B. Surer, S. Todo, S. Trebst, M. Troyer, M. L. Wall, P. Werner, and S. Wessel. The ALPS project release 2.0: open source software for strongly correlated systems. *J. Stat. Mech. Theory Exp.*, 2011:P05001, 2011.

[76] Hiroshi Shinaoka, Emanuel Gull, and Philipp Werner. Continuous-time hybridization expansion quantum impurity solver for multi-orbital systems with complex hybridizations. *Comput. Phys. Commun.*, 215:128, 2017.

[77] Hiroshi Shinaoka, Yusuke Nomura, and Emanuel Gull. Efficient implementation of the continuous-time interaction-expansion quantum Monte Carlo method. *Comput. Phys. Commun.*, 252:106826, 2020.

[78] ALPSCore/CT-HYB-SEGMENT. https://github.com/ALPSCore/CT-HYB-SEGMENT. Accessed: 2022-12-13.

[79] Markus Wallerberger, Andreas Hausoel, Patrik Gunacker, Alexander Kowalski, Nicolaus Parragh, Florian Goth, Karsten Held, and Giorgio Sangiovanni. w2dynamics: Local one-and two-particle quantities from dynamical mean field theory. *Comput. Phys. Commun.*, 235:388, 2019.

[80] Vijay Singh, Uthpala Herath, Benny Wah, Xingyu Liao, Aldo H Romero, and Hyowon Park. DMFTWDFT: An open-source code combining dynamical mean field theory with various density functional theory packages. *Comput. Phys. Commun.*, 261:107778, 2021.

[81] K. Haule. DFT + embedded DMFT Functional. http://hauleweb.rutgers.edu/tutorials/index.html. Accessed: 2022-12-13.

[82] Hiroshi Shinaoka, Junya Otsuki, Mitsuaki Kawamura, Nayuta Takemori, and Kazuyoshi Yoshimi. DCore: Integrated DMFT software for correlated electrons. *SciPost Physics*, 10:117, 2021.

[83] Junya Otsuki, Kazuyoshi Yoshimi, Hiroshi Shinaoka, and Yusuke Nomura. Strong-coupling formula for momentum-dependent susceptibilities in dynamical mean-field theory. *Phys. Rev. B*, 99:165134, 2019.

[84] I. I. Mazin, M. D. Johannes, L. Boeri, K. Koepernik, and David J. Singh. Problems with reconciling density functional theory calculations with experiment in ferropnictides. *Phys. Rev. B*, 78:085104, 2008.

[85] Qi Song, Y.J. Yan, Z.R. Ye, M.Q. Ren, D.F. Xu, S.Y. Tan, X.H. Niu, B.P. Xie, T. Zhang, R. Peng, H.C. Xu, J. Jiang, and D.L. Feng. Electronic structure of the titanium-based oxypnictide superconductor $Ba_{0.95}Na_{0.05}Ti_2Sb_2O$ and direct observation of its charge density wave order. *Phys. Rev. B*, 93:024508, 2016.

[86] Wataru Ishii, Takeshi Yajima, and Zenji Hiroi. Electronic phase diagram of the titanium oxypnictide superconductor $BaTi_2(Sb_{1-x}Bi_x)_2O$. In *J. Phys. Conf. Ser.*, volume 969, page 012052. IOP Publishing, 2018.

[87] Guanghua Zhang, J. K. Glasbrenner, R. Flint, I. I. Mazin, and R. M. Fernandes. Double-stage nematic bond ordering above double stripe magnetism: Application to $BaTi_2Sb_2O$. *Phys. Rev. B*, 95:174402, 2017.

[88] G. Ouvrard, E. Sandre, and R. Brec. Synthesis and crystal structure of a new layered phase: The chromium hexatellurosilicate $Cr_2Si_2Te_6$. *J. Solid State Chem.*, 73:27, 1988.

[89] Richard E. Marsh. The crystal structure of $Cr_2Si_2Te_6$: Corrigendum. *J. Solid State Chem.*, 77:190, 1988.

[90] V. Carteaux, G. Ouvrard, J.C. Grenier, and Y. Laligant. Magnetic structure of the new layered ferromagnetic chromium hexatellurosilicate $Cr_2Si_2Te_6$. *J. Mag. Mag. Mater.*, 94:127, 1991.

[91] V. Carteaux, F. Moussa, and M. Spiesser. 2D Ising-like ferromagnetic behaviour for the lamellar $Cr_2Si_2Te_6$ compound: A neutron scattering investigation. *Europhys. Lett.*, 29:251, 1995.

[92] V. Carteaux, D. Brunet, G. Ouvrard, and G. Andre. Crystallographic, magnetic and electronic structures of a new layered ferromagnetic compound $Cr_2Ge_2Te_6$. *J. Phys.: Condens. Matter*, 7:69, 1995.

[93] Kailang Xu, Zhenhai Yu, Wei Xia, Meng Xu, Xianliang Mai, Lin Wang, Yanfeng Guo, Xiangshui Miao, and Ming Xu. Unique 2D–3D structure transformations in trichalcogenide $CrSiTe_3$ under high pressure. *J. Phys. Chem. C*, 124:15600, 2020.

[94] Dilip Bhoi, Jun Gouchi, Naoka Hiraoka, Yufeng Zhang, Norio Ogita, Takumi Hasegawa, Kentaro Kitagawa, Hidenori Takagi, Kee Hoon Kim, and Yoshiya Uwatoko. Nearly room-temperature ferromagnetism in a pressure-induced correlated metallic state of the van der Waals insulator $CrGeTe_3$. *Phys. Rev. Lett.*, 127:217203, 2021.

[95] Zhenhai Yu, Wei Xia, Kailang Xu, Ming Xu, Hongyuan Wang, Xia Wang, Na Yu, Zhiqiang Zou, Jinggeng Zhao, Lin Wang, Xiangshui Miao, and Yanfeng Guo. Pressure-induced structural phase transition and a special amorphization phase of two-dimensional ferromagnetic semiconductor $Cr_2Ge_2Te_6$. *J. Phys. Chem. C*, 123:13885, 2019.